

UNIVERSITÀ DEGLI STUDI DI GENOVA

SCUOLA POLITECNICA

DIME

Dipartimento di Ingegneria Meccanica, Energetica,  
Gestionale e dei Trasporti



MASTER OF SCIENCE THESIS  
IN  
MECHANICAL ENGINEERING

**Investigations into Alternative Cooling Air Supply  
Concepts for the Last Stage Blade of a Heavy-Duty  
Gas Turbine**

**Supervisors:**

Dr. Cyrille Jerome Bricaud - Ansaldo Energia Switzerland

Dr. Oliver Schulz - Ansaldo Energia Switzerland

Chiar.<sup>mo</sup> Prof. Ing. Alessandro Bottaro

**Candidate:**

Alberto Tanghetti

March 2022

In collaboration with:



## Acknowledgements

Vorrei ringraziare il Prof. Alessandro Bottaro per avermi dato l'opportunità di scrivere questa tesi sotto la sua supervisione.

Mein ganz besonderer Dank gilt meinem Betreuer Dr. Oliver Schulz, der mich mit zahlreichen Anregungen und Diskussionen stets unterstützt und so maßgeblich zur Entwicklung dieser Arbeit beigetragen hat. Außerdem möchte ich mich bei meinem Betreuer Dr. Cyrille Bricaud für die vielen konstruktiven Gespräche und fachlichen Impulse bedanken. Zusätzlich bedanke ich mich bei Dr. Thomas Zierer für die Hilfestellungen und die tatkräftige Unterstützung. Ein herzlicher Dank geht an Carl Berger, Stephan Strueken, Stefan Rofka und Rene Waelchli für die offene und angenehme Arbeitsatmosphäre, dank der ich mich bei Ansaldo Energia in Baden sehr wohlfühlt habe.

I would like to thank Antoine and Alberto, friends before colleagues, for their valuable help and the time spent together.

Ringrazio Francesco, con cui ho condiviso il percorso universitario.

Dedico questa tesi ai miei genitori, Paolo e Sonia e a mia sorella Sofia, che da sempre mi sostengono e mi hanno permesso di raggiungere questo traguardo.



# Ricerca su Sistemi Alternativi per Fornire Aria di Raffreddamento all'ultimo Stadio di una Turbina a Gas di tipo Heavy-Duty

## Sommario

Nelle moderne turbine a gas, la temperatura all'ingresso della turbina e, di conseguenza, la temperatura dei gas di scarico vede un rapido incremento per aumentare il rendimento e la potenza prodotta. Di conseguenza, anche gli ultimi stadi di una turbina di tipo heavy-duty richiedono un sistema di raffreddamento interno, in modo da resistere ai carichi termici e meccanici. Questa tesi presenta un lavoro di ricerca riguardo sistemi alternativi per fornire aria di raffreddamento alle pale dell'ultimo stadio di una turbina a gas di tipo heavy-duty. In particolare, un sistema di raffreddamento caratterizzato da un compressore esterno viene investigato. I vari requisiti e le condizioni al contorno del sistema alternativo vengono esaminate. Una analisi preliminare sulle performance mostra i concreti benefici apportati, in termini di rendimento. Dunque, delle soluzioni innovative vengono progettate e studiate impiegando codici fluidodinamici mono-dimensionali (1-D) e analisi fluidodinamiche numeriche (CFD). In primo luogo, i codici 1-D vengono utilizzati per ottenere le condizioni al contorno che permettono di soddisfare i requisiti in termini di aria di raffreddamento delle pale dell'ultimo stadio della turbina. Successivamente, la soluzione più promettente viene individuata e studiata mediante analisi numerica (CFD). Infine, i risultati dell'analisi CFD della soluzione più promettente vengono utilizzati per ricalibrare il codice fluidodinamico monodimensionale. Lo studio presentato in questo lavoro è svolto nel dipartimento di Secondary Air Systems di Ansaldo Energia Switzerland. Questo lavoro evidenzia i benefici apportati da un sistema di raffreddamento alternativo e ne sottolinea in oltre gli aspetti più critici, che devono essere tenuti in considerazione durante fase di implementazione. Inoltre, fissa una solida base per futuri studi riguardo sistemi di raffreddamento alternativi per l'ultimo stadio di una turbina di tipo heavy-duty.

# Investigations into Alternative Cooling Air Supply Concepts for the Last Stage Blade of a Heavy-Duty Gas Turbine

## Abstract

In modern gas turbines, the temperature at the inlet of the turbine and thus, the hot gas temperature are rising to increase the efficiency and the power output. Therefore, the last stages of heavy-duty gas turbines require cooling flows to withstand the thermal and mechanical loads. This thesis presents an investigation into alternative cooling air supply concepts for the last stage blade of a heavy-duty gas turbine. In particular, a separately integrated feed system supplied by an external compressor is studied. The requirements and boundary conditions of the alternative feed system are examined. A preliminary performance analysis shows concrete benefits in terms of efficiency. Therefore, innovative concepts are designed and studied using one-dimensional (1-D) flow networks and Computational Fluid Dynamics (CFD) simulations. First, the 1-D networks are used to obtain the boundary conditions that fulfill the cooling flow requirements of the last stage blades. Then, the most promising concept is selected and analyzed using CFD. The numerical investigations are performed at base-load and part-load conditions. Ultimately, the results of the CFD analysis of the most promising concepts are used to re-calibrate the 1-D flow networks. The studies presented in this work were carried out in the Secondary Air System team of Ansaldo Energia Switzerland. This work highlights the benefits provided by an alternative feed system as well as the critical aspects that should be considered for its implementation. Moreover, it sets a solid base for further investigations into alternative cooling air supply concepts for the last stage of a heavy-duty gas turbine.

# Nomenclature

Notation	Unit	Description
$A$	$m^2$	area
$b$	$m$	rotating disk diameter
$c, v$	$\frac{m}{s}$	absolute speed
$C_c$	—	labyrinth seal carry-over coefficient
$C_d$	—	discharge coefficient
$c_p$	$\frac{J}{kgK}$	isobaric specific heat capacity
$C_r$	—	labyrinth seal contraction coefficient
$C_t$	—	labyrinth seal throttling coefficient
$C_w = \frac{\dot{m}}{\mu b}$	—	non-dimensional superposed mass flow rate
$d, D$	$m$	diameter
$G = \frac{s}{b}$	—	axial gap ratio
$h$	$\frac{J}{kg}$	specific enthalpy
HTC	$\frac{W}{m^2K}$	heat transfer coefficient
$k$	$\frac{J}{kg}$	turbulent kinetic energy
$k$	$\frac{W}{mK}$	thermal conductivity
$l$	$m$	length of firtree channel, characteristic length
$L$	$m$	distance between the edges of two contiguous bore
$\dot{m}$	$\frac{kg}{s}$	mass flow rate
$M$	$Nm$	torque

$n$	—	vortex exponent
$N$	—	number of blades
$Nu = \frac{HTCl}{k}$	—	Nusselt number
$p$	$Pa$	pressure
$P$	$W$	power
$Pr = \frac{c_p}{\mu k}$	—	Prandtl number
$Q$	$W$	heat
$r$	$m$	radius, radial position
$R$	$\frac{J}{kgK}$	gas-specific constant
$Re_\theta = \frac{\Omega r^2}{\nu}$	—	rotational Reynolds number
$Re_s = \frac{\Omega s^2}{\nu}$	—	gap Reynolds number
$s$	$\frac{J}{kgK}$	specific entropy
$s$	$m$	distance from stationary disk
$T$	$K$	temperature
$U = (U_x, U_y, U_z)$	$\frac{m}{s}$	mean velocity vector
$w$	$\frac{m}{s}$	relative speed
$W$	$m$	fillet edge length at the inlet of the rotor bore

### Greek letters

### Unit

### Description

$\alpha$

°

swirl angle

$\beta = atan(\frac{w_\theta}{w_{ax}})$

°

angle of relative velocity at the rotor bore inlet

$\beta = \frac{w_\theta}{\Omega r}$	—	swirl ratio
$\gamma = c_p/c_v$	—	gas specific heats ratio
$\epsilon$	$\frac{m^2}{s^3}$	rate of dissipation of turbulent kinetic energy $k$
$\zeta$	—	friction coefficient
$\eta$	—	efficiency
$\lambda$	—	friction coefficient
$\lambda_T = C_w Re_\theta^{-0.8}$	—	turbulent flow parameter
$\mu$	$Pa \cdot s$	dynamic viscosity
$\nu$	$\frac{m^2}{s}$	cinematic viscosity
$\pi$	—	gas turbine pressure ratio
$\rho$	$\frac{kg}{m^3}$	density
$\tau$	$Pa$	shear stress
$\phi$	—	compressibility coefficient
$\Omega$	$\frac{rad}{s}$	rotational speed

### Superscripts and Subscripts

amb	ambient
avg	average quantity
ax	axial
C	compressor
exh	exhaust
fluid	fluid domain
GT	Gas Turbine
hot gas	hot gas

i	i-th element
in	inlet
is	isentropic
ISO	International organization for Standardization
max	maximum radius
metal	metal surface
out	outlet
p	polytropic
r	radial
rel, r	relative quantity
R	Rotor, rotoric
S	Stator, statoric
seal	sealing
t	total quantity, turbulent
T	Turbine
th	thermal
$\theta$	tangential component
0	minimum radius
$\vec{\phantom{a}}$	vector
$\dot{\phantom{a}}$	time-derivative

## Abbreviations

B4	Blade 4
CA	Cooling Air
CAD	Computer Aided Design
CC	Combined Cycle
CCX	CalculiX software
CFD	Computational Fluid Dynamics
EGH	Exhaust Gas Housing
IGES	Initial Graphics Exchange Specification
ISO	International Organization for Standardization
GT	Gas Turbine
LHV	Lower Heating Value
PSN	Pre Swirl Nozzle
RB	Rotor Bore
RHS	Rotor Heat Shield
SAS	Secondary Air System
SAF	Secondary Air Flows
SR	Stator-Rotor
TAT	Turbine Air Temperature
TCLA	Turbine Cooling and Leakage Air
TIT	Turbine Inlet Temperature
VIGV	Variable Inlet Guide Vain

# Contents

<b>Nomenclature</b>	<b>VII</b>
<b>1 Introduction</b>	<b>1</b>
1.1 Ansaldo Energia Switzerland . . . . .	1
1.2 Introduction to gas turbines . . . . .	2
1.3 Blade cooling in modern gas turbines . . . . .	4
1.4 Secondary Air Systems . . . . .	7
1.4.1 Introduction to Secondary Air System . . . . .	7
1.4.2 Last stage cooling air circuit . . . . .	12
1.5 Cooling air feed system for blades . . . . .	15
1.6 Flow in rotating cavities . . . . .	19
1.6.1 Single disk rotating in a free space . . . . .	19
1.6.2 Rotor-stator system without superposed flow . . . . .	19
1.6.3 Flow regimes in a rotor-stator cavity . . . . .	21
1.6.4 Rotor-stator system with superposed flow . . . . .	22
1.6.5 1-D flow model for the radial core rotation distribution . . . . .	23
1.7 1-D flow network . . . . .	26
1.7.1 Introduction to 1-D flow networks . . . . .	26
1.7.2 Solver . . . . .	28
<b>2 Alternative cooling air feed system design</b>	<b>29</b>
2.1 Requirements and boundary conditions . . . . .	29
2.1.1 Pressure requirements . . . . .	29
2.1.2 Mass flow requirements . . . . .	30
2.1.3 Rotor-end disk purge air . . . . .	30
2.1.4 Summary of boundary conditions and system interfaces . . . . .	30
2.2 Preliminary performance analysis . . . . .	33
2.3 Literature review and pre-selection of the basic concepts . . . . .	35
2.4 1-D flow network assembly . . . . .	41
2.4.1 External line assembly . . . . .	42
2.4.2 Internal line assembly . . . . .	43
2.4.3 Results and comparison . . . . .	49
2.5 SWOT analysis . . . . .	51
2.6 Part-load analysis . . . . .	51
<b>3 Computational Fluid Dynamics analysis</b>	<b>55</b>
3.1 Fluid domain . . . . .	55
3.1.1 Rotor bore inlet design . . . . .	57
3.2 Mesh generation . . . . .	59
3.3 Computational set-up . . . . .	60
3.3.1 Frame of reference . . . . .	60
3.3.2 Turbulence model . . . . .	60
3.3.3 Near-wall treatment . . . . .	61

3.3.4	Solver . . . . .	61
3.4	Boundary conditions . . . . .	61
3.5	Mesh sensitivity study . . . . .	64
<b>4</b>	<b>Results and discussion</b>	<b>69</b>
4.1	Degrees of freedom of the 1-D flow network . . . . .	69
4.2	Base-load case . . . . .	70
4.2.1	Stator-rotor cavity . . . . .	72
4.2.2	Rotor bore inlet . . . . .	73
4.2.3	Rotor bore friction losses . . . . .	74
4.2.4	Rotor heat shield cavity . . . . .	75
4.2.5	Re-calibration of the 1-D flow network - Pressure . . . . .	77
4.2.6	Re-calibration of the 1-D flow network - Temperature . . . . .	77
4.3	Part-load case . . . . .	79
4.3.1	Stator-rotor cavity . . . . .	79
4.3.2	Rotor bore inlet . . . . .	80
4.3.3	Rotor bore friction losses . . . . .	81
4.3.4	Rotor heat shield cavity . . . . .	81
4.3.5	Re-calibration of the 1-D flow network - Pressure . . . . .	82
4.3.6	Re-calibration of the 1-D flow network - Temperature . . . . .	83
<b>5</b>	<b>Conclusion</b>	<b>84</b>
	<b>References</b>	<b>85</b>
<b>A</b>	<b>Appendix</b>	<b>88</b>
A.1	Core swirl estimation in the stator-rotor cavity . . . . .	88
A.2	Governing equations for a rotating frame of reference . . . . .	90
A.3	Realisable $k - \epsilon$ turbulence model . . . . .	90

## List of Figures

1.1	Ansaldo Energia Gas Turbine fleet [1]. . . . .	1
1.2	Ideal Brayton-Joule cycle [2]. . . . .	2
1.3	Real Brayton-Joule open cycle, adapted from [3]. . . . .	3
1.4	Performance map of a simple cycle gas turbine [2]. . . . .	4
1.5	Examples of internal cooling flows for vanes (left) and blades (right) [4]. . . . .	5
1.6	Blade cooling scheme [5]. . . . .	6
1.7	Internal air system for a gas turbine [6]. . . . .	7
1.8	Scheme of a typical GT (a); scheme of a GT with uncooled turbine (b). . . . .	8
1.9	Thermodynamic cycle of a Gas Turbine compared to the cycle of a Gas Turbine under the assumptions of "equivalent uncooled turbine". . . . .	9
1.10	Sketch of the cooling air network of the Ansaldo Energia GT 26 Gas Turbine [7]. . . . .	10
1.11	Sketch of the CA network of the Ansaldo Energia AE94.3A [5]. . . . .	10
1.12	Scheme of the current CA line for the last two rows of blades of the turbine, adapted from [8]. . . . .	12
1.13	Cooling air flow at the rotor heat shield cavity, adapted from [9] [10]. . . . .	13
1.14	Rotor-end disk purge air overview. . . . .	13
1.15	Sketch of the alternative CA lines for the last two stages of the turbine, adapted from [8]. . . . .	14
1.16	Example of a typical CA feed system for blades (source: Rolls Royce, adapted from [11]). . . . .	15
1.17	(a) CA with no pre-swirl; (b) CA with pre-swirl, adapted from [12] . . . . .	16
1.18	Inlet discharge coefficient for rotating holes [13]. . . . .	16
1.19	Separation bubble at the inlet of the RB due to high relative tangential velocity in the pre-swirl cavity, adapted from [12]. . . . .	17
1.20	Thermodynamic transformations for a feed system with no pre-swirl (left) and with pre-swirl (right) along an ideal streamline. . . . .	18
1.21	Flow structure on a free disk according to [14]. . . . .	19
1.22	Scheme of a SR cavity [6]. . . . .	20
1.23	Radial (left) and tangential (right) velocity profiles across a rotor-stator cavity [15]. . . . .	21
1.24	Flow regimes in a SR cavity according to Daily and Nece [16]. . . . .	22
1.25	Rotating flow patterns for a rotor-stator system with a superposed flow (based on the CFD analysis described in [17]). . . . .	23
1.26	Example of a typical radial distribution of $v_\theta$ in a pre-swirl SR cavity [12]. . . . .	26
1.27	Example of a simple 1-D network (top) and the implementation in the flow network (bottom) [18]. . . . .	27
1.28	Scheme of the solver implemented in the one-dimensional flow network [18]. . . . .	28
2.1	Example of hot gas pressure distribution along the leading edge. . . . .	29

2.2	Boundary conditions and design targets of the alternative cooling air feed system, adapted from [8]. . . . .	31
2.3	Example of the external compressor map for different ambient temperatures. . . . .	32
2.4	Balancing features. . . . .	33
2.5	Leakage to the bearing case. . . . .	33
2.6	Scheme of the current GT configuration (left) compared with the proposed configuration (right). . . . .	33
2.7	Cover plate with ribs [19]. . . . .	35
2.8	Cover plate without ribs [19]. . . . .	36
2.9	Example of cover plate fixation via supporting bushes [19]. . . . .	37
2.10	Supporting bushes [19]. . . . .	37
2.11	Connection via bores in the rotor disk [19]. . . . .	38
2.12	Scheme of a labyrinth seal [20]. . . . .	39
2.13	Concept with cover plate. . . . .	40
2.14	Concept without cover plate. . . . .	40
2.15	Cooling air flow at the RHS cavity for the alternative cooling air feed system, adapted from [9] and [10]. . . . .	41
2.16	Example of the assembly of the 1-D flow network for the external line. . . . .	43
2.17	Example of the assembly of the 1-D flow network for the internal line. . . . .	43
2.18	Detail of the 1-D flow network at the SR cavity. . . . .	45
2.19	Example of discharge coefficients at the RB inlet, adapted from [12] and [13]. . . . .	46
2.20	Detail of the 1-D flow network at the RB inlet. . . . .	46
2.21	Detail of the 1-D flow network at the RB outlet. . . . .	47
2.22	Detail of the 1-D flow network at the labyrinth sealings. . . . .	48
2.23	Detail of the 1-D flow network at the labyrinth sealing in the bearings area. . . . .	49
2.24	Locations of pressure measurement points in concept 2. . . . .	49
2.25	Pressure distributions for concept 1 and concept 2 for a PSN configuration. . . . .	50
2.26	Comparison configuration with and without PSN for concept 2. . . . .	50
2.27	Ansaldo GT 26 loading operation phase. . . . .	51
2.28	Complete 1-D flow network of the cooling air feed system for the blades of the last two stages of the turbine. . . . .	52
2.29	Scheme of the simplified characteristic map assumed for the external compressor. . . . .	53
2.30	Total relative pressure distribution at base-load and part-load. . . . .	54
3.1	Sketch of the fluid domain and its position inside the GT (left); CAD model of the fluid domain (right). . . . .	56
3.2	Sketch of the fluid domain at the labyrinth seal. . . . .	56
3.3	Detail of the CAD model at the RHS cavity. . . . .	57
3.4	Streamlines at the inlet of a rotating bore with sharp edges (a) and with fillet edges (b) [21]. . . . .	57
3.5	RB inlet cross-section on the $x - \theta$ plane [22]. . . . .	58
3.6	RB inlet cross-section on the $r - \theta$ plane [22]. . . . .	58

3.7	Front view (left) and $x - \theta$ view (right) of the RB fillet inlet. . . . .	59
3.8	Non-dimensional velocity profile at the wall. . . . .	61
3.9	Boundary conditions. . . . .	63
3.10	Coarse mesh. . . . .	64
3.11	Fine mesh. . . . .	65
3.12	Residuals. . . . .	65
3.13	RB average relative speed (top) and average relative pressure (bottom). . . . .	66
3.14	Contour of $y^+$ over the rotoric walls. . . . .	66
3.15	Profiles of the relative velocity in the RB for the five different grids. . . . .	67
3.16	Profiles of the absolute velocity in the RB for the five different grids. . . . .	67
3.17	Profiles of the tangential velocity in the SR cavity for the five different grids. . . . .	68
4.1	Main control surfaces considered for the post-processing of the CFD data. . . . .	70
4.2	Comparison of total relative and static pressure for the 1-D prediction and the CFD analysis at base-load. . . . .	71
4.3	Comparison of total relative temperature for the 1-D prediction and the CFD analysis at base-load. . . . .	71
4.4	Tangential velocity in the SR cavity. . . . .	72
4.5	Vector flow field and pressure distribution at the inlet of the RB. . . . .	73
4.6	Discharge coefficient for a rotating bore [23]. . . . .	74
4.7	Discharge coefficient for a non-rotating orifice [13]. . . . .	75
4.8	Vector field of relative velocity at the RHS cavity and blade's firtree. . . . .	75
4.9	Discharge coefficient for a rotating orifice [13]. . . . .	76
4.10	Comparison of total relative and static pressure for the 1-D prediction, CFD analysis and the re-calibrated 1-D flow network at base-load. . . . .	77
4.11	Comparison of total relative temperature for the 1-D prediction, CFD analysis and the re-calibrated 1-D flow network at base-load. . . . .	78
4.12	Comparison of total relative and static pressure for the 1-D prediction and the CFD analysis at part-load. . . . .	79
4.13	Tangential velocity in the SR cavity at part-load. . . . .	80
4.14	Discharge coefficient for a rotating bore [23]. . . . .	80
4.15	Vector flow field for base-load (a) and for part-load (b) in the RHS cavity. . . . .	81
4.16	Discharge coefficient for a rotating orifice [13]. . . . .	82
4.17	Comparison of total relative and static pressure for the 1-D prediction, CFD analysis and the re-calibrated 1-D flow network at part-load. . . . .	82
4.18	Comparison of total relative temperature for the 1-D prediction, CFD analysis and the re-calibrated 1-D flow network at part-load. . . . .	83
A.1	Sketch of the control volume used for the core swirl estimation. . . . .	88

# List of Tables

2.1	Performance analysis. . . . .	34
2.2	Part-load analysis. . . . .	53
3.1	Number of cells for each grid. . . . .	64

# 1 Introduction

## 1.1 Ansaldo Energia Switzerland

This master thesis has been carried out in collaboration with Ansaldo Energia Switzerland in Baden, Switzerland. Ansaldo Energia Switzerland is a joint venture of Ansaldo Energia, born in 2016 after the acquisition of Alstom's advanced heavy-duty gas turbines business. The Ansaldo Energia group is a leading international player in the power generation industry, to which it brings an integrated model embracing turnkey power plants construction, power equipment (gas and steam turbines, generators and microturbines), manufacturing and services and nuclear activities. [1] Ansaldo Energia offers a complete range of heavy-duty gas turbines (GT) for power generation applications, from E to H class technology, ranging from 80 MW to 538 MW (ISO power) in a single unit configuration. This allows costumers to operate open-cycle as well as combined-cycle power plants with state of the art gas turbines in terms of efficiency, power output, emissions, fuel flexibility and cost-effectiveness (Fig. 1.1).

### Standard Configurations

Gas Turbine	Gas Turbine Performance	Power Plant Configuration	Power Plant Performance
<b>GT36-S6</b> 	369 MW 42.3%	1+1	520 MW 62.3%
		2+1	1,046 MW 62.6%
<b>GT36-S5</b> 	538 MW 42.8%	1+1	760 MW 62.6%
		2+1	1,525 MW 62.8%
<b>GT26</b> 	370 MW 41.0%	1+1	540 MW 61%
		2+1	1,083 MW 61.2%
<b>AE94.3A</b> 	340 MW 40.3%	1+1	495 MW 60%
		2+1	992 MW 60.3%
<b>AE94.2</b> 	190 MW 36.3%	1+1	287 MW 55.8%
		2+1	578 MW 56.2%
<b>AE64.3A</b> 	80 MW 36.4%	1+1	120 MW 55.7%
		2+1	243 MW 56.4%

Fig. 1.1: Ansaldo Energia Gas Turbine fleet [1].

This work was undertaken at the Secondary Air System team, which belongs to the R&D sector. The Secondary Air System department is responsible for the so-called Secondary Air Flows, which are necessary for the correct and efficient operation of the machine. Among the various tasks which the Secondary Air System department is responsible for, the development of upgrades for the current cooling air feed system is of fundamental importance.

## 1.2 Introduction to gas turbines

A GT is an internal combustion engine that uses air as the working fluid. It mainly consists of a compressor, a combustion chamber and a turbine. The working principle is based on the ideal Brayton-Joule cycle, which involves four thermodynamic processes [19], as seen in Fig. 1.2:

- Isentropic compression 1-2;
- Isobaric heat input ( $Q_{in}$ ) 2-3;
- Isentropic expansion 3-4;
- Isobaric heat dissipation ( $Q_{out}$ ) 4-1;

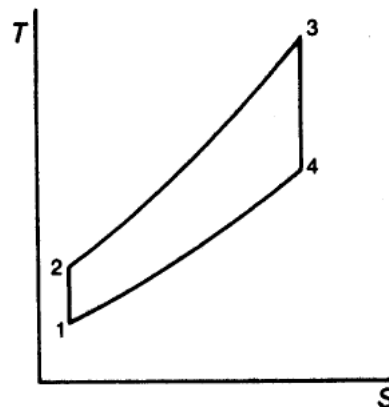


*Fig. 1.2: Ideal Brayton-Joule cycle [2].*

In a GT, the air is taken from the atmosphere, compressed in a centrifugal or axial-flow compressor and then fed into a combustion chamber. Here, fuel is added to the compressed air and burned to increase the temperature. The hot exhaust gases expand through the turbine to a static pressure below the ambient pressure and exhaust over the diffuser to the environment. In the turbine, the thermal energy is converted into mechanical energy that drives the rotor. Since the exhausts are released into the ambient, the process is referred to as an open cycle. In contrast to the ideal process, the real cycle is not characterised by two isobaric and two isentropic processes, but accounts for real effects such as pressure losses, heat exchange losses, mass losses (leakages), incomplete chemical reactions and mechanical losses. Therefore, the ideal Brayton-Joule cycle is a theoretical model. However, for real machines, the entropy variation and the efficiency of the components must be considered, as shown in Fig.1.3. [2]

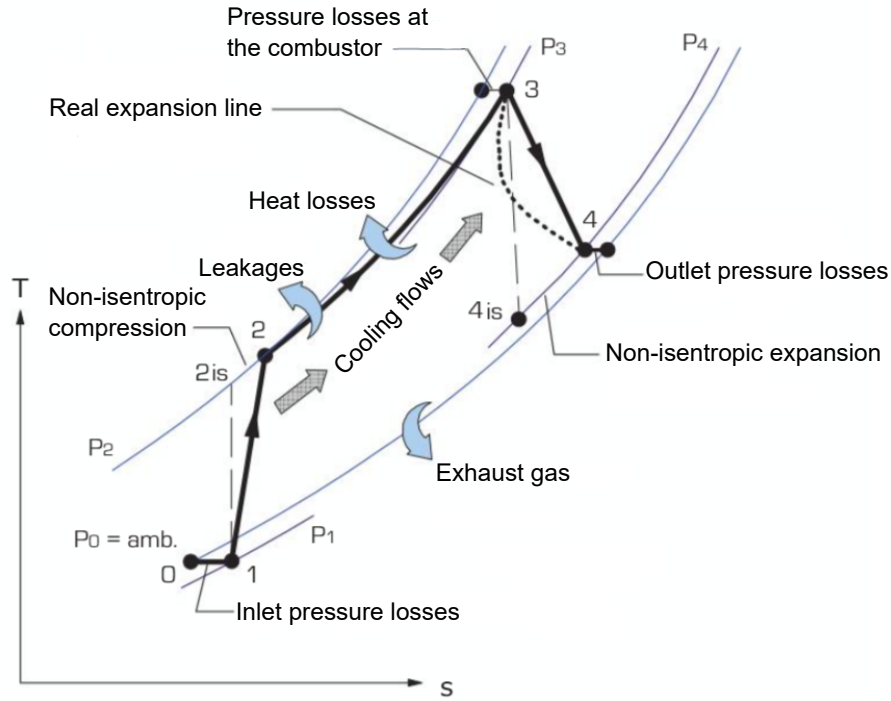


Fig. 1.3: Real Brayton-Joule open cycle, adapted from [3].

Typically, the compressor and the turbine are keyed on the same shaft with the compressor directly driven by the turbine. The energy contained in the working fluid, which is not used by the compressor, can be extracted in the form of shaft power, compressed air or thrust, depending on their application. [19]

For electric power generation, the GT is used to drive an electric generator that converts the mechanical energy available at the shaft into electricity.

GTs used for electric power generation can be divided into two main categories:

1. heavy-duty gas turbines: large power generation units, specifically developed for electric power generation. Their power range varies from 3 to 480 MW.
2. aero-derivative gas turbines: power generation units of smaller size, which have origin in the aircraft industry as aircraft engines. They have been adapted to the electrical generation by replacing the diffuser nozzle with a power turbine at their exhaust. Typically, these units range in power from 2.5 to about 50 MW.

In this thesis, a Heavy-duty single shaft GT will be examined, which is characterised by a four-stage turbine.

An important parameter of the thermodynamic cycle is the thermal efficiency.

For a real GT, the overall cycle efficiency can be written as follows:

$$\eta_{GT} = \left( \frac{\eta_T T_{hot\ gas} - \frac{T_1 \beta^{\frac{\gamma-1}{\gamma}}}{\eta_C}}{T_{hot\ gas} - T_1 - T_1 \left( \frac{\pi^{\frac{\gamma-1}{\gamma}}}{\eta_C} - 1 \right)} \right) \left( 1 - \frac{1}{\pi^{\frac{\gamma-1}{\gamma}}} \right), \quad (1.1)$$

where  $\eta_C$ ,  $\eta_T$  are respectively the efficiency of the compressor and the turbine,  $\pi$  is the overall pressure ratio and  $\gamma$  is the specific heat ratio.

Eq. 1.1 shows that the overall efficiency grows as  $T_{hot\ gas}$  increases.  $T_{hot\ gas}$  is defined in this case as the temperature of the hot gas at the inlet of the turbine. A higher efficiency leads to lower fuel consumption and lower pollutant emission. Thus, the turbine inlet temperature (TIT) must be the highest possible value, which is given by the structural mechanical limit. State-of-the-art turbine materials and cooling techniques allow hot gas temperatures of approximately 1400-1500 °C. [2]

Fig. 1.4 shows the performance map of a GT operating in a simple cycle. The efficiency is plotted as a function of the pressure ratio for different hot gas temperatures [2].

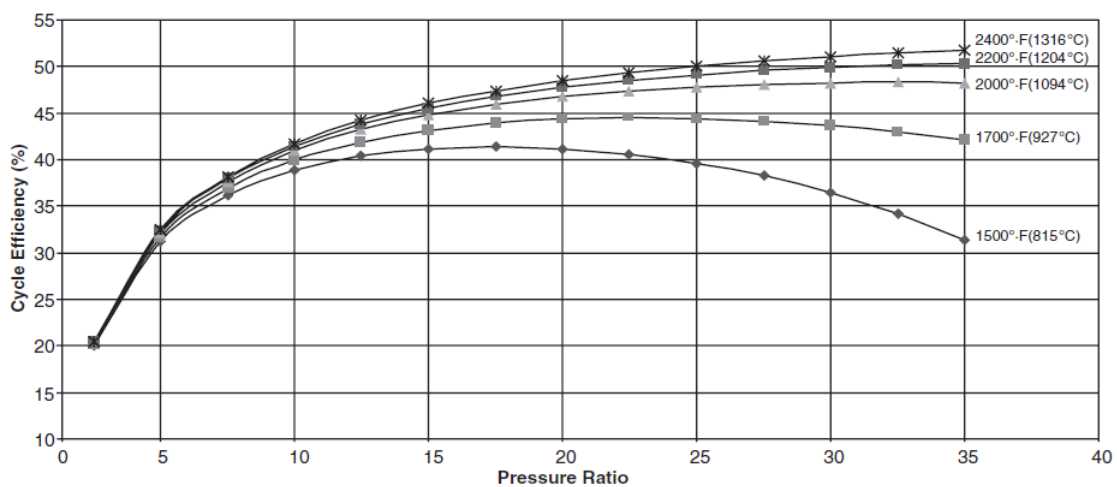


Fig. 1.4: Performance map of a simple cycle gas turbine [2].

In order to increase the efficiency, a combined cycle power plant can be used as a substitute for a simple cycle. In a combined cycle power plant, the high temperature exhausts released by the GT are used to produce high-pressure steam in a heat-recovery steam generator instead of being simply discharged into the atmosphere. The high-pressure steam powers one or more steam turbines, which increase the power output of the whole plant and its global efficiency. In contrast to the single cycle, a combined state-of-the-art cycle power plant can reach an efficiency of approximately 0.6. [3]

### 1.3 Blade cooling in modern gas turbines

GT engines focus on increasing the hot gas temperature in order to reduce the specific fuel consumption and to enhance the overall performance of the engine. However, the melting point of the materials limits the allowable temperature level of the cycle. Additionally, operation at very high temperatures reduces the lifetime of turbine vanes and blades. Consequently, a turbine blade cooling and specific coating are necessary to reduce the temperature of the blade metal to acceptable levels for the materials. [4]

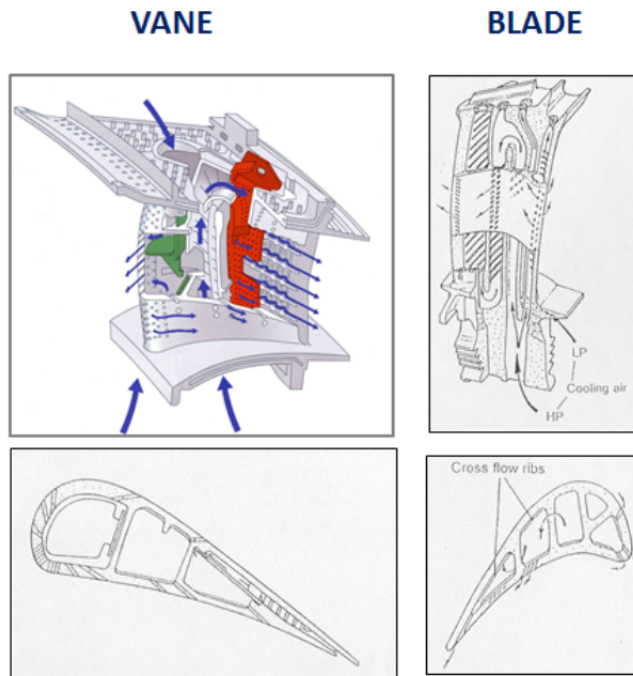


Fig. 1.5: Examples of internal cooling flows for vanes (left) and blades (right) [4].

In order to decrease the blade metal temperature, the turbine blades in the first stages are coated with a ceramic Thermal Barrier Coating (TBC). The TBC has a low heat conductivity and thus lowers the heat flow into the blades, which allows a considerable temperature difference between the blade metal surfaces and the surface of the coating layer. In addition to the TBC, an active blade cooling with Cooling Air (CA) is required to guarantee a sufficient blade lifetime with higher gas temperatures. Turbine blade cooling can be classified into three main configurations [5]:

1. Internal forced convection: a mechanism of heat transfer based on a fluid in motion inside the blade itself, in which the fluid motion is generated by an external source. In order to increase the cooling effect, special features are integrated into the cooling cavities such as ribs and pins, which increase the turbulences of the cooling air and the wetted surface, improving the heat transfer.
2. Jet impingement: an internal cooling technique with the coolant impinging on the inner surface of the blade, which enhances convective heat transfer.
3. Film cooling: an external cooling technique that aims to protect the blade's surface from the high-temperature gas with a film of cold air. The CA leaves the cavities inside the blades through several small holes and spreads over the entire blade surface, creating a cold protective film. In this way, the high-temperature gas is separated from the blade surface. In order to prevent the gas from entering the turbine blades, the static CA pressure needs to be higher than the pressure of the gas itself. This applies especially to the stagnation point at the leading edge of the blade where the static pressure is almost equal to the total pressure of the high-temperature gas.

Convective cooling techniques, namely internal forced convection and jet impingement, are insufficient for turbine inlet temperatures at the current state of art. Therefore, they are often combined with film cooling. Additionally, film cooling has the advantage to reduce the outer metal temperature of blades and vanes. This leads to lower gradients of temperature over the wall and thus, reduces the stresses. The precise choice of method depends on various factors such as gas temperature, material stress limits and costs. [5]

Fig.1.6 illustrates the three cooling methods in an exemplary blade. The trailing edge part is cooled by internal convection enhanced by turbulence promoters. The leading edge is cooled by a combination of film cooling and jet impingement. The cooling mass flow is generally bled from the compressor. Since pressure losses are not negligible and since the cooling air flows in a high pressure ambient, a relatively high pressure value must be guaranteed at the blade cooling channel inlet. Thus, the driving pressure ratio that is required for the cooling flow rate is ensured. Therefore, the feeding pressure combined with the temperature of the cooling air and its flow rate are the main constraints that must be taken into account during the design phase of a feed system for blade cooling. [5]

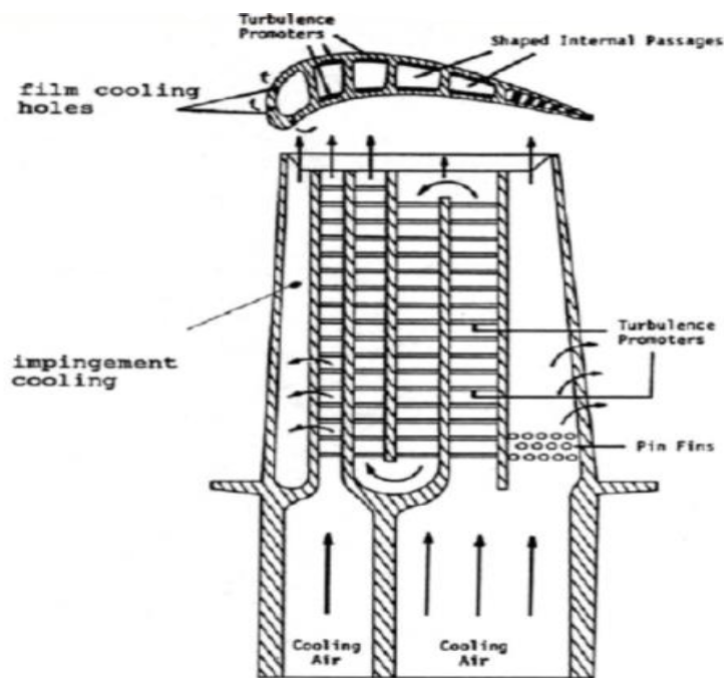


Fig. 1.6: Blade cooling scheme [5].

Due to the large size of the hot gas flow path and thus, high aspect-ratio, the last stages of the turbine are subject to high mechanical stress. Consequently, even for the last stages, which are normally not cooled, internal forced convection cooling is often required.

## 1.4 Secondary Air Systems

Secondary Air Flows (SAF) are of fundamental importance for the correct and safe operation of the GT. Secondary Air Flows can be seen as the "blood circuit" of the GT since they supply the components of the entire hardware with CA. In this section, the Secondary Air Systems (SAS) of a gas turbine will be described. Moreover, a brief summary of the circuit that provides the CA for the last two stages of the gas turbine will be presented.

### 1.4.1 Introduction to Secondary Air System

The SAS of a GT is defined as the total air flow, which does not directly pass over the aerofoil surfaces and through the combustor [24]. A scheme of an engine highlighting the complex nature of GT cooling systems is shown in Fig. 1.7. The red arrows represent the intricate system of cooling flows in a multi-stage axial turbine.

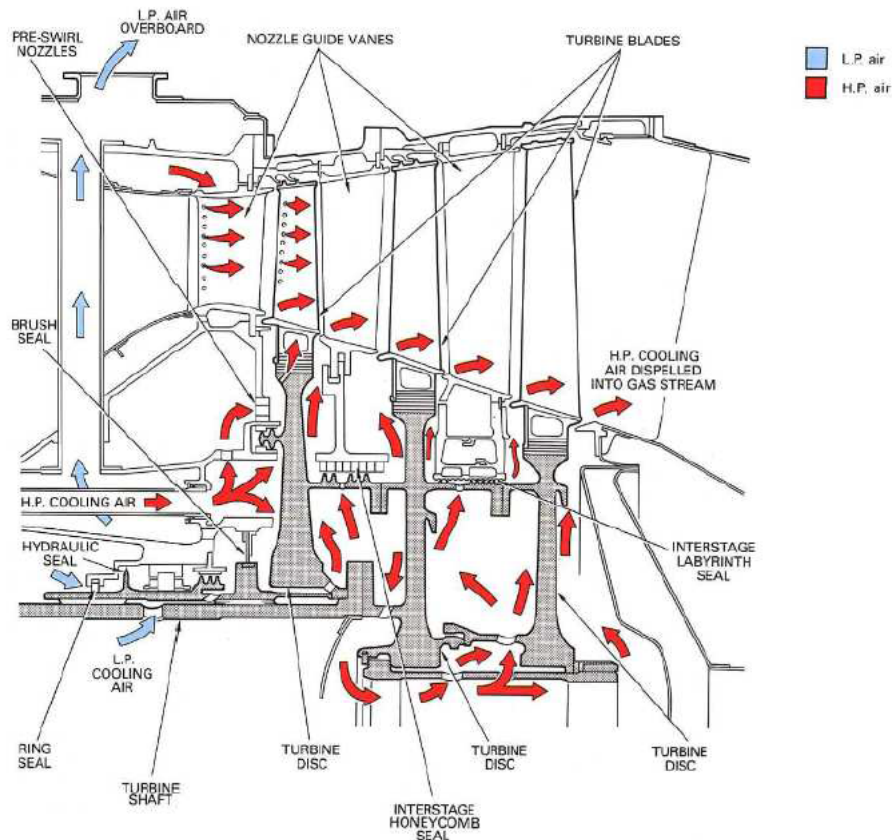


Fig. 1.7: Internal air system for a gas turbine [6].

All components in the turbine and in the combustion chamber zones must be kept at a temperature below the permitted temperature limit given by the material to prevent any damage to the machine and to increase the lifetime of the components. Therefore, the SAF is used to perform several important functions for the safe and efficient operation of the machine such as cooling of the static and rotating components, sealing, clearance control and axial thrust control. Additionally, the cooling

air must fill and pressurise rotating cavities between stator and rotor to prevent high-temperature gas ingestion.

The air mass flow rate, which is required to guarantee the SAS functions, is bled from the compressor flow path. This mass flow accounts for approximately 20% of the exhaust mass flow. Therefore, it has a strong influence on the GT performance. In order to analyse the influence of the SAF on the GT performance, it is necessary to introduce the concepts of Turbine Cooling and Leakage Air ( $TCLA$ ) and Turbine Inlet Temperature ISO ( $TIT_{iso}$ ).

$TCLA$  is defined as total of the cooling and leakage flows, as shown in:

$$TCLA = \sum \dot{m}_{turbine\ cooling\ and\ leakage\ air} \quad (1.2)$$

$TIT_{iso}$  is defined by the norm ISO 2314:2009(E) [25]. It represents the TIT of an uncooled turbine, where the cooling and leakage flows are mixed with the hot gases from the combustor before entering the first stator.

Fig. 1.8 shows a scheme of a typical GT (on the left) compared to a GT, where the turbine is uncooled and the cooling flows are mixed with hot gas from the combustor (on the right).

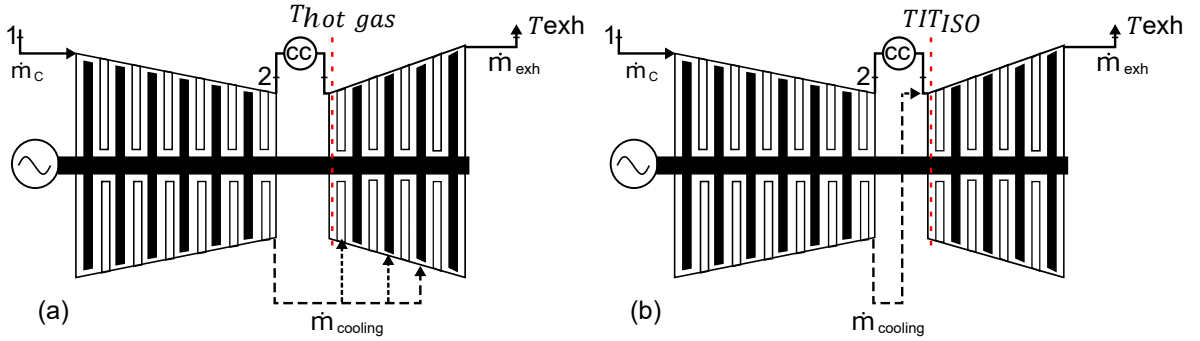


Fig. 1.8: Scheme of a typical GT (a); scheme of a GT with uncooled turbine (b).

Consequently, a real turbine, which is characterised by a lower inlet mass flow  $\dot{m}_{T,in}$  than exit mass flow  $\dot{m}_{exh}$  due to the presence of SAF (see Fig. 1.8 (a)), can be modelled by an equivalent uncooled turbine under the assumptions of:

- lower TIT ( $TIT = TIT_{ISO} < T_{hot\ gas}$ );
- same power output, same temperature of the exhaust  $T_{exh}$  and same inlet pressure;
- constant mass flow  $\dot{m}_T = \dot{m}_{exh} = const.$  over the turbine.

In Fig. 1.9, the thermodynamic cycle associated with the real GT and the thermodynamic cycle relative to the GT with the equivalent uncooled turbine are compared in the T-S diagram.

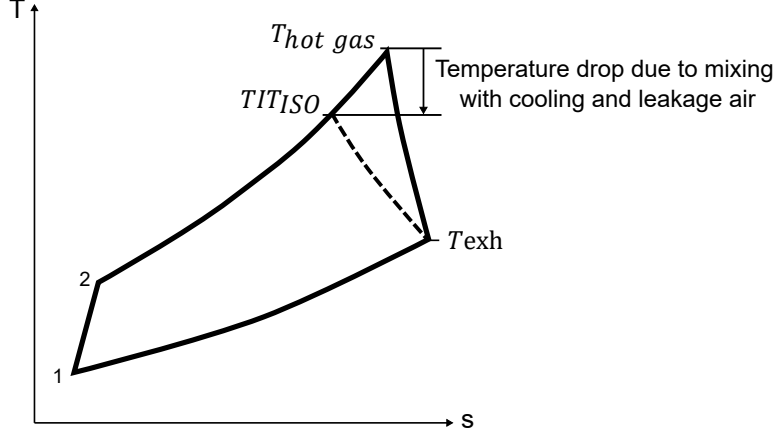


Fig. 1.9: Thermodynamic cycle of a Gas Turbine compared to the cycle of a Gas Turbine under the assumptions of "equivalent uncooled turbine".

The thermal efficiency for a GT can be computed as:

$$\eta_{th} = \frac{P_T - P_C}{\dot{Q}_{in}} = \frac{\dot{m}_T[h(T_{hot\ gas}) - h(T_{exh})] - \dot{m}_C[h(T_2) - h(T_1)]}{\dot{m}_{fuel}LHV}, \quad (1.3)$$

where  $\dot{m}_{fuel}$  is the fuel mass flow,  $LHV$  is the Lower Heating Value of the fuel,  $\dot{m}_T$  and  $\dot{m}_C$  are respectively the mass flows elaborated by the turbine and the compressor and  $h$  is the specific enthalpy evaluated for different temperatures at different locations in the machine according to Fig. 1.9. [2]

Introducing the equivalent uncooled turbine model and assuming for simplicity that all the CA is spilled out at the outlet of the compressor and neglecting ( $\dot{m}_C = \dot{m}_T = const. = \dot{m}_{exh}$ ), eq. 1.3 can be written as

$$\eta_{th} = \frac{\dot{m}_{exh}[h(TIT_{ISO}) - h(T_{exh})] - \dot{m}_{exh}[h(T_2) - h(T_1)]}{\dot{m}_{fuel}LHV}. \quad (1.4)$$

In the equivalent uncooled turbine model,  $TIT_{iso}$  is linked with the  $TCLA$  by the eq.:

$$\dot{m}_{exh} h(TIT_{iso}) = (\dot{m}_{exh} - TCLA) h(T_{hot\ gas}) + TCLA h(T_{cooling\ air}), \quad (1.5)$$

which can be derived from the energy balance at the combustion chamber, as shown in [25].

Combining eq. 1.4 with eq. 1.5, it can be noticed that the efficiency of the GT mainly depends on  $TIT_{ISO}$  and thus, on  $TCLA$ .

In particular, for a given  $T_{hot\ gas}$  and a given  $T_{exh}$ ,  $TCLA$  must be kept as low as possible in order to provide higher  $TIT_{iso}$  and thus, higher thermal efficiency of the GT cycle.

An example of a SAS lines design of a typical heavy-duty GT is pictured in Fig. 1.10 [7]. Several points of extractions along the compressor can be observed. The number of extractions results as a trade-off between complexity, costs and losses. A high number of extractions would result in a better match of turbine cooling pressures and purge pressures, reducing the pressure losses and the amount of  $TCLA$ . On the contrary, a low number of extractions would reduce costs and complexity and

provide simpler start-up and shut-down operations. The supply lines of the SAF can be located entirely outside the thermal block (as in Fig. 1.10) or even inside the thermal block (as in Fig. 1.11). The choice mainly depends on the architecture of the rotor. For instance, the Ansaldo GT 26 (Fig. 1.10) is characterised by a rotor made by a series of disks welded together. On the one hand, a welded rotor provides high stiffness and high torque transfer capability, and it reduces the costs and the required maintenance. On the other hand, a welded rotor limits the opportunity to have inner diameter compressor extractions and thus, it reduces the total amount of extraction points.

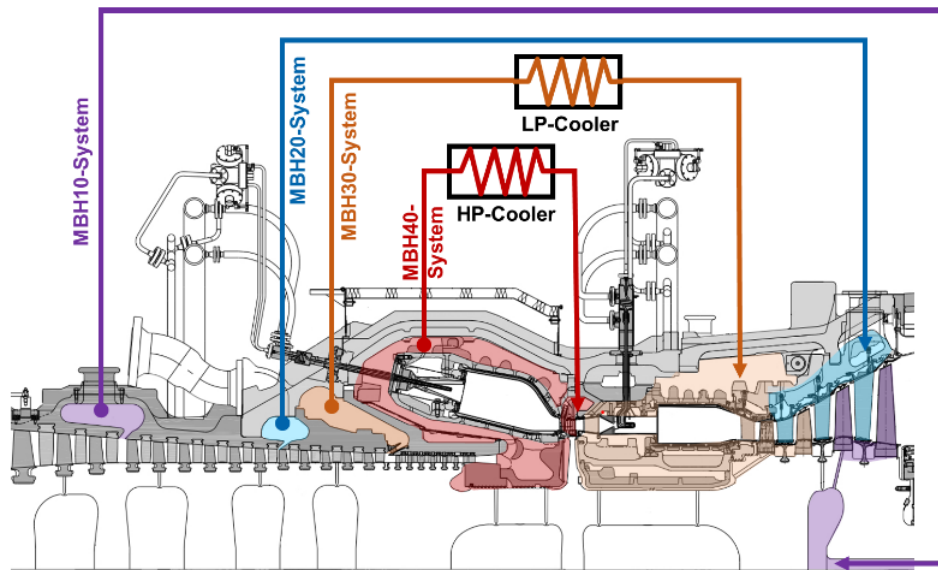


Fig. 1.10: Sketch of the cooling air network of the Ansaldo Energia GT 26 Gas Turbine [7].

On the contrary, the Ansaldo AE 94.3A, which is represented in Fig. 1.11, is characterised by a tie-rod design rotor, which allows for the presence of extraction inside the thermal block. Therefore, the number of extractions increases. However, a tie-rod rotor design has several disadvantages such as higher costs and complexity due to the presence of several individual parts. The final design is a choice of the engine manufacturer based on the aforementioned considerations.

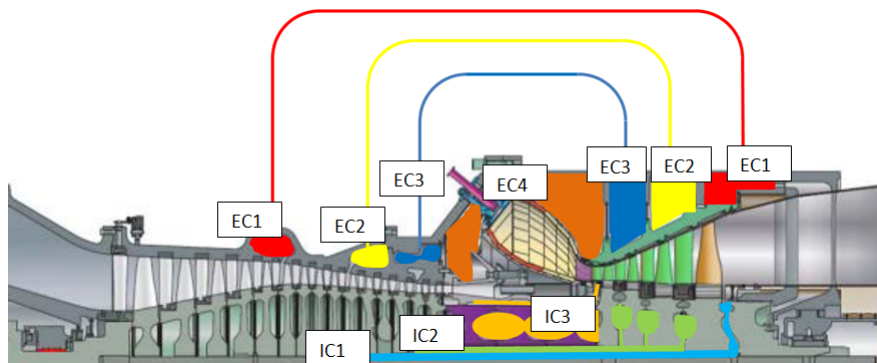


Fig. 1.11: Sketch of the CA network of the Ansaldo Energia AE94.3A [5].

In the following, a brief summary of the SAS main tasks is given [5].

- Cooling of the static and rotating components:
  - Blade cooling: the first stage blades are cooled by a portion of air bled off from the main flow at the end of the compressor to guarantee the maximum possible pressure ratio to the blades. Furthermore, in modern gas turbines, one or more additional flows can be fitted inside the rotor to supply the cooling air to other rotating stages. The cooling air is driven by centrifugal and pressure forces towards the cavities between the turbine rotor disks to reach the rotor cascades through radial bores.
  - Vane cooling: the cooling air for the first stage vanes is directly extracted at the diffuser exit, where the pressure is at its maximum level. The successive vanes are fed via external piping systems with cooling air extracted from intermediate stages along the compressor.
  - Disk cooling: the rotor disks of the turbine require cooling to prevent thermal fatigue as well as uncontrolled expansion and contraction rates for steady-state and transient operation modes.
  - Combustion chamber cooling: in the combustion chamber, the cooling mass flow is essential to preserve the components, to increase their lifetime and to operate under safety conditions.
- Sealing: the term sealing includes all devices, mechanical or fluid dynamic, used to divide zones with different pressures in order to minimise mass leakages and to protect the rotoric cavities from hot gas ingestion. Examples of such devices are abradable seals or labyrinth seals. Labyrinth seals are mechanical seals that provide a tortuous path to prevent leakage.
- Axial thrust control: the shaft experiences varying gas loads, which push in a forward direction on the compressor and a rearward direction on the turbine. The axial forces generate a net axial force, called rotor axial thrust, that needs to be countered. To balance this force and to reduce the thrust acting on the axial bearings, part of the turbine is designed as a balancing piston. This is essentially a surface subject to a pressure gradient, which is oriented against the rotor axial thrust.
- Ventilation of bearing compartments: bearing compartments are purged with cooling air in order to prevent damage to the instrumentation equipment as well as the overheating of leakage oil or oil fog.
- Blow-off air for start-up and shut-down: the SAS must provide the blow-off mass flow to avoid dangerous flow instabilities during start-up and shut-down operations.

### 1.4.2 Last stage cooling air circuit

In this section, a brief summary of the current cooling flow network for the rear stages of the heavy-duty GT, which is the subject of the study, is presented in order to facilitate a deeper comprehension of this thesis' main goal. A scheme of the CA line for the last two stages of the GT is shown in Fig. 1.12.

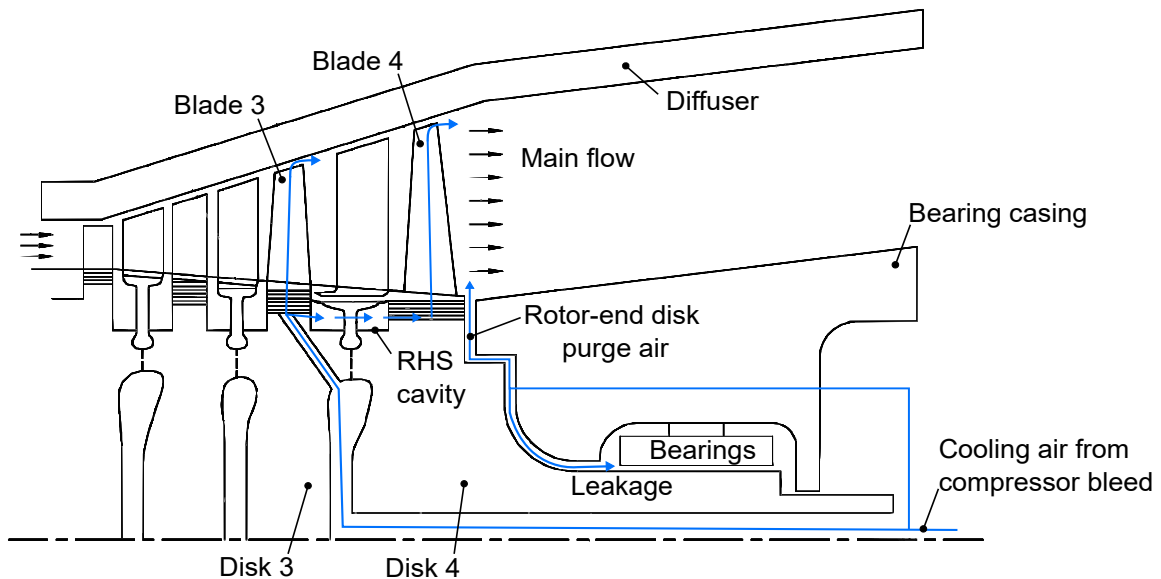
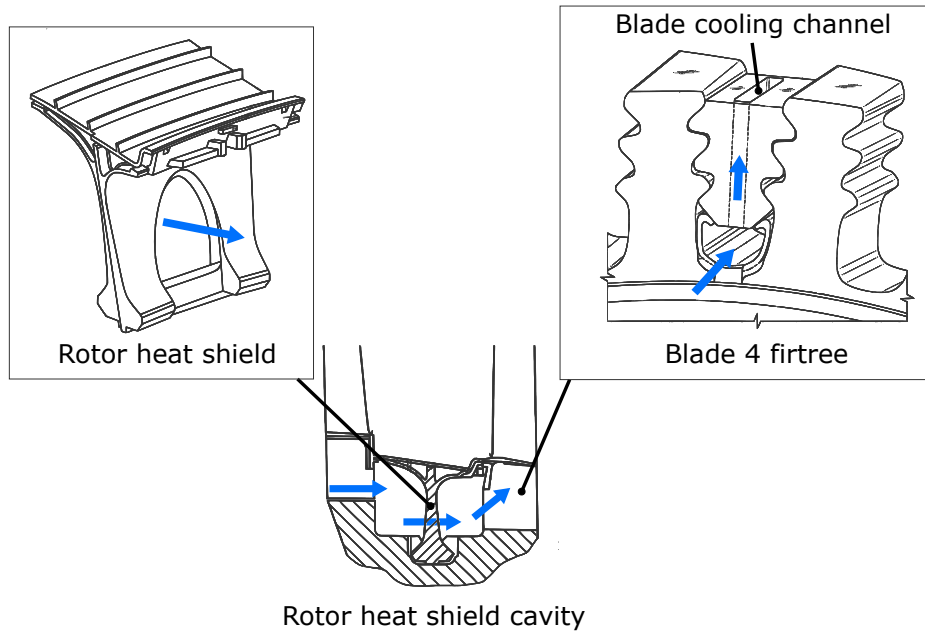


Fig. 1.12: Scheme of the current CA line for the last two rows of blades of the turbine, adapted from [8].

The CA for blade three and blade four is bled from the compressor after the first stages. The air flows through an external piping line and is guided through a hole bored in the shaft into a cavity between disks three and four. The CA flows from the cavity through radial bores up to the firtree of blade three. A fraction of this air is guided directly into the cooling channels of blade three and then discharges into the hot gas channel through exit holes at the tip of the blade.

The remaining air flows from the firtree of blade three to the Rotor Heat Shields (RHS) cavity between the penultimate and the last stages. From the RHS cavity, the air goes to the firtree of blade four and then it feeds the blades. Ultimately, the air is discharged from the tip of the blades into the hot gas stream at the inlet of the diffuser.

In Fig. 1.13, the CA flow path from blade three to the firtree of blade four is shown in more detail.



*Fig. 1.13: Cooling air flow at the rotor heat shield cavity, adapted from [9] [10].*

A small portion of the CA, named rotor-end disk purge air, is directed to the turbine rotor outlet face before entering the main rotor bore (RB) in the shaft. It discharges between the rotor-end surface and the exhaust gas diffuser into the hot gas (see Fig. 1.14). Thereby, the ingestion of hot gas into the system is prevented [24].

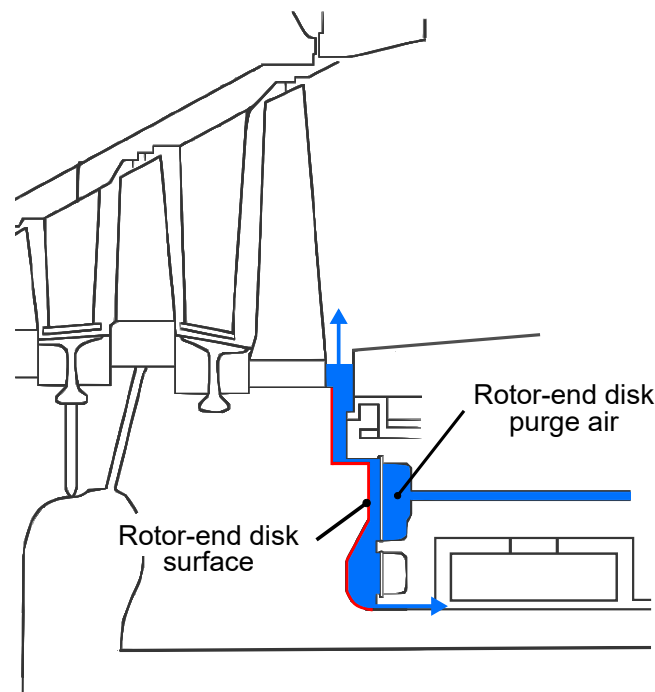


*Fig. 1.14: Rotor-end disk purge air overview.*

The pressure of the cooling air spilled from the compressor and used to provide CA to the last two stages is significantly higher than the requirement of blade four. This is due to the fact that the pressure of the cooling line is driven by the required pressure of blade three, which is notably higher than the actual target of blade four. Therefore, the energy spent to pressurise the cooling air above the required pressure of blade four counts as a loss.

An alternative turbine last stage cooling supplying system, which delivers the cooling air from an external compressor, would improve the engine's performance by delivering cooling air at lower pressure.

Furthermore, the air pressure of the current cooling system strongly depends on the GT operation mode, since the Variable Guide Vanes (VGVs) of the compressor are partly closed to reduce the engine's power during part-load operation modes. Therefore, the pressure supplied by the compressor and with it the pressure of the mentioned cooling system air significantly decreases.

An external compressor would uncouple the supplied pressure from the operation mode, ensuring proper cooling during all the GT operation modes.

Additionally, an external source would supply air at a lower temperature compared to the current cooling system. Colder cooling air would decrease the required blade cooling mass flow. A lower mass flow of CA for blade four would have a direct positive impact on the engine's performance since it would reduce the  $TCLA$ . In Fig. 1.15, a sketch of the SAS line for the alternative feed system is shown.

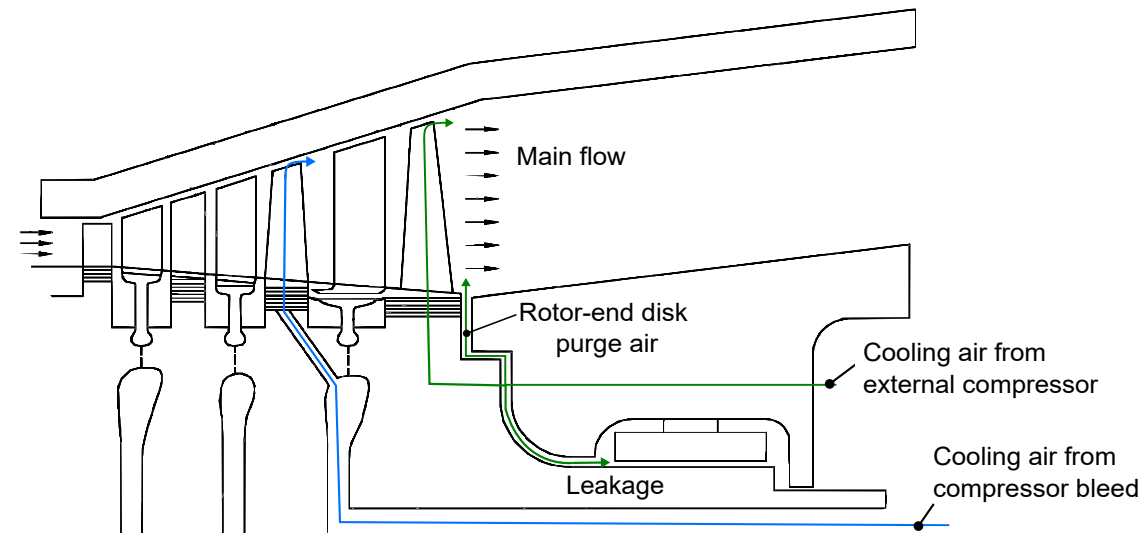
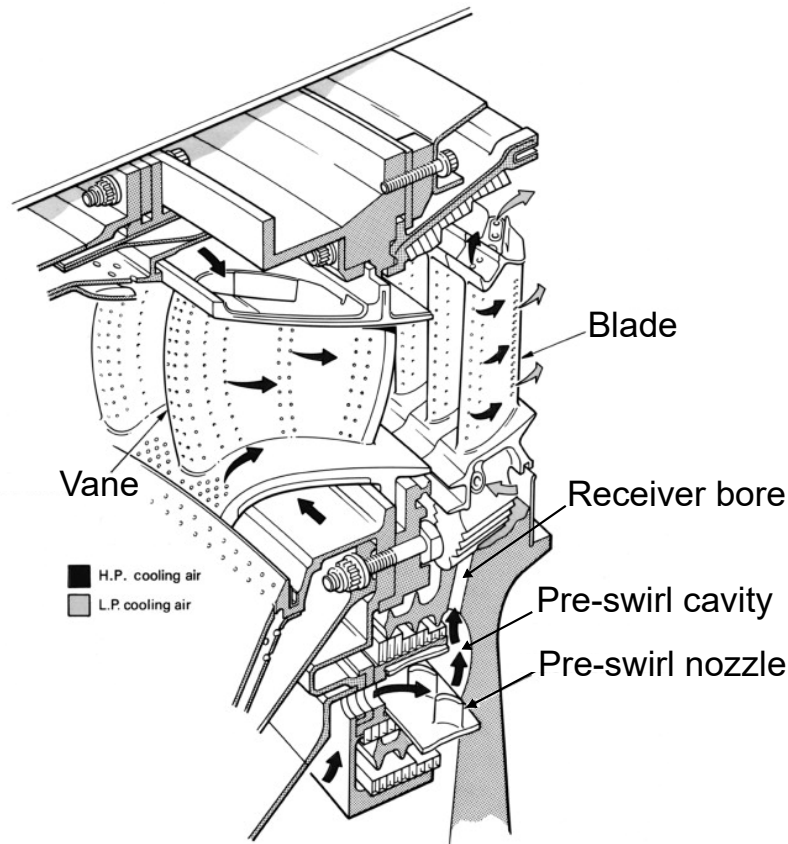


Fig. 1.15: Sketch of the alternative CA lines for the last two stages of the turbine, adapted from [8].

The main goal of this work is therefore the design of an alternative feed system for the last stage of a heavy-duty GT, focusing on the feasibility and the performance assessment.

## 1.5 Cooling air feed system for blades

As mentioned in section 1.3, the TIT is one of the most relevant parameters regarding gas turbines since an increase of the TIT can significantly raise the GT efficiency. During the last years, efforts have been made to improve materials and coating in order to increase the maximum allowable temperature. However, the need for a cooling system for the turbine is inevitable.



*Fig. 1.16: Example of a typical CA feed system for blades (source: Rolls Royce, adapted from [11]).*

In Fig. 1.16 a scheme of a typical CA feed system is shown: the compressor air is fed into the annular chamber (pre-swirl cavity), which consists of stator and rotor surfaces. Usually, with the help of a swirl generator (axial pre-swirl nozzle), the cooling air enters into the cavity at a certain angle with respect to the direction of rotation of the rotor. This means that the receiver channels in the rotor are supplied with a flow having a more favourable angle of attack  $\beta = \text{atan}\left(\frac{w_{\theta}}{w_{ax}}\right)$  (see Fig. 1.17 (b)) [12].

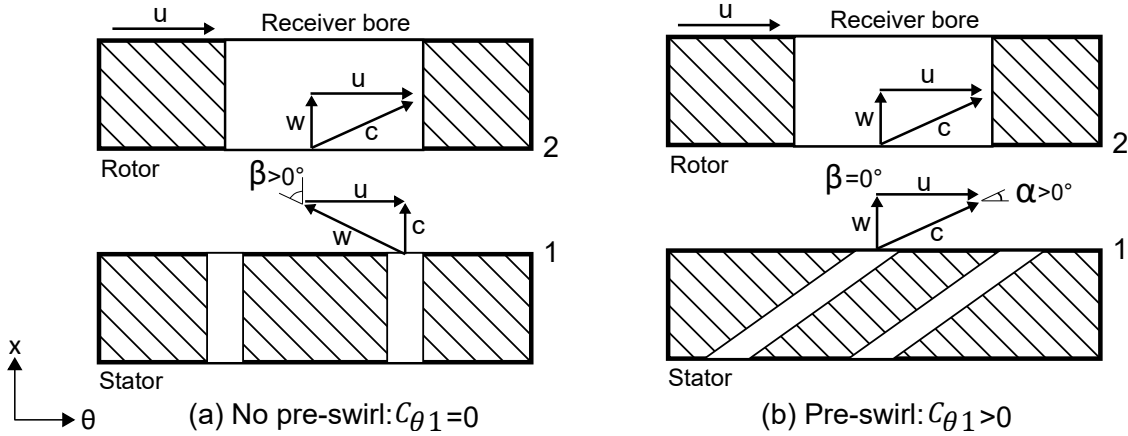


Fig. 1.17: (a) CA with no pre-swirl; (b) CA with pre-swirl, adapted from [12].

In addition, the pre-swirl reduces the total pressure losses between the pre-swirl cavity and the blade firtree and reducing the flow separation area at the inlet of the receiver, which can partially block the channel (see Fig. 1.17 (a)).

The risk of detachment at the inlet of the receiver reaches a maximum when the flow enters the cavity fully axial (in the absolute reference frame, as shown in (a)), while the losses are lower when the relative speed  $w$  is parallel to the receiver channel axis (see Fig. 1.17 (b)).

Correspondingly, the losses decline with a decrease of the angle of attack  $\beta$  [13]. This is illustrated by Fig. 1.18, which shows the discharge coefficient  $C_d$  plotted against  $\frac{w_\theta}{w_{ax}} = \tan \beta$  for different length-to-diameter ratios.

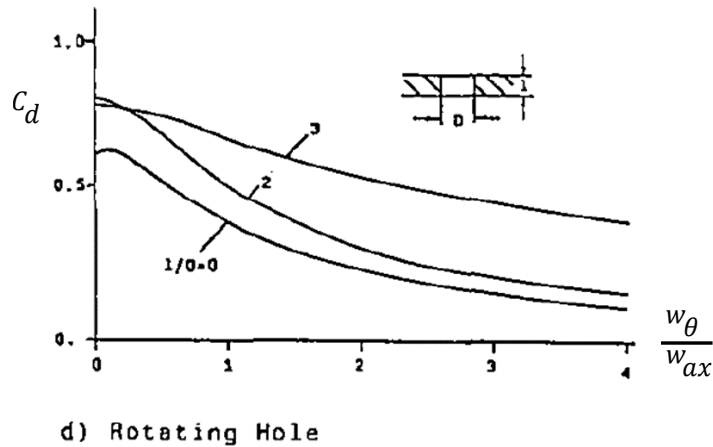


Fig. 1.18: Inlet discharge coefficient for rotating holes [13].

Fig. 1.19 shows a separation bubble at the inlet of a RB caused by a high relative tangential velocity in the pre-swirl cavity.

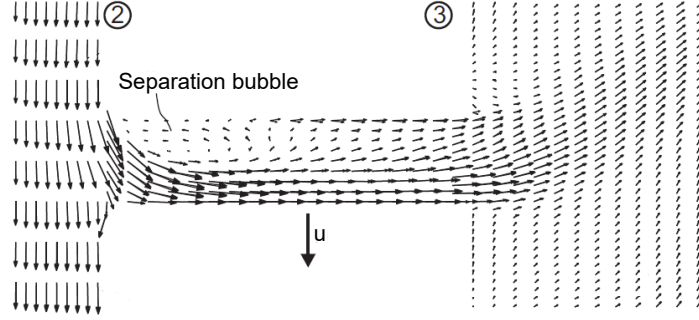


Fig. 1.19: Separation bubble at the inlet of the RB due to high relative tangential velocity in the pre-swirl cavity, adapted from [12].

In the following part, a configuration with pre-swirl of the cooling flow (at the inlet stator-rotor cavity (SR) in front of the receiver) will be compared with a configuration with no pre-swirl.

By applying the Euler eq. [12] between the inlet section (before entering the bore) and the outlet of the bore the following eq. is obtained:

$$\Delta h_t = c_p(T_{t3} - T_{t1}) = u_3 c_{\theta 3} - u_1 c_{\theta 1}. \quad (1.6)$$

Here,  $\Delta h_t$  is the total enthalpy increase due to the pumping through the channel in the rotor frame,  $T_t$  is the total temperature,  $u$  is the rotoric tangential speed and  $c_\theta$  is the tangential speed. In the rotoric frame, the relevant parameter for blade cooling is the total relative temperature  $T_{t3rel}$ , which is linked to the absolute total temperature by the following relation:

$$T_t = T_{trel} - \frac{u^2 - 2uc_\theta}{2c_p}. \quad (1.7)$$

Combining eq. 1.6 with eq. 1.7, the total relative temperature for a given total inlet absolute temperature  $T_{t2}$ ,  $T_{t3rel}$  can be expressed as follows:

$$T_{trel3} = T_{t1} + \frac{2u_3 c_{\theta 3}}{c_p} - \frac{u_1 c_{\theta 1}}{c_p}. \quad (1.8)$$

On the one hand, it becomes evident from eq. 1.8 that in order to minimise  $T_{t3rel}$ , the tangential component of the inlet speed  $c_{\theta 1}$  must be equal to  $u_1$ . On the other hand, in order to maximise the pumping work given by the rotor to the fluid without imposing a negative  $c_{\theta 1}$ , which would lead to excessive losses,  $c_{\theta 1}$  must be equal to zero (see eq. 1.6).

The thermodynamic transformations, which take place in a pre-swirl feed system along an ideal streamline, are shown schematically in the h-s diagrams in fig 1.20.

In a configuration with no pre-swirl, the CA enters the cavity in front of the receiver completely axial at a static pressure  $p = p_1$ . Entering the RB, the relative speed  $\vec{w}_1$  is ideally turned axial, and the dynamic pressure associated with the relative tangential speed is recovered, leading to an increase of pressure.



## 1.6 Flow in rotating cavities

Rotating flow determines the fluid dynamics of numerous secondary air systems including disk cooling and leakages. These 3-D flows can be of an unsteady nature. As previously shown, these internal air systems serve the purpose of impeding the ingestion of mainstream gas into the disk cavities along with supplying the turbine blades and vanes with CA. Owen and Rogers [26] [27] collected a detailed analysis of both experimental and theoretical literature related to rotating flows. The aim of this chapter is to discuss briefly qualitative aspects of the flow field detected in rotor-stator cavities in order to model them correctly.

### 1.6.1 Single disk rotating in a free space

In order to ease the understanding of the complex flow arising in rotor-stator systems, a basic disk rotating in free air shall be examined. As shown in Fig. 1.21, the disk possesses a radius  $b$  and pivots around the  $z$ -axis with an angular velocity of  $\omega$ .

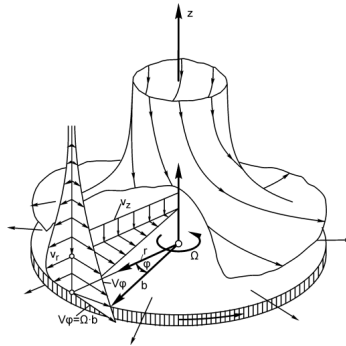


Fig. 1.21: Flow structure on a free disk according to [14].

On each side of the disk boundary layers will evolve, reaching a maximum tangential velocity component  $v_\theta = \Omega r$  at the disk surface, which decreases to zero in the free-stream exterior of the boundary layer. Centrifugal forces induced by the rotating disk make the fluid inside the boundary layer flow radially outwards. The radial velocity component will be zero on the disk surface as well as in the free-stream. Consequently, the external fluid will be dragged away axially into the disk boundary layer. The flow pushed by a spinning disk is named “free-disk entrainment rate” or “free disk pumping effect”.

The flow inside the boundary layer can be of laminar or turbulent nature, which is assessed by the local rotational Reynolds number (eq.1.9).

$$Re_\theta = \frac{\Omega r^2}{\nu} \quad (1.9)$$

Nearby the rotation axis, the flow is typically laminar for all values of omega, whereas with an increasing radius, the flow might become turbulent for large values of omega. Between these two areas, a transition zone will develop. [6]

### 1.6.2 Rotor-stator system without superposed flow

A typical gas turbine configuration consists of a rotating disk located near a stationary casing. This can be modelled by considering the fluid dynamics between

a rotating disc, named rotor, and a stationary disc, named stator. A rotor-stator system is characterised by a rotating disk with a diameter,  $b$ , which rotates at a distance  $S$  from a stationary disk with a comparable diameter, illustrated in Fig. 1.22.

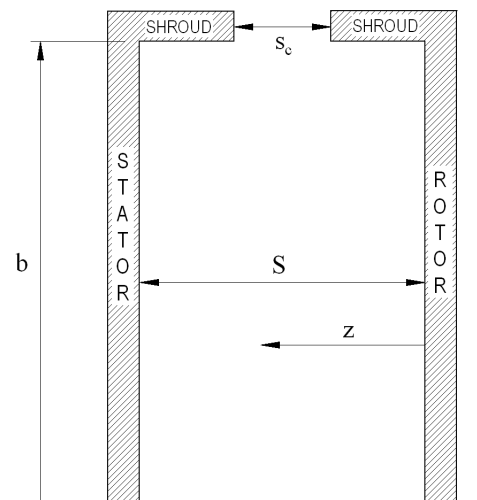


Fig. 1.22: Scheme of a SR cavity [6].

The flow between a rotating and stationary disk is of Batchelor nature, as proven experimentally [6]. This describes a fluid core between the two discs, which rotate with an angular velocity between 0 and  $\Omega$ .

A resulting implication is that two boundary layers would exist: one on the rotor equivalent to that on a free disk and a second on the stator. The latter would include a radial inflow of fluid into the cavity, which contains an efflux of fluid from the boundary layer into the rotating core. Thus, the core flow would be entrained on the rotor boundary layer and out of the system.

The existence of such a core flow was shown by [15], who used laser-doppler anemometry (LDA) to investigate the tangential and radial velocity components in a simple rotor stator system with a stationary shroud. The experiments were conducted under the assumption of no superposed flow-rate and results were taken across the gap. (Here  $z$  is the axial distance from the rotor side as shown in fig 1.22.)

The resulting flow structure was detected to be a turbulent version of Batchelor flow with a radial outflow on the stator ( $z/S = 0$ ), a radial inflow on the stator ( $z/S = 1$ ). Between these two boundary layers prevails an inviscid rotating core. (see Fig.1.23.)

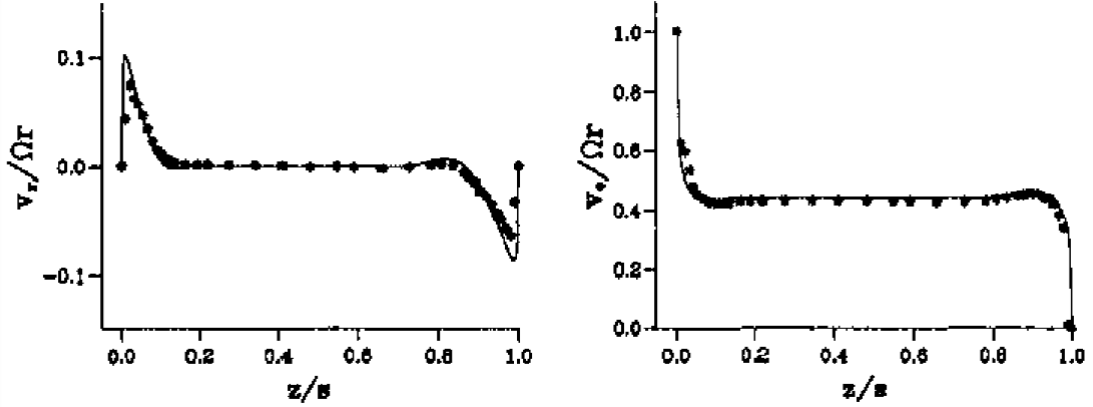


Fig. 1.23: Radial (left) and tangential (right) velocity profiles across a rotor-stator cavity [15].

The radial velocity component takes a value of zero on both the discs and in the core as a result of the viscous forces adjacent to the disk surfaces and the Coriolis forces inside the core.

The turbulent flow structure inside a rotating cavity is influenced by two non-dimensional parameters, assuming that individual boundary layers prevail on either disc. Namely, these parameters are the swirl ratio (eq. 1.10) and the turbulent flow parameter (eq. 1.11). This matter is analysed by [26]. The swirl ratio  $\beta$  is characterised as the ratio of the tangential velocity component  $v_\theta$  inside the rotating core to the angular velocity of the rotor at identical radii  $\Omega r$ .

$$\beta = \frac{v_\theta}{\Omega r} \quad (1.10)$$

The turbulent flow parameter  $\lambda_T$  connects the rotational Reynolds number with the non-dimensional flow-rate, which are both measurable under experiment. The turbulent flow parameter is defined as:

$$\lambda_T = C_w Re_\theta^{-0.8}, \quad (1.11)$$

where  $C_w = \frac{\dot{m}}{\mu b}$  is the non-dimensional superposed flow-rate.

### 1.6.3 Flow regimes in a rotor-stator cavity

A gap Reynolds number, which is shown in eq. 1.12, can be identified for a basic rotor-stator system including a variable axial clearance between the rotor and stator and without a superposed flow. This is done equivalently to the case of the free disk.

$$Re_s = \frac{\Omega s^2}{\nu} \quad (1.12)$$

Here,  $s$  is the axial spacing.

For large values of  $Re_s$ , on at least one of the discs a boundary layer prevails, while a rotating and inviscid core will be developed between them. For small values of  $Re_s$ ,

Couette flow will evolve. Here, a viscous-regulated flow will permeate the entire disk cavity. The flow can still be of laminar or turbulent nature.

Research on a rotor-stator cavity executed by Daily and Nece [16] resulted in the outline of four flow-regimes rooted on the aforementioned theory, as shown graphically in 1.24.

These flow regimes are determined by the rotational Reynolds number,  $Re_s$ , and the axial gap ratio,  $G = \frac{s}{b}$ .

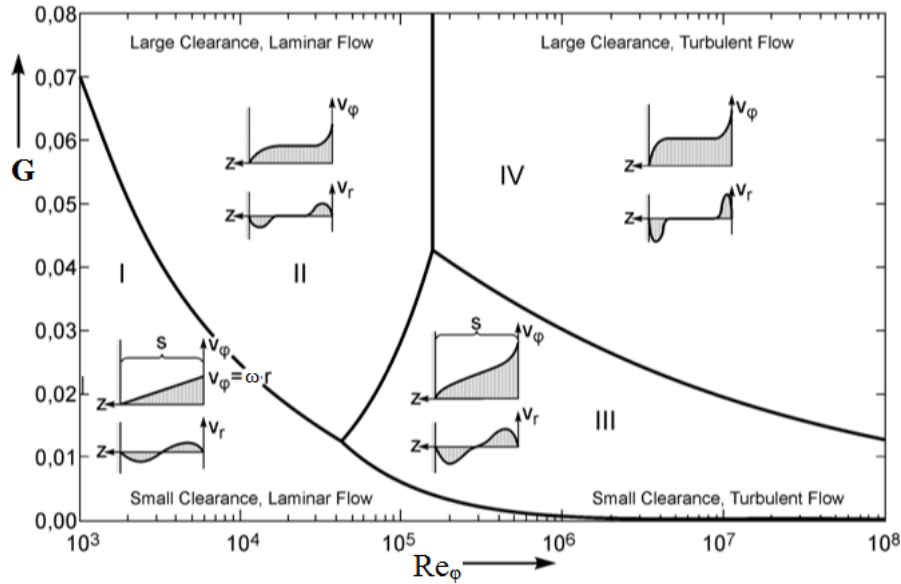


Fig. 1.24: Flow regimes in a SR cavity according to Daily and Nece [16].

- Regime I: laminar flow for narrow spacing (low values of  $G$ ). Flow will be of a Couette type with merged boundary layers on the rotor and stator. For a constant rotational Reynolds number, the frictional heating on the rotor will decrease with an increase in  $G$ ;
- Regime II: laminar flow for larger values of  $G$  and low  $Re_s$ . The flow exhibits a boundary layer on both the rotor and stator, however, now with a rotating core in between the discs;
- Regime III: turbulent flow for narrow spacing, comparable to Regime I;
- Regime IV: turbulent flow for larger spacing, comparable to Regime II;

#### 1.6.4 Rotor-stator system with superposed flow

With a prevailing superposed radial flow in the SR system, the flow can be classified into the same four regimes as discussed in the previous section [6].

In Fig. 1.25, the expected streamlines for a rotor-stator system with a superposed flow are shown.

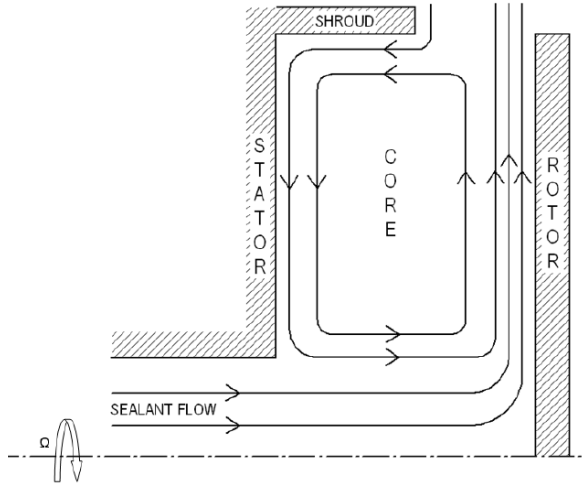


Fig. 1.25: Rotating flow patterns for a rotor-stator system with a superposed flow (based on the CFD analysis described in [17]).

When the pressure in the mainstream flow near the rim seal is higher than in the cavity, an ingress of air occurs. The ingested air flows radially inwards, travelling down the stator boundary layer. Then, the air flows axially across the inviscid rotating core. Subsequently, the flow is mixed with a superposed flow, which enters the system through the center of the stator disc. Ultimately, the flow exits the cavity through the seal clearance. For a rotor-stator system with a superposed flow-rate, the flow conditions not only depend on the rotational Reynolds number,  $Re_\theta$ , and the axial gap ratio,  $G$ , but additionally on the non-dimensional superposed flow-rate,  $C_w$  [6].

The most relevant regimes for this thesis' application are the second and the fourth. Daily et al. [16] measured the tangential component of velocity in a core for a superposed outflow of air. They correlated their results by the relation:

$$\beta = \frac{\beta_0}{12.74\lambda_T\left(\frac{b}{r}\right)^{\frac{13}{5}} + 1}, \quad (1.13)$$

where  $\beta$  is the core swirl ratio and  $\beta_0$  is the core swirl ratio in case of no superposed flow.  $\beta_0$  can be assumed to be 0.5 since Daily et al. [16] did not find a sole dependence on the axial gap width  $G$ . This correlation will be used to model the flow in the SR cavities at the rear disk of the turbine for a relatively small gap.

For a large gap clearance, an inviscid core is expected and the modelling of the core will be discussed in the next section.

### 1.6.5 1-D flow model for the radial core rotation distribution

Since the tangential speed governs the fluid motion, a radial pressure gradient develops inside the cavity, in which the pressure distribution depends on the magnitude and distribution of the tangential velocity. This is shown in the radial equilibrium eq. 1.14.

$$\frac{\partial p}{\partial r} = \rho \left( \frac{v_\theta^2}{r} - v_r \frac{\partial v_r}{\partial r} \right) \quad (1.14)$$

The previous equation is obtained from the radial balance between centrifugal and pressure forces under the assumption of no axial velocity [28].

Due to the dependency of the pressure distribution on the tangential speed, it is necessary to estimate correctly the core swirl ratio in rotor-stator cavity problems in case of flow regimes of type IV.

Will [28] proposed a simplified flow model to compute the radial distribution of the core rotation factor derived from the integral form of the tangential momentum equation. [28]. The model assumes a constant value for the circumferential velocity (“mean value theorem”, according to [29]) along the axial gap width:

$$\frac{1}{r^2} \frac{\partial}{\partial r} (r^2 \int_{z=0}^{z=s} v_r v_\theta dz) = \frac{1}{\rho} (\tau_{\theta z S} - \tau_{\theta z R}). \quad (1.15)$$

Eq. 1.15 is the integral form of the tangential momentum equation, obtained under the hypothesis of steady flow conditions, axisymmetric flow and negligible shear stress resulting from radial gradients of the tangential velocity. Referring to a flow regime of type IV, the circumferential velocity is almost constant in the core region and a significant change appears only within the thin boundary layers. The axial distance with a significant change of  $v_\theta$ , compared to the region with an approximately constant value, can thus be neglected. Clearly, under this assumption, the validity of the model is not verified in case of stronger variations in the velocity profiles for example in the case of flow regime III. Nevertheless, numerical simulations as well as numerous experimental studies have shown that this is an admissible assumption for most cases. [28]

Expanding eq. 1.15 with  $2\pi$  and introducing the core swirl ratio  $\beta$  leads to:

$$\frac{d\beta}{dr} = \frac{2\pi b}{\dot{m}\Omega} (\tau_{\theta z S} - \tau_{\theta z R}) - \frac{2\beta}{\frac{r}{b}}. \quad (1.16)$$

Indicating with  $\tau$  the shear stress and with  $\lambda$  the friction coefficient,

$$\tau = \lambda \frac{\rho}{8} \bar{v}^2, \quad (1.17)$$

the mean tangential velocities for the stator and the rotor are respectively:

$$\begin{aligned} \bar{v}_S^2 &= r^2 \Omega^2 \beta^2 \\ \bar{v}_R^2 &= r^2 \Omega^2 (1 - \beta)^2. \end{aligned} \quad (1.18)$$

Introducing these results into eq. 1.16 and indicating  $\phi_G = \frac{Q}{\pi \Omega b^3}$  as the dimensionless through-flow rate, a correlation for the radial gradient of the core swirl ratio can be obtained:

$$\frac{d\beta}{dr} = \frac{(\frac{r}{b})^2}{4\phi_G} (\lambda_S \beta^2 - \lambda_R (1 - \beta)^2) - \frac{2\beta}{\frac{r}{b}}. \quad (1.19)$$

Assuming for simplicity an equal friction coefficient for stator and rotor ( $\lambda_R = \lambda_S$ ), the limits of eq. 1.19 can be easily seen considering an infinitesimal through-flow (small leakages) and the opposite case of an infinite through-flow:

$$\phi_G \rightarrow 0: \beta = \frac{1}{2} = \text{const.} \rightarrow \frac{v_\theta}{r} = \text{const.} \rightarrow \text{forced vortex}$$

$$\phi_G \rightarrow \infty: \beta r^2 = \text{const.} \rightarrow rv_\theta = \text{const.} \rightarrow \text{free vortex}$$

A forced vortex is characterised by a linear increase of  $v_\theta$  with the radius. In contrast to the latter case, a free vortex is defined by a constant angular momentum. In SR cavities, a pure free vortex or a pure forced vortex structure is seldom found [20].

Therefore, for a correct prediction of the physical behaviour of the flow into the SR cavities and thus, of the pressure distribution, it is necessary to predict correctly the radial gradient of the tangential velocity  $\bar{v}_\theta$ . The prediction must be made depending on the intensity of the radial through-flow, as shown in eq. 1.19.

Once the radial gradient of the swirl velocity inside the cavity  $\frac{d\beta}{dr}$  is chosen, it is necessary to estimate the magnitude of the swirl in the core to obtain the radial distribution of the swirl velocity  $v_\theta(r)$ .

A simplified 1-D model based on the principle of conservation of angular momentum can be employed to obtain a first guess for the magnitude of the core swirl inside the cavity.

Considering a cylindrical control volume in the SR cavity, the principle of conservation of angular momentum leads to the following equation:

$$\sum \dot{m}_{in} r_{in} v_{\theta in} = M_S + M_R + \sum \dot{m}_{out} r_{out} v_{\theta out}, \quad (1.20)$$

where  $M_S$  and  $M_R$  are respectively:

$$\begin{aligned} M_S &= \int \rho \lambda_S \frac{\pi}{4} r^2 \frac{\bar{v}_S^2}{s} dr \\ M_R &= \int \rho \lambda_R \frac{\pi}{4} r^2 \frac{\bar{v}_R^2}{s} dr. \end{aligned} \quad (1.21)$$

The 1-D equation can then be easily discretised along the radial direction and solved iteratively for  $\bar{v}_\theta(r)$ . The final result is a first estimation of the core swirl distribution inside the cavity.

In appendix A.1, a more detailed explanation of the core swirl estimation for a SR cavity, based on the 1-D tangential momentum balance, will be presented.

It must be noticed that due to the momentum transferred from the stator and the rotor to the fluid, a core swirl that differs from zero is always expected in the cavity.

An example of a typical radial distribution of the tangential speed in a SR cavity with a pre-swirl system can be seen in Fig. 1.26: it is possible to observe a swirl distribution similar to a free-vortex flow [12].

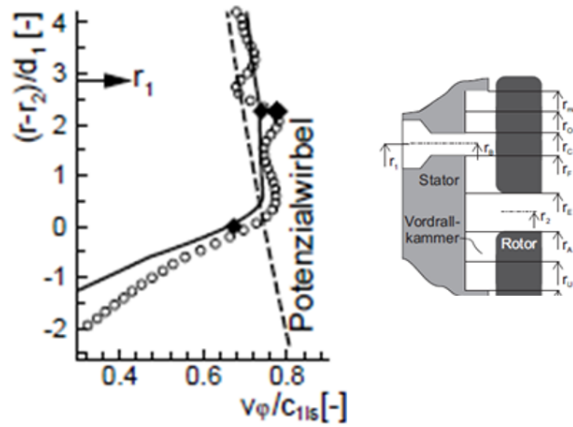


Fig. 1.26: Example of a typical radial distribution of  $v_\theta$  in a pre-swirl SR cavity [12].

## 1.7 1-D flow network

### 1.7.1 Introduction to 1-D flow networks

A physics-based 1-D network is often used to model various components of the SAS lines of a GT since it offers the best compromise of prediction accuracy, cost and speed. Moreover, a 3-D CFD analysis of an entire SAS circuit is neither compatible with the time scheduling of modern design procedure, nor would it be justifiable because of the degree of uncertainty deriving from the assumptions for the boundary conditions. Therefore, a 1-D flow network allows to evaluate several engine configurations or conditions in a reasonably short time [5]. The 1-D network reduces the complex geometry of the different elements of the cooling system to simple values such as a pressure loss coefficient. The reliability of the 1-D computations mainly depends on the empirical correlations implemented in the network, which are based on experiments and CFD analysis. Inside the design frame, a CFD analysis must be used to develop first a better understanding of the flow physics. Additionally, it must be used to reinforce the 1-D flow network, improving the quality of the correlations [20].

A 1-D network consists of two types of elements [18]: the nodes and the connections. The nodes store several values such as pressure and temperature and can represent for example a measurement location or a boundary condition. There are three types of nodes:

- Plenum: elements used to define the boundary conditions of the system.
- Stator Node: a node used for the stationary reference frame;
- Rotor Node: a node used for the rotating reference frame;

The elements that link the nodes to each other are called connections. They describe the change of the node values and represent physical effects. For instance, a pressure loss can be modelled with a pressure loss coefficient. Another example, a SAS component such as labyrinth seals or orifices, can be modelled by connectors, which receive geometrical parameters of the element to be modelled as input.

In the basic approach for the solver, each node contains exactly one pressure and one temperature. In a secondary airflow network, the tangential velocity is of interest, therefore, its value is also stored in the nodes. The information stored in each node result from the solution of the classic equation of continuity, momentum and energy conservation. The solution is obtained accordingly with the characteristics implemented in the connections that link the nodes. For a compressible flow, the momentum equation remains coupled with the energy equation through the density, which is computed using the ideal gas law. Additionally, the modelling methodology also allows the presence of internal choking and backflow.

The building of the flow network describing the SAS line occurs by applying the proper geometry to the models and by connecting them with the proper topology. The modular 1-D code is therefore a powerful tool, which allows modelling the bleed lines from the compressor extraction points to the hot gas section of the turbine meridian channel [5].

An example of a 1-D flow network can be seen in Fig.1.27. The image on top shows a schematic drawing of a simple network. The image on the bottom shows the implementation of the same network in the flow network solver interface.

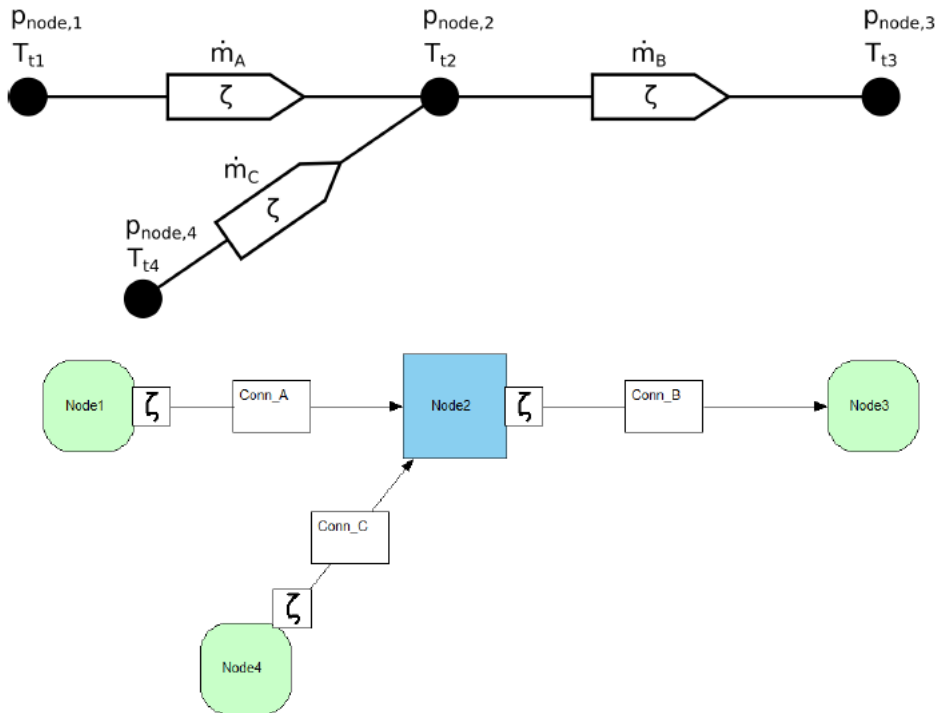


Fig. 1.27: Example of a simple 1-D network (top) and the implementation in the flow network (bottom) [18].

The input and output ports are connected with each other in order to shape the entire secondary airflow network to be analysed. The Plenum nodes are used in the network model to fix the thermodynamic boundary conditions such as total pressure and temperature at the extreme points of the network. Leakage and sealing flows are calculated by lumped-parameter loss-elements using the local static pressure along the hot gas path as boundary conditions. Cooling flows inside blades and vanes are

calculated by a special network element that model the internal flow characteristic. These connectors receive as inputs the blade root static pressure and the thermodynamic conditions of the hot gas at the exit of the cooling circuit and provide as output the CA mass flow [5]. For the 1-D modelling of the flow of a CA feed system as seen in 1.5, it is necessary to sequentially model first the pre-swirl nozzle, then the SR cavity in front of the receiver and ultimately, the flow through the receiver bores in the rotor frame [20]. Due to the importance of the modelling of this system for this thesis' application, a more detailed description will be presented in section 2.4.2.

### 1.7.2 Solver

The 1-D flow network uses the open-source software named CalculiX as a solver. CalculiX (CCX) is a free and open-source finite element analysis software developed by MTU Aero Engines. The software is based on a combination of several programming languages to describe the elements' physics. It implements the root-finding Newton Raphson algorithm as a solver. The solver can handle both linear and non-linear calculations. The task of the solver is the computation of the internal mass flows, pressures and temperatures by solving the equation system of the flow network [5]. The system of equations is properly discretised and solved iteratively according to the numerical scheme implemented. The calculation is considered as converged when the residuum is smaller than a default value set by the user [18]. Hereafter, in Fig. 1.28, a simplified scheme of the solver is presented.

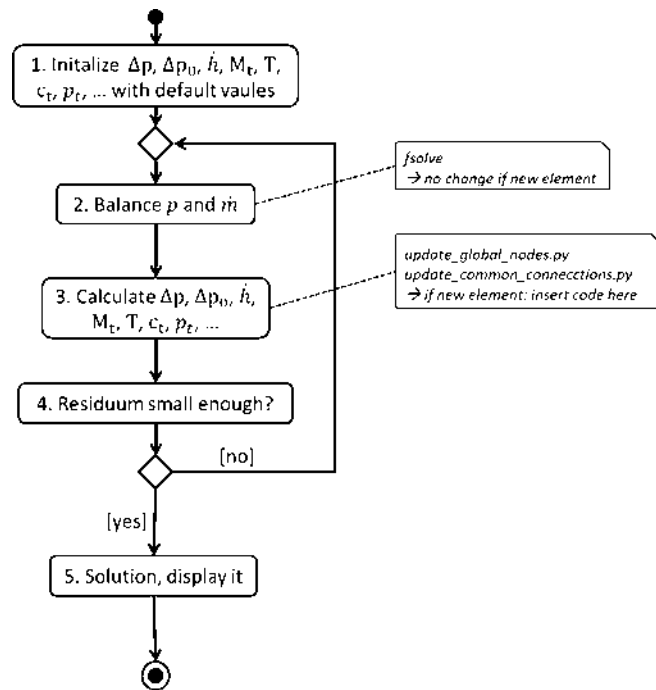


Fig. 1.28: Scheme of the solver implemented in the one-dimensional flow network [18].

## 2 Alternative cooling air feed system design

In this chapter, the different phases of the preliminary design process of the alternative CA feed system will be discussed. First, the functional requirements as well as the boundary conditions are identified and summarised. Furthermore, a preliminary performance analysis is presented. After a literature review, two concepts are defined and analysed using a one-dimensional flow network. The results of the one-dimensional analysis are presented and discussed. Moreover, the results of the SWOT analysis, performed in close contact with the departments of Gas Turbine Integration (GTI) and Mechanical Integrity (MI), are presented and discussed. Ultimately, the most promising concept is chosen. A part-load analysis of the most promising concept concludes the design phase.

### 2.1 Requirements and boundary conditions

In the following sections, the functional requirements as well as the boundary conditions for the CA feed system will be identified and analysed in order to define the actual design task. Moreover, the interfaces along with the geometrical constraints of the system and with the environments will be defined.

#### 2.1.1 Pressure requirements

The primary function of the feed system is to supply the blades and the RHS cavity of the last stage of the turbine with CA, ensuring the required mass flow rate and the required pressure in every GT operation mode. Therefore, the pressure requirements must fulfill two criteria:

1. **No hot gas ingestion into the blade:**

The pressure requirement for the CA at the blade roots is driven by the pressure of the surrounding hot gas. In order to prevent hot gas ingestion into the blades and therefore guarantee proper blade metal temperatures, the cooling air pressure must be higher than the hot gas pressure. Fig. 2.1 shows a typical distribution of the hot gas pressure along the leading edge of a blade.

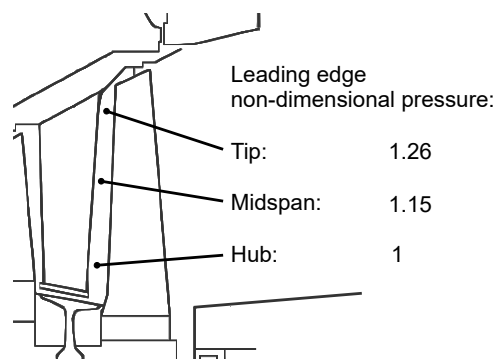


*Fig. 2.1: Example of hot gas pressure distribution along the leading edge.*

The hot gas pressure rises radially from the inner to the outer radius of the blade (see Fig. 2.1) and varies between the pressure and suction side. The

pressure requirement for the CA of the blade follows a simple design rule as shown in eq.2.1.

$$p_{req1} = k_1 p_{hot\ gas} \quad (2.1)$$

The correlation states that the required CA pressure,  $p_{req1}$ , has to be equal to the average hot gas pressure at the leading edge of the blade,  $p_{hot\ gas}$ , multiplied by a constant of proportionality,  $k_1$ , as a safety margin with  $k_1 > 1$ . The pressure distribution inside the blade delivers the value for  $k_1$ .

## 2. No hot gas ingestion into the RHS cavity:

Similarly, hot gas ingestion must be avoided also in the RHS cavities. Therefore, an analogous correlation is used to compute the required pressure:

$$p_{req2} = k_2 p_{hot\ gas}, \quad (2.2)$$

where the constant of proportionality  $k_2$  ( $k_2 > 1$ ) mainly depends on the quality of the sealings between the cavity and the hot gas path.

Finally, the required pressure that must be provided by the alternative feed system was therefore obtained by:

$$p_{req} = \max(p_{req1}, p_{req2}). \quad (2.3)$$

### 2.1.2 Mass flow requirements

The last stage blades of the turbine object of this study are cooled via internal forced convection. In general, the required CA mass flow depends on the temperature of the cooling air itself. However, the mass flow that must be ensured by the alternative CA system has been assumed for simplicity equal to the fraction of CA used in the current feed system to supply the blades of the last stages and to provide the rotor-end disk purge air (see next section 2.1.3). Therefore, the temperature dependency of the blade cooling mass flow was neglected.

### 2.1.3 Rotor-end disk purge air

A secondary goal of the feed system is to guarantee the rotor-end face cooling. The rotor-end face cooling air is currently supplied by the cooling system used for the last two blades, which is intended to be modified. The rotor-end face cooling is essential to ensure that the temperatures of the rotor disk metal stay within acceptable limits. In order to achieve that, hot gas ingestion through the gap between the rear end of the turbine and the Exhaust Gas Housing (EGH) must be avoided during all operation modes. The alternative CA feed system therefore must provide the rotor-end disk purge air, which constantly purges the aforementioned gap (see Fig. 1.14).

### 2.1.4 Summary of boundary conditions and system interfaces

In Fig. 2.2, the boundary conditions and the interfaces of the system are shown schematically.

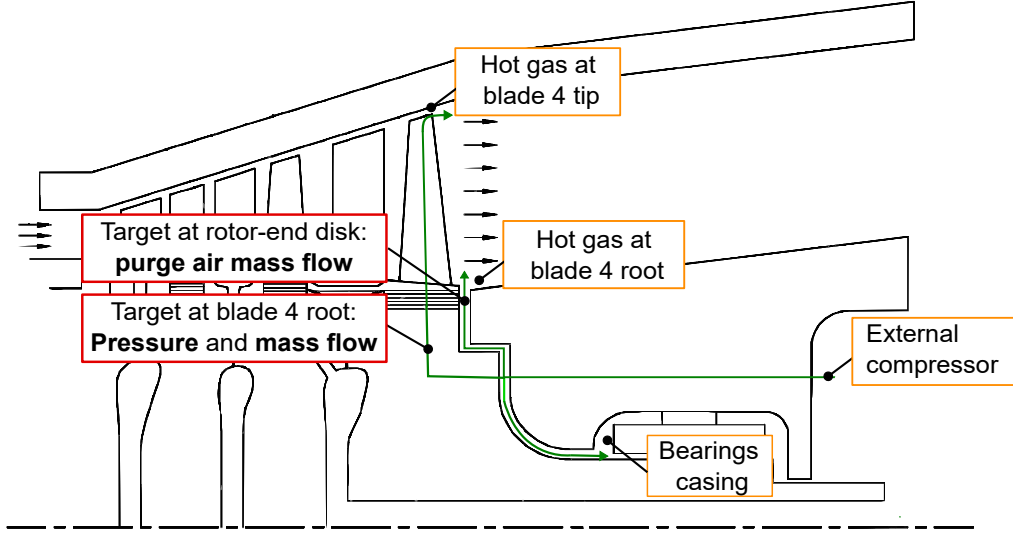


Fig. 2.2: Boundary conditions and design targets of the alternative cooling air feed system, adapted from [8].

In the feed system to be designed, CA must be taken from the environment and compressed to the required pressure ratio using an external compressor. The CA must then be guided through a pipe network into a plenum and then to a cavity between stator and rotor. From the cavity, the main flow must be guided to the blade four firtree in order to enter the cooling channels inside the blades, while part of the CA must be used to purge the rotor-end disk.

To conclude, the feed system has four main interfaces with the surrounding ambient in the GT. The four interfaces, which define the thermodynamic boundary conditions used to set up the one-dimensional flow network, are:

- External compressor: the CA is provided by an external compressor. Considering a system without an inter-cooler between the external compressor and the feed system, total pressure and total temperature of the CA are coupled by the polytropic efficiency  $\eta_p$  of the compressor, as shown by eq. 2.4:

$$\frac{T_{t,out}}{T_{t,in}} = \left( \frac{p_{t,out}}{p_{t,in}} \right)^{\frac{\gamma-1}{\gamma\eta_p}}, \quad (2.4)$$

where  $T_{t,in}$ ,  $p_{t,in}$  are respectively the ambient total temperature and pressure,  $\gamma$  is the heat capacity ratio and  $T_{t,out}$ ,  $p_{t,out}$  are respectively the outlet total temperature and pressure. [2]

The pressure supplied by the external compressor must be regulated according to the required pressure at the roots of blade four. Hence, an important design task is to deliver the cooling air to the blades in the most efficient method, aiming at minimising the pressure ratio and thus, the power required from the external compressor.

- Hot gas path: the rotor-end disk purge air flows from the cavity between stator and rotor into the hot gas path at the intake of the diffuser. Total pressure and temperature at this location are therefore fixed boundary conditions given by the operating point of the GT.

- Bearing casing: in the bearing case, the total pressure is set equal to ambient pressure. The temperature depends on the leakages coming from the cavity between the bearing casing and the rotor-end disk.
- Blade: the aim of the feed system is to supply blade four with the required mass flow and pressure. Total pressure and temperature at the exit of the cooling channels inside the blades are given by the operating point of the GT.

The integration of the feed system into the machine must take into account several design constraints:

- The axial position of the bearing casing should be unaltered in order to avoid substantial modification regarding the length of the rotor.
- Balancing weights in the form of pins and bars are inserted in case of an imbalance of the rotor (see Fig. 2.4). The balance pin holes and bars are located in the rotor-end face and have to remain accessible during the GT outage.
- The temperature inside the bearing casing must be kept below a certain limit. This is necessary to prevent damage to the instrumentation equipment as well as the overheating of leakage oil or oil fog. This temperature is mainly dependent on the cooling air temperature used for the rotor-end disk purge air (see Fig. 2.5). As a consequence, the temperature of the CA coming from the external compressor and thus, its outlet pressure, is limited. The pressure limit must also take into account the ambient temperature as shown in eq. 2.4. Fig. 2.3 shows the non-dimensional outlet temperature as a function of the non-dimensional pressure ratio of the external compressor for different ambient temperatures.

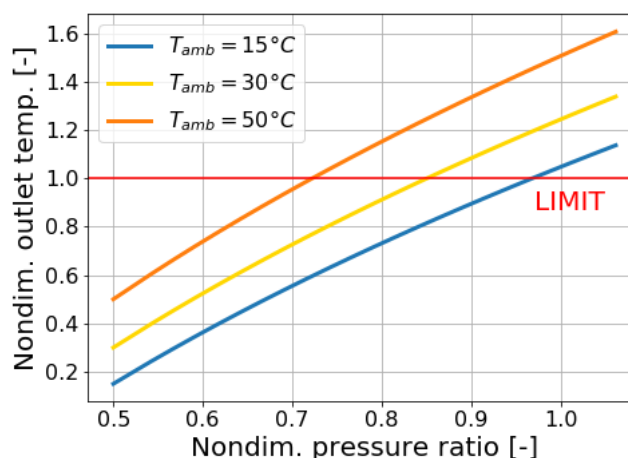


Fig. 2.3: Example of the external compressor map for different ambient temperatures.

- Thermal axial expansion of the rotor must be taken into account from the beginning during the design of the feed system.

- The parts of the new system should be technically feasible with standard manufacturing processes of Ansaldo Energia.

For the reasons mentioned above, the design of the alternative cooling air feed system has been conducted in constant iteration with the team of MI and the team of GTI.

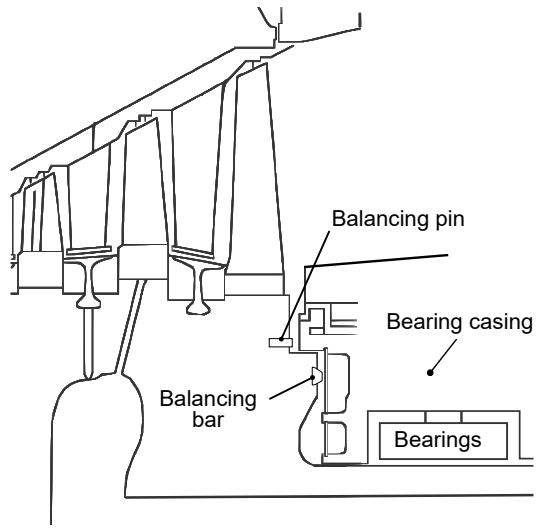


Fig. 2.4: Balancing features.

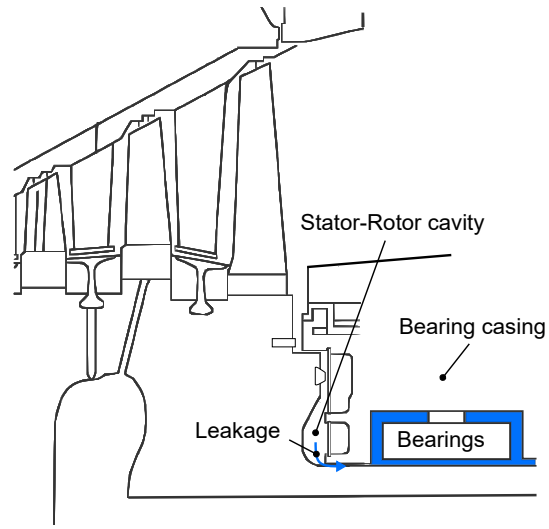


Fig. 2.5: Leakage to the bearing case.

## 2.2 Preliminary performance analysis

A preliminary performance assessment was conducted in order to quantify the performance benefits related to the alternative cooling air feed system subject of this study.

The analysis was conducted using an in-house software, which receives a series of inputs such as the ambient pressure and temperature, the characteristic curves of the turbomachines and the percentage load of the GT. As a result, the tool provides a complete overview of the GT and CC main performance parameters, which are obtained computing global balances of power and mass.

For a better understanding, in Fig. 2.6 (left) a scheme of the current GT configuration (with no external compressor) is compared to a scheme of the GT with the alternative feed system implemented (2.6, right).

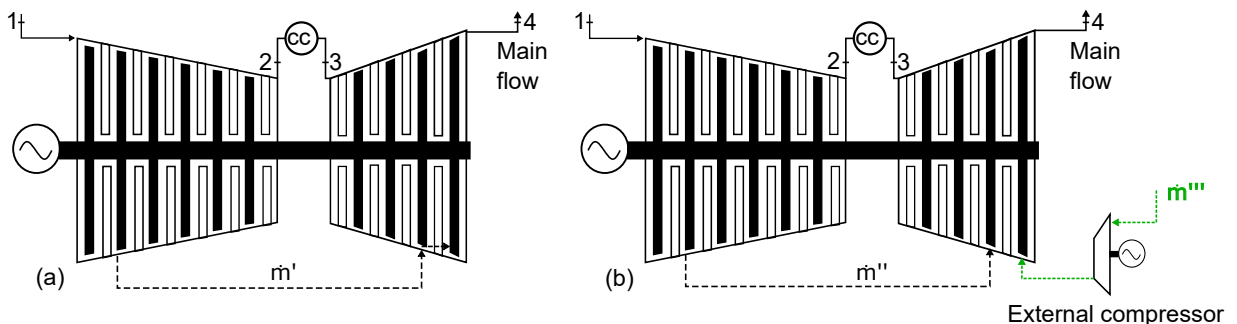


Fig. 2.6: Scheme of the current GT configuration (left) compared with the proposed configuration (right).

In the current configuration, the CA mass flow  $\dot{m}'$ , used to cool the last two stages, is spilled from the GT compressor. A fraction of the spilled mass flow is then used for blade three, while the remaining fraction is used to cool blade four and the rear turbine disk.

For the performance analysis of the GT with the alternative feed system, the cooling mass flow spilled from the GT compressor  $\dot{m}''$  was assumed equal to  $\dot{m}'' = \dot{m}' - \dot{m}'''$ , where  $\dot{m}'''$  is the mass flow elaborated by the external compressor. The elaborated mass flow, the pressure and temperature output of the external compressor assumed for the performance analysis were derived from a preliminary assessment.

Additionally, it must be emphasised that the pressure of the cooling air supplied by the external compressor is lower than the pressure of the bleed supplied by the GT compressor.

In table 2.1, the performance improvement of the engine is shown based on the alternative feed system for blade four in comparison to the standard configuration. The values are expressed as a percentage of the base-load condition.

*Tab. 2.1: Performance analysis.*

GT compressor required power	-0.45%
Turbine power output	+1.82%
GT gross power output	+1.33%
External compressor required power	-0.11%
GT net power output	+1.22%
GT thermal efficiency	+0.2%

From table 2.1 it is possible to observe that the power required by the GT compressor increases. This is due to a reduction of the bleed mass flow ( $\dot{m}'' < \dot{m}'$ ) that leads to an increase of the core mass flow. For the same reason, the turbine power output increases in comparison to the standard configuration.

However, the turbine's power output increases more than the power required by the GT compressor, which results in a positive GT gross power output increase.

The power required by the external compressor has been computed according to eq. 2.5:

$$P_{ext,comp} = \frac{\dot{m}c_p T_{t,amb}}{\eta_C} \left[ \left( \frac{p_{t,out}}{p_{t,amb}} \right)^{\frac{\gamma-1}{\gamma}} - 1 \right], \quad (2.5)$$

where  $\dot{m}$  is the mass flow elaborated by the external compressor,  $c_p$  is the isobaric specific heat capacity,  $T_{t,amb}$  and  $p_{t,amb}$  are respectively the total temperature and pressure at the inlet of the external compressor,  $p_{t,out}$  is the total outlet pressure supplied by the external compressor,  $\gamma$  is the specific heat ratio and  $\eta_C$  is the efficiency of the external compressor, which was assumed.

In the global balance of power, the required power from the external compressor must be subtracted from the GT gross power output to compute the GT net power output. Table 2.1 shows a positive increase of the GT net power with respect to the standard configuration.

Furthermore, both the thermal efficiencies of the GT and the CC increase in comparison to the standard configuration. This preliminary evaluation proves the beneficial impact of the alternative CA feed system on the performance of the whole engine.

### 2.3 Literature review and pre-selection of the basic concepts

The aim of the following chapter is to provide a complete overview of the state of the art of an alternative feed system for the last stage of a heavy-duty GT.

Therefore, a survey of the previous studies and the available literature will be presented. Ultimately, the preliminary concepts will be discussed.

The sources considered were a diploma thesis [19] and a series of internal previous studies.

According to the available sources, the alternative feed systems can be divided into two main categories:

1. feed systems with cover plate,
2. feed systems without cover plate.

#### Cover plate

In order to generate the required pressure for the turbine blade cooling and thus, to reduce the pressure necessary by the external compressor, a concept comparable to a centrifugal compressor has been analysed [19]. The so-called compressor is preferably located between the last turbine stage and the rotor bearing in the exhausts bearing tunnel to use the rotor end face as its hub. The cover plate is used as a shroud for the compressor stage. This concept can be integrated inside the GT in form of:

- cover plate with ribs,
- cover plate without ribs.

The first alternative has a simple blading in form of ribs, as seen in Fig. 2.7. The ribs are part of the cover plate, forming the flow channels with the rotor-end face as the hub. The main advantage of this concept is the ability to guide the cooling flow and to increase the pressure due to the presence of blades in form of ribs [19].

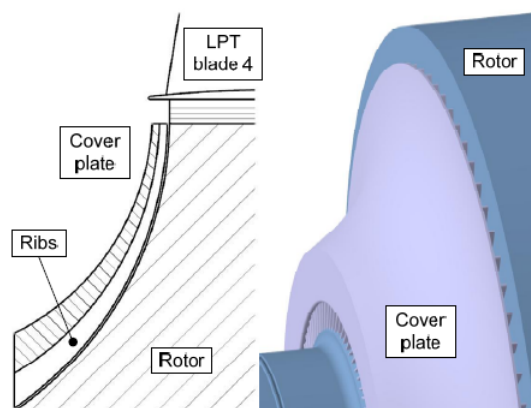


*Fig. 2.7: Cover plate with ribs [19].*

The second alternative is a simple cover plate without ribs (see Fig. 2.8) that uses the operating principle of a Tesla compressor. A Tesla compressor is a device that uses viscous shear forces to transfer torque from blade-less rotoric disks to the fluid and thus, to increase its pressure. These forces act in the boundary layer of the fluid that flows in the gap between two closely spaced disks that are rotating about a central axis. Since the transfer of momentum from the rotor to the air in this option is only performed by friction, the gap between the cover plate and the rotor-end face must be small in order to provide the momentum properly. The resulting centrifugal forces push the air through the flow channel to the outer radius and thereby pressurise it. The twist of the stream is not actively changed since there are no blades in the flow channel. Nevertheless, it is changed due to friction between the channel walls and the air together with the inertia of the gas. The predominant disadvantage of this option is the inability to guide the flow inside the compressor and thus influence the downstream flow angle due to the missing blading. Previous studies have shown that a significant increase of pressure is only possible for low mass flows and have highlighted the difficulties in transferring momentum only with friction. Therefore, a Tesla compressor is not suitable for the last stage feed system. [19]

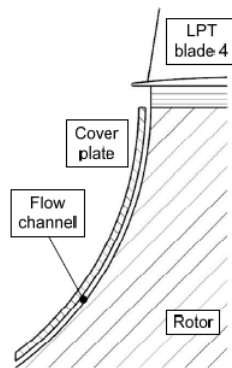


*Fig. 2.8: Cover plate without ribs [19].*

The cover plate of the compressor has to be fixed on the GT rotor in order to transfer the shaft power from the rotor to the CA and thus fulfil the compressor's main function. Different solutions for the fixation of the cover plate were analysed. The most suitable one according to [19] is shown in fig 2.9. In this solution, the cover plate is connected to the rotor with supporting bushes inside the balancing pin holes. The central bore in the bushes allows for the insertion of the balance pins in case they are needed. The bushes have to pierce through the flow channel of the compressor in order to connect the cover plate to the rotor. Therefore, the flow channel is partially blocked. However, this influence can be minimised by an adjustment of size, number and radial position of the balance pins.

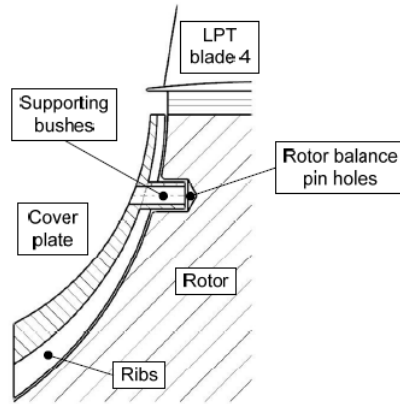


*Fig. 2.9: Example of cover plate fixation via supporting bushes [19].*

## Radial bore

In order to guide and pressurise the cooling air, a concept without cover plate that uses solely bores in the rotor disk, as shown in Fig. 2.10, was analysed. The main advantages of this concept are represented by a simplified design with no additional features such as the cover plate. The principal deficiency of this concept is the inability to guide the flow at the inlet of the receiver, which causes higher losses.

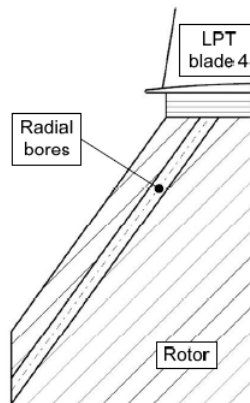


*Fig. 2.10: Supporting bushes [19].*

## Connection to the turbine blades

The CA needs to be guided to the firtrees of blade four. The compressor flow channel therefore has to be connected to the firtrees. This connection can be established in different forms as analysed in [19].

According to [19], the finest solution is a connection with bores obtained in the rotor disk, as shown in Fig. 2.11.

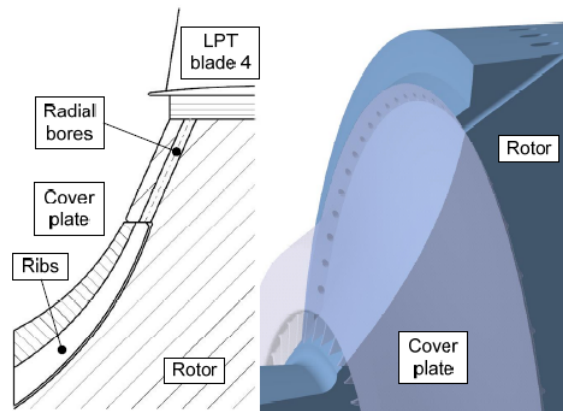


Fig. 2.11: Connection via bores in the rotor disk [19].

The connection of the compressor and the turbine blades via bores in the rotor disk allows for a direct feed of each individual blade in case the RB end directly into the firtrees. Therefore, the number and the diameter of the bores are directly connected respectively to the number of blades and the dimension of the firtree.

Alternatively, the outlet of the bores can be placed in the RHS cavity, allowing to decouple the number of bores and the number of blades. Predominantly, it provides more freedom for the size of the diameter of the bores.

### Preliminary concepts design

A key feature for the design of the feed system was an additional sealing at the outer radius in the SR cavity.

In the alternative feed system, an additional sealing became necessary since the SR cavity is now pressurised by the external compressor. The additional sealing then reduces the leakage flow from the cavity to the main flow path that otherwise would be remarkably higher than the required purge air. This would lead to a higher total mass flow elaborated by the external compressor and thus, to a higher power consumption, diminishing the performance benefits of the system.

For a better understanding, a brief description of the functioning of a labyrinth seal is presented. A labyrinth seal creates a complex flow passage to increase the pressure loss across it and reduces leakage flow rate for a given clearance.

Fig. 2.12 shows the scheme of a labyrinth seal and its position in the feed system.

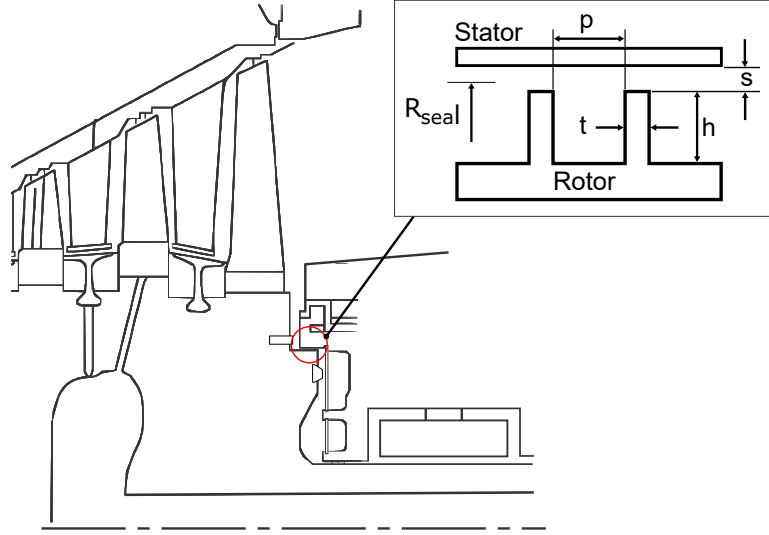


Fig. 2.12: Scheme of a labyrinth seal [20].

For the labyrinth seal geometry shown in Fig. 2.12, Egli [30] proposed the following equation to estimate the mass flow rates of leakages:

$$\dot{m}_{leak} = C_t C_c C_r (2\pi R_{seal} s) \frac{P_{t,in}}{\sqrt{RT_{t,in}}}, \quad (2.6)$$

where  $C_t$ ,  $C_c$  and  $C_r$  are respectively a seal throttling coefficient, a seal carry-over coefficient and seal contraction coefficient.  $P_{t,in}$ ,  $T_{t,in}$  are respectively the total pressure and temperature at the inlet.  $R_{seal}$  and  $s$  are the radial positions of the seal and the radial gap between the stator and the fins. From eq. 2.6 it becomes evident that to enhance the effectiveness of the sealing for a given gap and given inlet total pressure and temperature, its radial position  $R_{seal}$  must be as low as possible. After a series of iterations with the department of MI, two new concepts were developed:

- **Concept 1:** the first solution is represented by a cover plate with ribs. Moreover, RB are used as a connection to the turbine blades. (see Fig. 2.13)

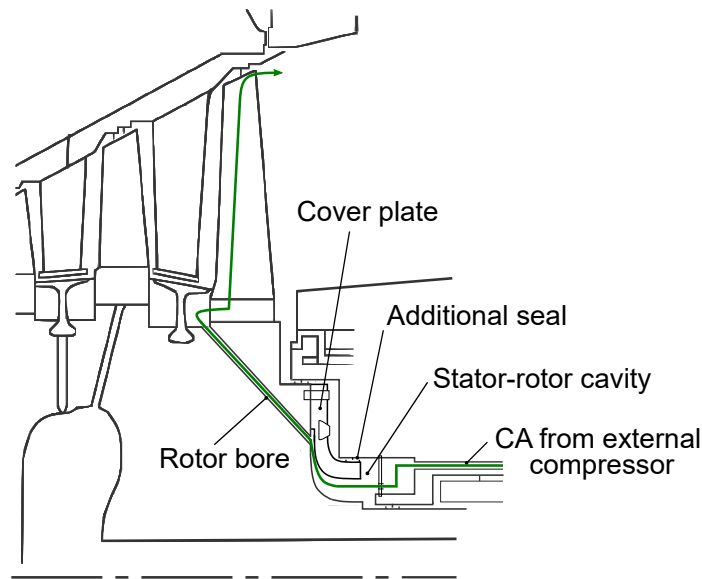


*Fig. 2.13: Concept with cover plate.*

- **Concept 2:** the second solution uses solely RB to feed turbine blades. An additional balcony is added at the rotor-end disk, on which an additional sealing is placed. (see Fig. 2.14)

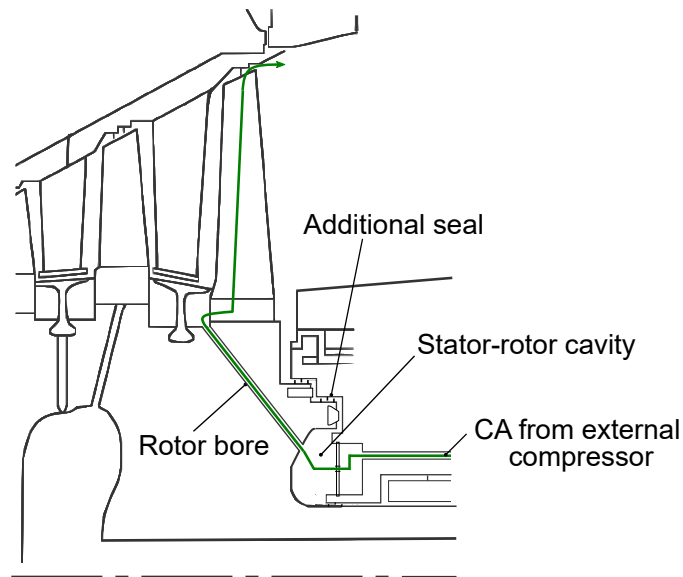


*Fig. 2.14: Concept without cover plate.*

In both concepts, the main target of the design was the additional seal at a low radius with the purpose to reduce the leakages from the cavity between the stator

and the rotor-end disk. A second advantage of the cover plate was the ability of the ribs to guide the flow to the inlet of the receiver bore, reducing the inlet losses.

For concept 1, two different solutions for the fixation of the cover plate were proposed:

1. Fixation via bushes located in the balancing pin holes,
2. Fixation via welding at the outer radius of the cover plate.

For both concepts, the outlet of the bores was located at the rotor heat shield cavity. This solution leads to a larger potential to optimise the size of the RB. Fig. 2.15 shows the air flow path from the RB to the rear part of the RHS cavity and ultimately, to the blades. In order to implement this solution, the channel in the RHS segment (see Fig. 2.15, top left) must be sealed since the two parts of the cavity will be supplied with CA at different pressure.

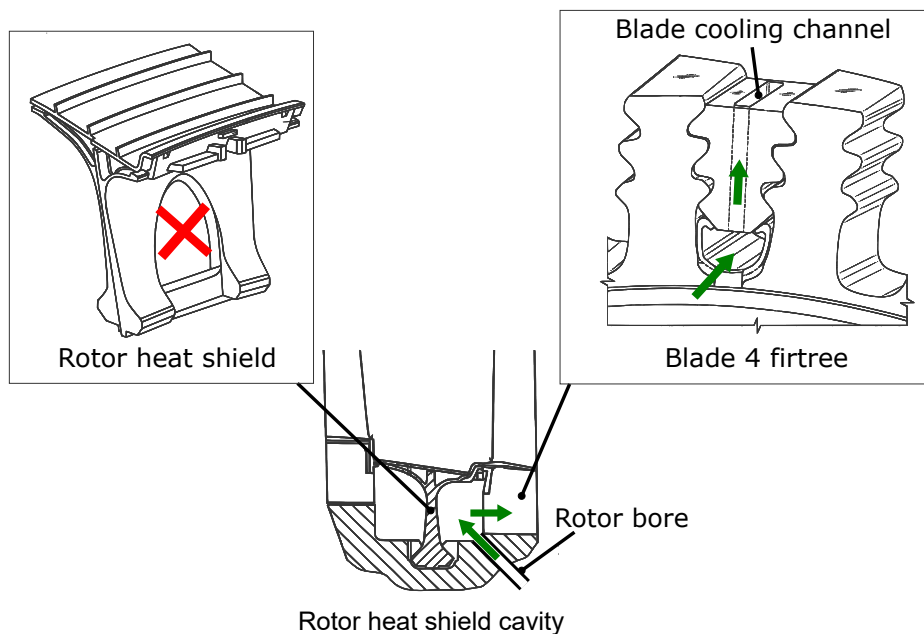


*Fig. 2.15: Cooling air flow at the RHS cavity for the alternative cooling air feed system, adapted from [9] and [10].*

A detailed comparison between the two models will be presented in the following section.

## 2.4 1-D flow network assembly

The two preliminary concepts were modelled using the in-house 1-D flow network "Six" in order to compare and evaluate the required supply pressure to fulfil the mentioned requirements of blade four.

The 1-D flow network assembly is based on a series of assumptions and correlations used as a first best guess. In the second part of the thesis, the results of a CFD analysis of the most promising concept will be shown. The CFD analysis will be used to re-calibrate the one-dimensional model.

Both concepts were analysed in a configuration with a pre-swirl nozzle system (PSN) and a system without pre-swirl (no PSN), as explained in section 1.5. In the configuration with PSN, the PSN was designed to set a swirl ratio approximately equal to 1 in the SR cavity to minimise the losses at the inlet of the RB.

In this section, only the assembly of the 1-D flow network for concept 2 will be discussed, as the method applied for the assembly in the two concepts is equivalent. The network can be divided into two main sections: (i) external line, (ii) internal line.

#### 2.4.1 External line assembly

The external line develops in a piping network outside the thermal block, which originates from the external compressor and ends at the bearing casing after passing through the struts of the Exhaust Gas Housing (EGH). The outlet conditions of the external compressor represent the boundary conditions of the line and have been modelled using a Plenum element, which receives total pressure and temperature as input.

The elements used to model the pipes are simple statoric nodes. The nodes are linked with connectors that implement friction losses and local losses due to bends or changes of cross sections. The losses were implemented in terms of a discharge coefficient according to eq. 2.7:

$$\dot{m} = \frac{C_d A p_{t,in} \phi}{\sqrt{RT_{t,in}}}, \quad (2.7)$$

where  $C_d$  is the discharge coefficient,  $A$  is the cross-sectional area,  $p_{t,in}$  and  $T_{t,in}$  are respectively the inlet pressure and temperature (relative to the previous node) and  $\phi$  is a factor, which describes the compressibility effects and depends on the pressure ratio  $\frac{p_{s,out}}{p_{t,in}}$  across the connection element. The compressibility coefficient is defined as

$$\phi = \begin{cases} \sqrt{\frac{2\gamma}{\gamma-1} \left( \left( \frac{p_{s,out}}{p_{t,in}} \right)^{\frac{2}{\gamma}} - \left( \frac{p_{s,out}}{p_{t,in}} \right)^{\frac{\gamma+1}{\gamma}} \right)} & \frac{p_{s,out}}{p_{t,in}} > \left( \frac{2}{\gamma+1} \right)^{\frac{\gamma+1}{\gamma}} \\ \sqrt{\gamma \left( \frac{\gamma+1}{2} \right)^{\frac{\gamma+1}{\gamma-1}}} & \frac{p_{s,out}}{p_{t,in}} < \left( \frac{2}{\gamma+1} \right)^{\frac{\gamma+1}{\gamma}} \end{cases} \quad (2.8)$$

The discharge coefficient used to model the pressure losses is defined as

$$C_d = \frac{1}{\sqrt{\zeta + 1}}, \quad (2.9)$$

where  $\zeta$  is the loss coefficient derived from the correlations proposed by Idel’Cik [31] and inserted as input for the pressure loss connector. [32]

For the external line, the piping path and the diameters of the pipes were chosen with the goal to minimise the pressure losses and accordingly to the available design space.

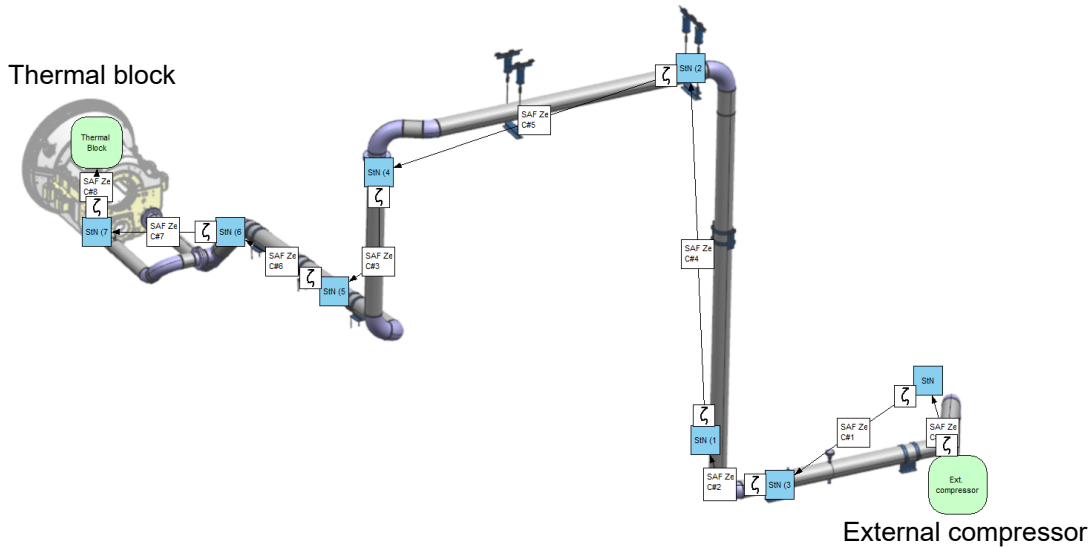


Fig. 2.16: Example of the assembly of the 1-D flow network for the external line.

### 2.4.2 Internal line assembly

The internal line section evolves inside the thermal block. The CA from the external compressor is guided through the external line to a cavity located in the bearing case. From the cavity, the CA flows in the SR cavity through a series of PSNs or simple holes depending on whether the configuration includes a PSN or not. From the cavity between stator and rotor, the flow splits into three branches: the main cooling flow is directed to the RHS cavity through a series of RB, while the remaining mass flow flows partially through the rear-end of the turbine disk to the hot gas path and partially to the bearing case.

In Fig. 2.17, the 1-D flow network for the internal line is shown.

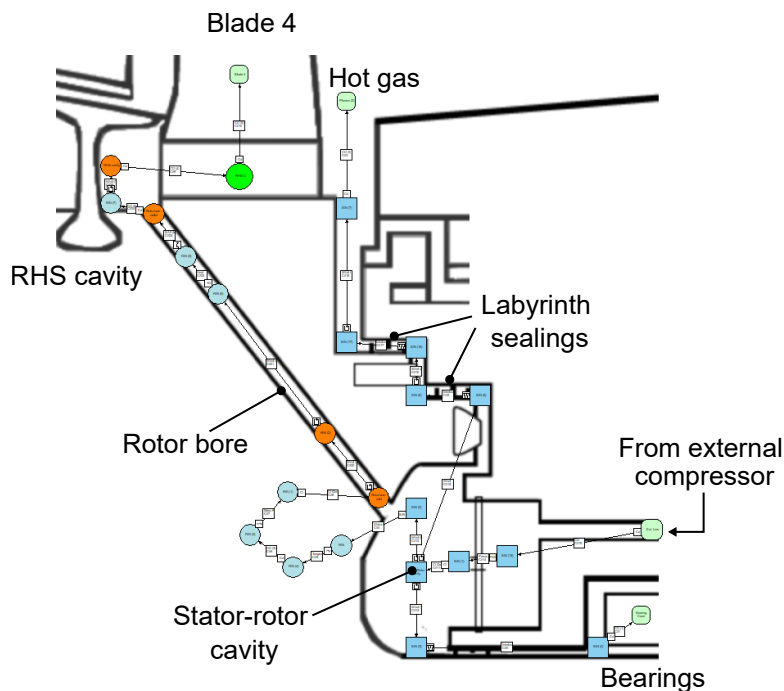


Fig. 2.17: Example of the assembly of the 1-D flow network for the internal line.

Hereafter, the assembly of the components of the internal line will be explained.

### Pre-swirl nozzle

The inflow to the cavity between stator and rotor was modelled using a "pre-swirl connection", which allows to set a swirl angle to the outcoming flow and a discharge coefficient to take into account the pressure losses across this element. For the configuration with no pre-swirl, the swirl angle is set to zero.

The equation implemented in the PSN connection is:

$$c_{\theta,out} = \eta_v \cos(\alpha) \sqrt{2C_p T_{t,in} \left( 1 - \left( \frac{p_{s,out}}{p_{t,in}} \right)^{\frac{\gamma-1}{\gamma}} \right)}, \quad (2.10)$$

where  $c_{\theta,out}$  is the tangential speed at the outlet node,  $\eta_v$  is the efficiency of the swirl generation,  $\alpha$  is the swirl angle, and  $T_t$ ,  $p_t$  and  $p_s$  are the thermodynamic quantities evaluated at the extremities of the connection. [32]

### Stator-rotor cavity

The tangential velocity distribution inside the SR cavity was modelled as a constant  $c_\theta$  distribution using a "Whirl Connection" to link the nodes at different radii. The Whirl Connection calculates the change of  $c_\theta$  depending on the inflow and outflow radius and the inserted vortex exponent according to the following equation:

$$c_{\theta,out} = c_{\theta,in} \left( \frac{r_{in}}{r_{out}} \right)^n, \quad (2.11)$$

with  $n$  as the vortex exponent:

$$n = -1 \rightarrow \text{free vortex,}$$

$$n = 1 \rightarrow \text{forced vortex (rigid body rotation).}$$

The SR cavity is characterised by a relatively large axial gap and moreover, a small radial through-flow is expected. Therefore, a constant  $c_\theta$  was assumed and modelled with  $n = 0$ .

For the configuration with no pre-swirl, a "swirl-generator element" was added. This element introduces a tangential velocity in the cavity, necessary to model the swirl induced by the rotor. The swirl-generator connection simply sets a defined value for the tangential speed, in similarity with a PSN connection. [32]

The value of the swirl velocity of the core flow inside the cavity was evaluated from an integral 1-D momentum balance as mentioned in 1.6.5 and detailed in the appendix A.1.

The magnitude of the swirl as well as the exponent implemented in the cavity will be re-calibrated according to the results obtained from the CFD analysis.

Fig. 2.18 shows the SR cavity of the internal line in a detailed way.

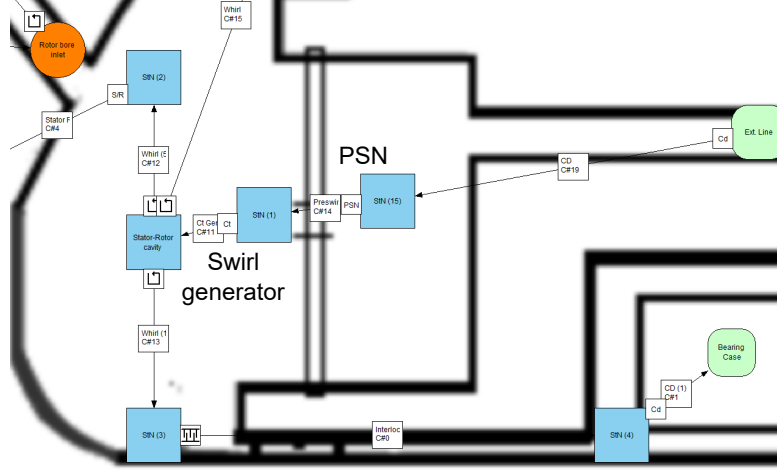


Fig. 2.18: Detail of the 1-D flow network at the SR cavity.

## Rotor bore

From the SR cavity, the cooling air flows into a rotating bore. Thus, the reference frame must pass from the absolute to the relative one, which was modelled by a "Stator/Rotor" connection. The "Stator/Rotor" connection was necessary to avoid an undefined behaviour of  $T_t$  when the reference frame changes. For instance, for the change from a stator node to a rotor node eq. 2.12 was implemented [32].

$$T_{t,rel} = T_t + \frac{u^2 - 2uc_\theta}{2c_p} \quad (2.12)$$

In addition, a "Tangential Dynamic Pressure Recovery" connection was required in order to model the recovery of the relative tangential speed. This connector allows to compute the pressure recovery based on the tangential velocity  $c_\theta$  respectively  $w_\theta$ , depending on the reference frame.

In particular, for the rotating frame of reference, the equation implemented in the connection is the relationship for isentropic compressible flows [32]:

$$p_{out} = p_{s,int} \left( \frac{T_{t,rel}}{T_{t,rel} - \frac{w_\theta^2}{2c_p}} \right)^{\frac{\gamma-1}{\gamma}}, \quad (2.13)$$

where  $p_{out}$  is the total pressure after the recovery and  $p_{s,int}$ ,  $T_{t,rel}$ ,  $w_\theta$  are respectively the static pressure of the inlet node, the relative total temperature and the tangential component of the relative speed.

The losses at the inlet of the rotating bores were modelled by a discharge coefficient element (as seen for the losses in pipes). The value of the discharge coefficient derives from empirical and numerical correlations property of Ansaldo Energia. For a given mass flow through the bore and thus, for a given axial speed, the value of the discharge coefficient mainly depends on the swirl ratio in the SR cavity that defines the angle of attack  $\beta$ . The PSN, as seen in section 1.5, leads to a higher swirl ratio in the SR cavity and thus, to a higher discharge coefficient if compared to the configuration with no PSN, as shown in Fig. 2.19.

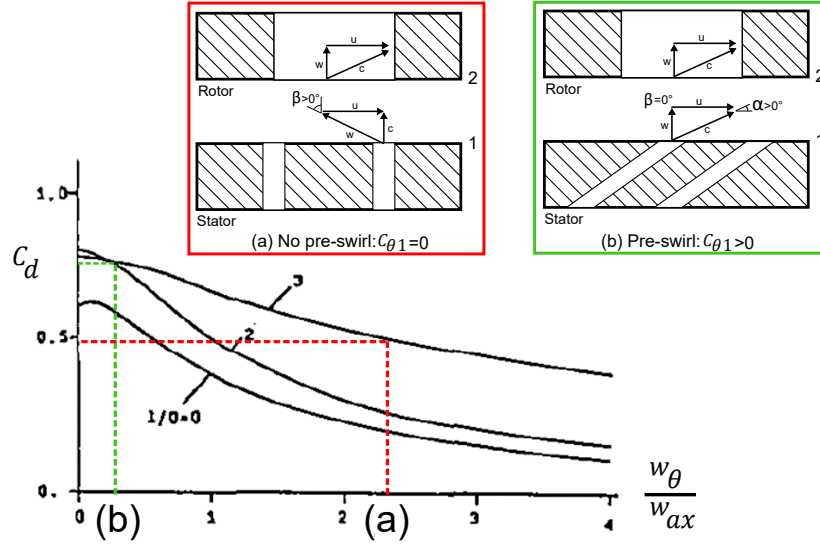


Fig. 2.19: Example of discharge coefficients at the RB inlet, adapted from [12] and [13].

When the CA enters the rotating bore, it assumes the state of a solid body rotation. This was modelled using a swirl-generation connection followed by a whirl element with a forced vortex exponent ( $n=1$ ). The swirl-generation connection allows to set a tangential speed equal to the rotational speed at the radius of the receiver ( $r$ ) bore according to the following equation [32]:

$$v_{\theta} = \omega r. \quad (2.14)$$

An additional control node was inserted between the inlet and the outlet of the bore. This node provides the value of the total relative pressure at the inlet of the bore after the losses. The radial position of the nodes mainly depends on the length of the bore interested by the losses induced by the inlet section. For the preliminary analysis, a radial position that corresponded to a distance of two diameters was chosen. The position of the intermediate nodes as well as the discharge coefficient used to model the inlet losses will be tuned according to the CFD results. Fig. 2.20 shows a detail of the flow network at the inlet of the bore.

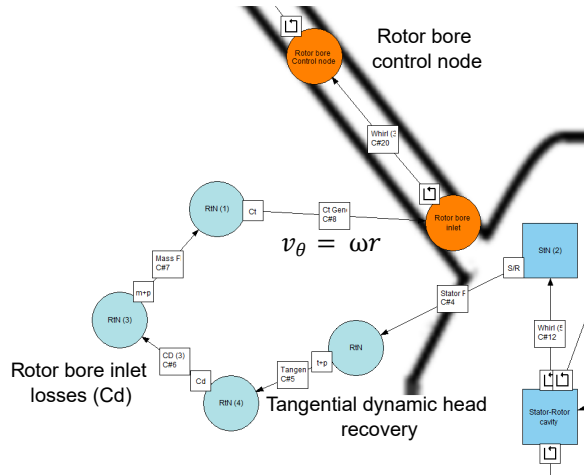


Fig. 2.20: Detail of the 1-D flow network at the RB inlet.

A "heat pick-up" connector was used to model the heat pick-up due to convection along the bore. The Heat Transfer Coefficient (HTC) was obtained from the Dittus-Boelter correlation valid for turbulent flows in pipes [33]:

$$Nu = 0.023Re^{0.8}Pr^{0.4}, \quad (2.15)$$

where  $Nu$  is the Nusselt number,  $Re$  and  $Pr$  are respectively the Reynolds number and the Prandtl number. Once the HTC was estimated, it was possible to compute the convection heat pick-up according to the following equation [33]:

$$\dot{Q} = HTC[A(T_{metal,avg} - T_{fluid,avg})]. \quad (2.16)$$

Here,  $A$  is the inner surface of the RB,  $T_{fluid,avg}$  is the bulk average cooling air temperature that results from the 1-D computation and  $T_{metal,avg}$  is the estimated average metal temperature based on previous investigations. In order to model the losses due to friction inside the bore, a friction connection was inserted. To obtain the value of the friction coefficient  $\zeta$ , the bore was considered as a straight pipe and the flow as turbulent. In Fig. 2.21, a detail of the flow network at the RHS cavity is shown.

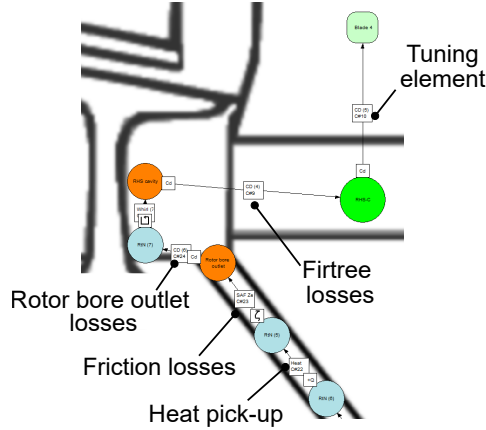


Fig. 2.21: Detail of the 1-D flow network at the RB outlet.

### Rotor Heat Shield Cavity and blade's firtree

From the rotor bore, the air flows into the RHS cavity. Due to its large volume, the RHS was approximated as a plenum, with  $p_{trel} \approx p_s$  under the assumption of  $w_\theta \approx 0$ . Therefore, the flow from the RB to the RHS cavity was modelled as a discharge into a plenum, using a discharge coefficient connection  $C_d$  to take into account the losses caused by the abrupt change of the cross-sectional area.

The friction coefficient to be implemented can be estimated by the so-called Borda-Carnot correlation [31]:

$$\zeta = \frac{\Delta p}{\frac{\rho w^2}{2}} = \left(1 - \frac{A_{in}}{A_{out}}\right)^2, \quad (2.17)$$

where  $A_{in}/A_{out}$  is the cross-sectional flow area ratio of the abrupt expansion.

In particular, the assumption of an infinite discharge area was made, leading to a  $\zeta = 1$ , according to eq. 2.17. This means that from the RB exit to the RHS cavity, one dynamic head was expected to be lost.

The change of radius in the cavity was modelled by two rotoric nodes, connected by a whirl element. For the whirl element, the assumption of constant tangential velocity along the radial direction was made since a high value of radial through-flow rate was expected. Therefore, a vortex exponent  $n = 0$  was implemented in the swirl connection.

The flow from the RHS cavity to the blade's firtree was modelled using a discharge coefficient connection placed between the node at the outer radius in the cavity and the node corresponding to the blade's firtree. The value of the  $C_d$  implemented in the connection was evaluated assuming a simple flow restriction.

An additional discharge coefficient connector was added between the Plenum, used to define the hot gas boundary conditions, and the node of the firtree. The connector was used to tune the cooling mass flow through the blade. The cross-sectional area  $A$  (see eq. 2.7) was manually inserted to obtain the correct mass flow for every computation.

### Rotor-end disk purge air

A fraction of the CA in the SR is forced in the radial direction towards the hot gas main path by the high pressure ratio. This CA is required to cool the rear part of the disk and to avoid hot gas ingestion. The purge air was modelled as a line that branches out from the SR cavity node and ends in a Plenum element. The Plenum contains the total pressure and temperature of the hot gas and therefore, represents the boundary condition of the line.

The labyrinth seals were modelled using elements that receive geometrical parameters as input such as the number of fins and the length of the gap. The elements compute as output the mass flow similar to a discharge coefficient element.

In order to model the flow field in the cavity between the sealings, the correlation 1.13 was used, while in front of the lock plate of the blade the core swirl motion was modelled as a free vortex ( $n=-1$ ).

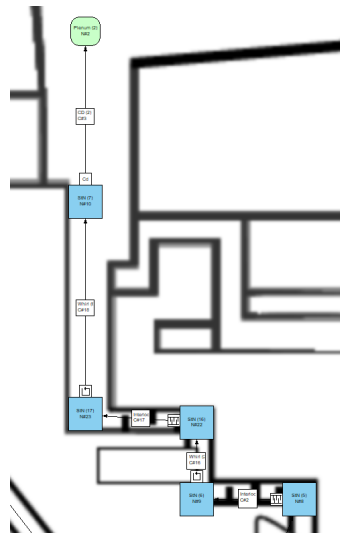


Fig. 2.22: Detail of the 1-D flow network at the labyrinth sealings.



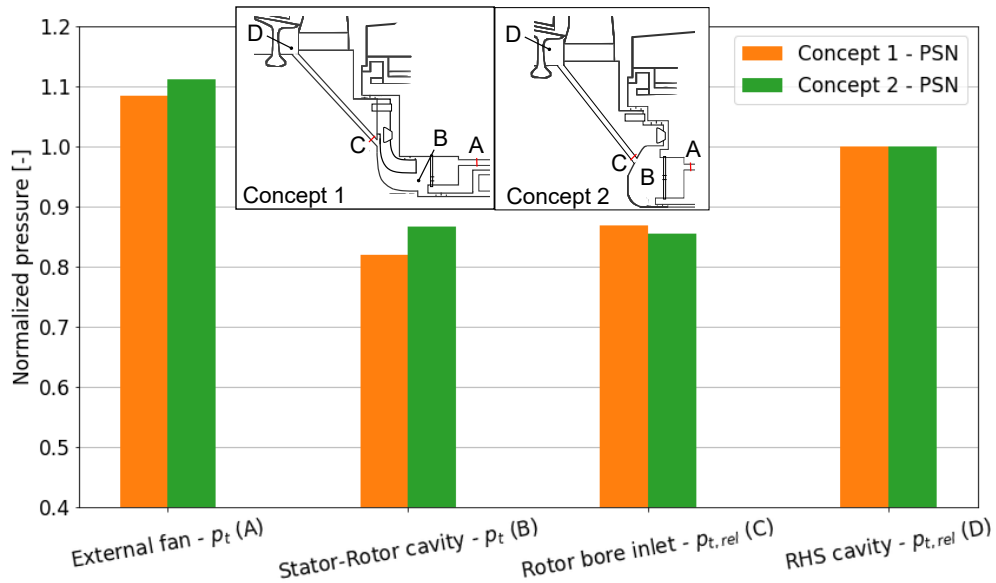


Fig. 2.25: Pressure distributions for concept 1 and concept 2 for a PSN configuration.

In Fig. 2.26, for concept 2 the configuration with PSN is compared to the configuration without PSN.

The pressure required from the external compressor with PSN is significantly higher than the required pressure without the PSN. This is due to the fact that a PSN requires a pressure ratio between inlet and outlet to provide an adequate swirl to the CA in the cavity in front of the receiver. The configuration without the PSN leads to a higher pressure at the inlet of the receiver as a result of the recovery of the tangential dynamic head. Nevertheless, this leads to higher inlet losses at the RB. A correct estimation of the inlet losses is therefore fundamental in order to predict a physically correct behaviour of the system.

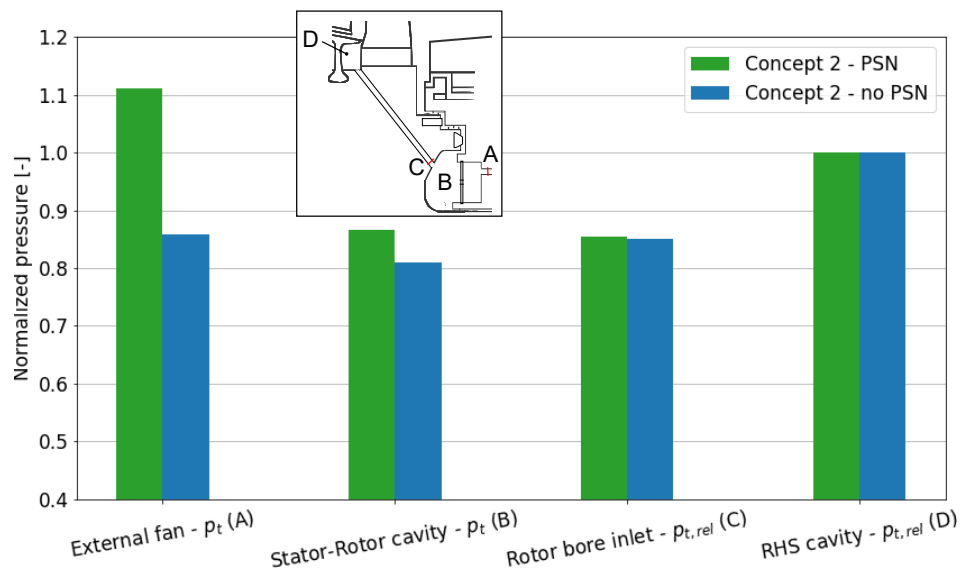


Fig. 2.26: Comparison configuration with and without PSN for concept 2.

As seen in section 2.1, one of the main design constraints that must be considered for the design of the feed system is the temperature at the bearing case. The solution including the PSN would lead to a higher temperature at the bearing casing due to the high supply pressure required by the external compressor. Therefore, the solution without PSN was chosen as the most promising configuration.

## 2.5 SWOT analysis

The SWOT analysis was developed as a simple, effective tool to analyse the insight and the outlook of a project and to build the framework for analysing Strengths, Weaknesses, Opportunities and Threats (SWOT) of the project [34].

By performing a SWOT analysis for both of the concepts, it was possible to choose the most promising concept. Additionally, the analysis helped to raise the awareness of multiple factors that might affect future developments.

The analysis involved the departments of MI and GTI and considered a large number of aspects such as performance, feasibility, costs and complexity of the design.

In conclusion, although the concept with cover plate showed higher performance benefits, the concept without the cover plate was judged as the most promising solution for an alternative CA feed system for the last turbine's stage blades.

## 2.6 Part-load analysis

The functional requirements of the alternative CA feed system must be met during all the operation points of the GT. Therefore, it is necessary to evaluate the robustness of the most promising concept also during part-load operation conditions.

The so-called VIGV-TAT corner point operation mode represents a critical condition for the feed system, which supplies the last two stages. The VIGV-TAT corner point operation mode is defined as the operation condition, in which the TAT target value is reached while the VIGVs are still closed during the loading/de-loading part-load operation phases of the GT. Fig. 2.27 shows a scheme of the loading operation phase of the Ansaldo GT 26.

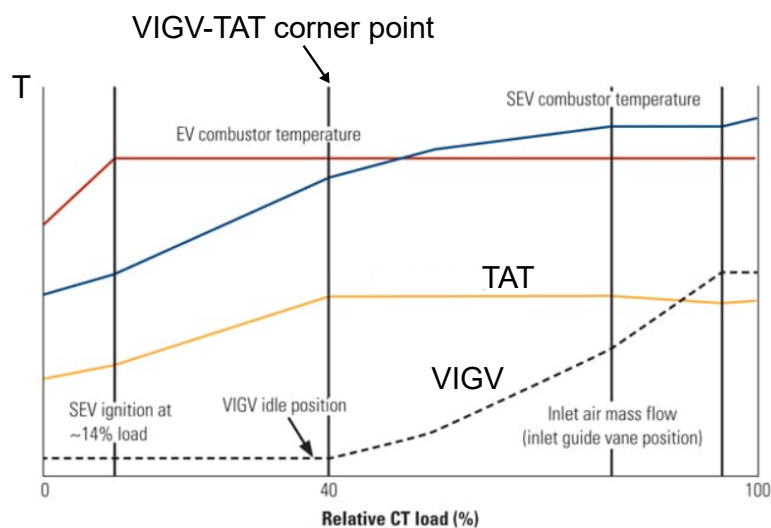
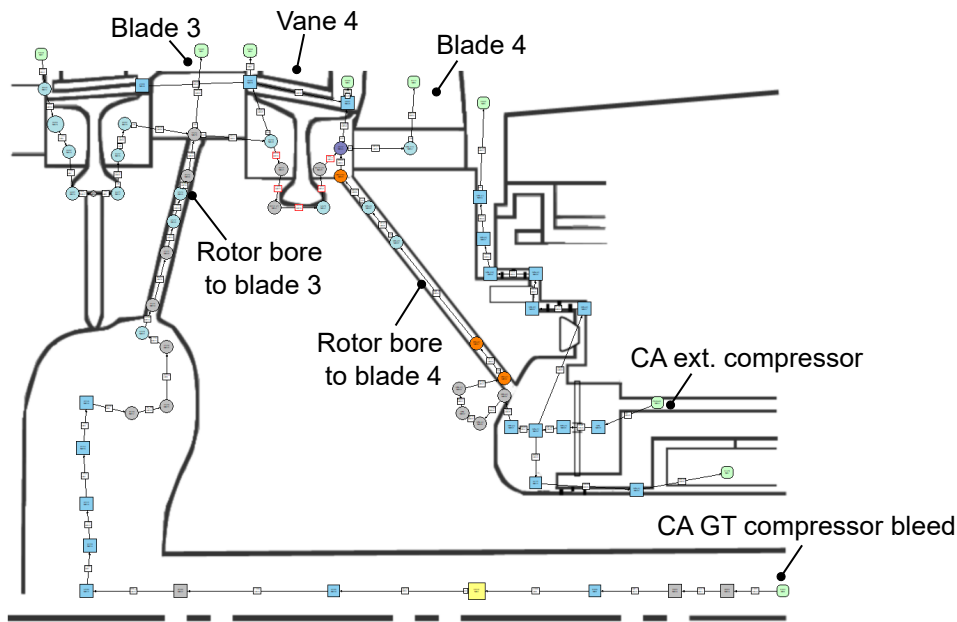


Fig. 2.27: Ansaldo GT 26 loading operation phase.

In the alternative feed system, blade four is fed from the rear part of the RHS cavity

to the firtree through a channel. However, the front part of the RHS cavity is still supplied by CA, which is extracted from the GT compressor. Since the VIGVs of the GT compressor at VIGV-TAT corner point are still closed, the bleeding pressure is notably lower than at base-load. Consequently, a lower pressure of the bleeding flow leads to a lower pressure in the front part of the RHS cavity. Therefore, to obtain a more precise estimation of the pressure at the firtree of blade four at VIGV-TAT corner point operation mode, it is necessary to include the leakages into the model. The 1-D flow network of the internal line, which models the alternative feed system object of this study, was then integrated into the flow network of the system currently supplying the blades of the penultimate stage of the turbine. Thus, a complete 1-D flow network of the CA feed system for the blades of the last two stages of the turbine was obtained. A scheme of the flow network is represented in Fig. 2.28.



*Fig. 2.28: Complete 1-D flow network of the cooling air feed system for the blades of the last two stages of the turbine.*

This thesis covers the preliminary design phase of an innovative CA feed system. For that reason, further assumptions regarding the behaviour of the external compressor were necessary in order to start the design loop. Once the pressure and mass flow required by the system will be fixed with more precision, it will be possible to choose the hardware and consequently remove these assumptions. First, no control systems for the external compressor were assumed to reduce the overall complexity. Therefore, the external compressor was assumed to work at constant rotational speed. Moreover, the back-pressure of the cooling line seen by the external compressor at part-load was expected to be lower than at base-load. Consequently, the equivalent user characteristic curve of the cooling line can be sketched as shown in Fig. 2.29. For the evaluation of the operation point of the external compressor, its characteristic was strongly simplified, as shown in Fig. 2.29. As a result, the mass flow elaborated at part-load was assumed to be equal to the mass flow required for base-load.

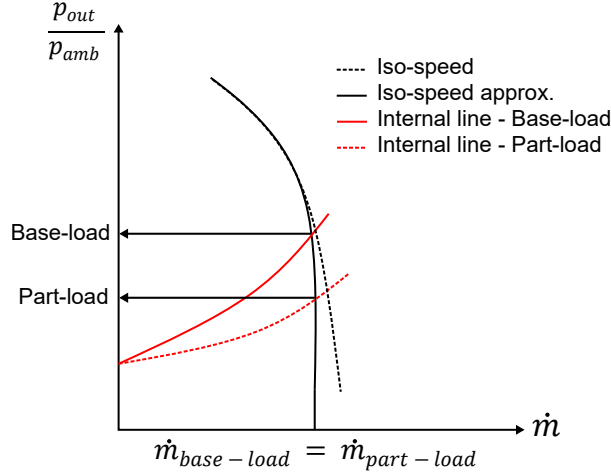


Fig. 2.29: Scheme of the simplified characteristic map assumed for the external compressor.

The boundary conditions for the VIGV-TAT corner point were applied to the flow-network. The pressure at the Plenum node, which models the pressure supplied by the external compressor (see section 2.4.2), was tuned to obtain the target mass flow rate elaborated by the external compressor under the above mentioned assumptions. The results of the 1-D flow network at part-load case are summarised in the following table. The values are expressed as a percentage of the base-load case.

Tab. 2.2: Part-load analysis.

RB mass flow	+13.6%
Rotor-end disk purge air mass flow	-40%
Bearing casing leakage mass flow	+1.33%
Blade 4 firtree pressure	-35%

These quantities were used as boundary conditions for the CFD assessment. The discharge coefficient at the inlet of the bore was modified according to the flow conditions expected for part-load in the SR cavity. In particular, a higher mass flow and thus, a higher  $w_{ax}$ , was computed. Therefore, a smaller angle of attack  $\beta = \text{atan}\left(\frac{w_t}{w_{ax}}\right)$  was estimated, which led to a higher discharge coefficient, according to the correlation mentioned in 2.4.2. However, the value of the discharge coefficient will be re-calibrated to match the results of the CFD evaluation.

In Fig. 2.30, the distribution of total relative pressure at part-load is compared with the distribution at base-load.

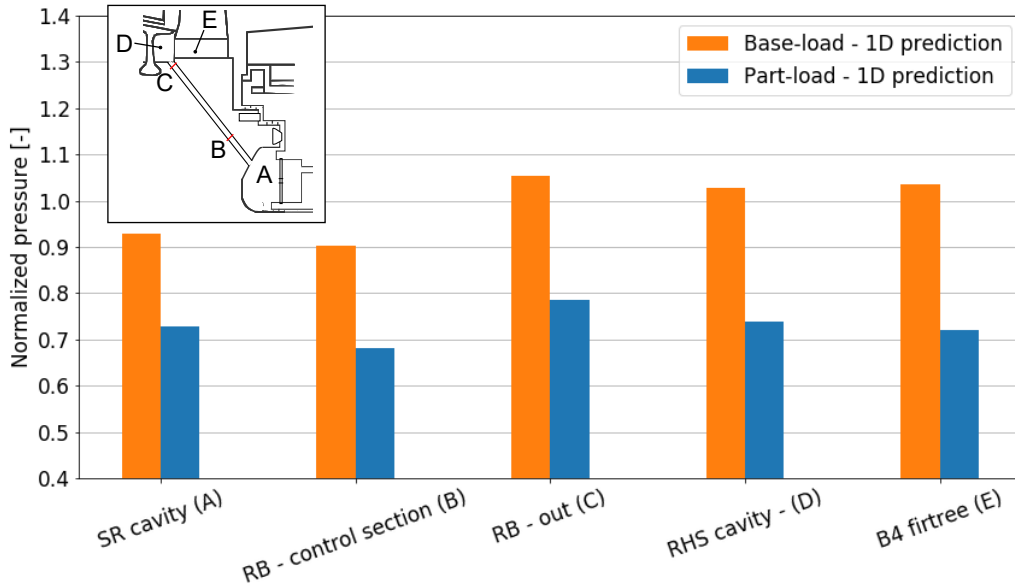


Fig. 2.30: Total relative pressure distribution at base-load and part-load.

At part-load, the pressure difference between the blade's firtree and the SR cavity is lower compared to the base-load case. This is mainly due to the fact that the mass flow in the part-load case is higher than the one at base-load. Additionally, the cooling flow at part-load is supplied at a lower pressure and thus, at lower density, which results in higher velocities. Therefore, the losses in the part-load case are in absolute value higher than the losses at base-load case. The CFD analysis elaborated in the next chapter will be used to conclude the study and re-calibrate the one-dimensional network for base-load and part-load.

### 3 Computational Fluid Dynamics analysis

The 1-D flow network analysis provides a robust and fast criterion to model internal flow systems of a GT. However, the accuracy and reliability of the results strongly depend on the empirical correlations, which are used to model the complex 3-D features typically present in such flows. CFD provide a numerical prediction of the distributions of velocity, pressure, temperatures and other relevant properties over the entire calculation domain. [20]

The CFD analysis is therefore a powerful tool that can be employed to develop a better understanding of the single component flow physic, reinforcing the 1-D modelling. In particular, CFD plays two fundamental roles for the modelling of SAS flow networks: [20]

- CFD provides a quantitative assessment of friction factors, discharge coefficients and loss coefficients, which then become input for the 1-D flow network models.
- CFD provides a flow field visualisation that helps to understand the key features of the flow field, which are not easily discernable.

First, a brief description of the fluid domain and the mesh generation process will be presented. Then, the computational set-up and the boundary conditions will be examined. Finally, the mesh sensitivity study will be presented.

#### 3.1 Fluid domain

A complete 3-D model of the selected concept was created in CAD using the software Siemens NX. The main object of the preliminary CFD analysis is the investigation of the flow field in the SR cavity between the bearing case and the rear part of the rotor, the flow through the RB and the flow field in the rear part of RHS cavity.

Additionally, in order to reduce the complexity and the number of cells, only a sector of the complete fluid domain was considered for the CFD analysis. The sector includes only one RB and was obtained by slicing the entire fluid domain with two  $r - z$  symmetry planes, which define an angular sector of  $360^\circ/N$ , with  $N$  as the number of RB. Therefore, a simplified 3-D model of the fluid domain was created.

In Fig. 3.1, a sketch of the fluid domain and its location inside the GT is shown and compared with the CAD model.

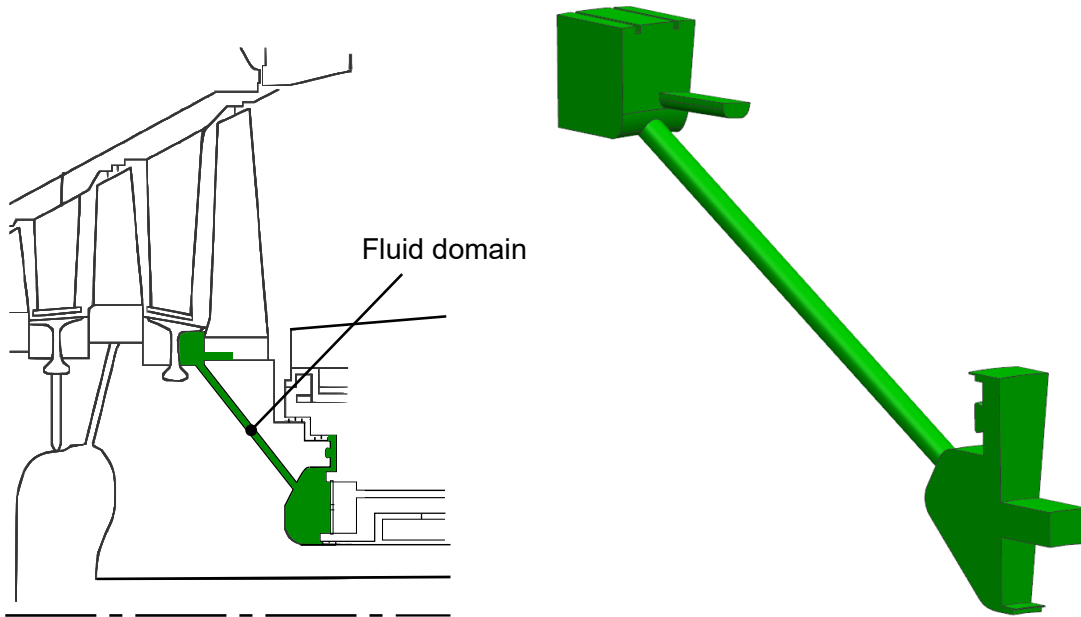


*Fig. 3.1: Sketch of the fluid domain and its position inside the GT (left); CAD model of the fluid domain (right).*

The fluid domain did not include the labyrinth seals since they were not relevant for the aforementioned analysis goal and would have added unnecessary complexity to the model. However, the flow through the seals must be modelled since it produces a radial through-flow in the SR cavity, which influences the swirl distribution in the cavity itself, as seen in chapter 1.6. In addition, at the location of the labyrinth seals, the fluid domain was elongated in the axial direction in order to reduce the risk of recirculation, as sketched in Fig. 3.2.

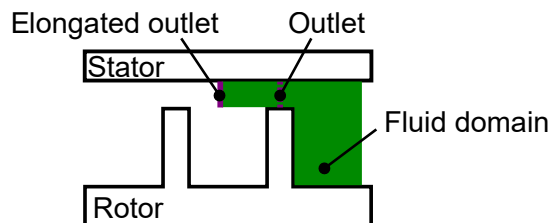


*Fig. 3.2: Sketch of the fluid domain at the labyrinth seal.*

The inlet section of the domain was also elongated in the axial direction by a factor of  $5h$ , where  $h$  is the height of the channel, in order to obtain a fully developed flow in the proximity of the SR cavity.

In Fig. 3.3, the fluid domain at the RHS cavity can be observed. In the RHS cavity, the ribs that support the rotor heat shield were included since they have a direct impact on the flow field in this region. Additionally, the channel at blade four firtree was included, as it represents the main outlet of the system.

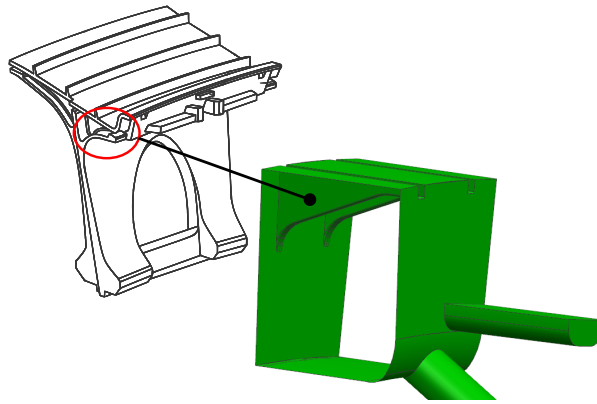


*Fig. 3.3: Detail of the CAD model at the RHS cavity.*

The RB inlet represents a key feature of the alternative feed system design. Hence, a more detailed description of this feature will be presented in the next section.

### 3.1.1 Rotor bore inlet design

The design of the receiver bores represents a critical aspect of the project and therefore, it requires particular attention.

In section 1.5, for a receiver with sharp edges and a relative velocity  $w$  inclined with a certain angle  $\beta$  with respect to the axis of the receiver, it has been shown that the inlet area is subject to a high risk of detachment and recirculation. This would lead to unacceptable losses. This effect is clearly visible in Fig. 3.4 (a), where the streamlines show a visible zone of recirculation at the inlet of the receiver.

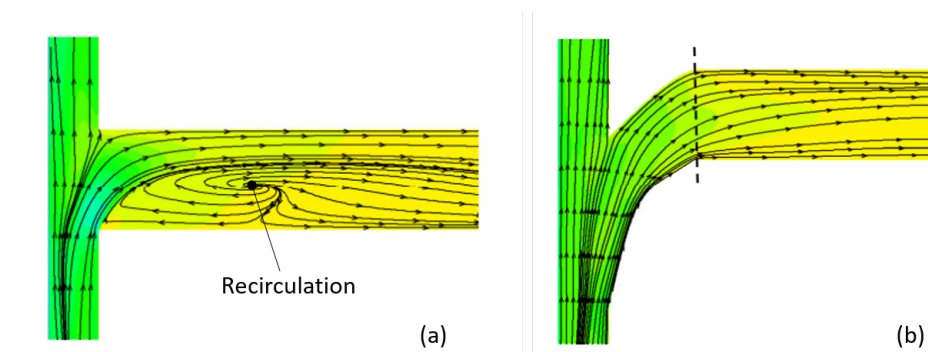


*Fig. 3.4: Streamlines at the inlet of a rotating bore with sharp edges (a) and with fillet edges (b) [21].*

A possible solution is shown in Fig. 3.4 (b). Instead of sharp edges, the inlet of the receiver bore is shaped with a fillet edge oriented in the direction of rotation of the rotor. The introduction of a fillet edge allows for a smoother transition from the cavity to the cooling bores and improves the flow conditions at the bore inlet. The recirculation area is reduced and thus, the effective flow cross section in the cooling bore inlet is increased. This limits the peak-velocities to lower values and significantly reduces the pressure losses [22]. For a given mass flow and a given diameter, a high number of bores is required to minimise the velocity in order to reduce the friction losses. However, by increasing the number of bores, the wall

thickness between neighbouring bores is reduced. This distance limits the rotor lifetime at the inlet of the bores. In order to keep the minimum wall thickness as high as possible, the edge fillet is only applied on one side of the bore in the direction of rotation. A simplified cross-section of the inlet of the RB on the  $x - \theta$  plane is shown in Fig. 3.5. Here,  $x$  is the bore axis and  $\theta$  is the circumferential direction.

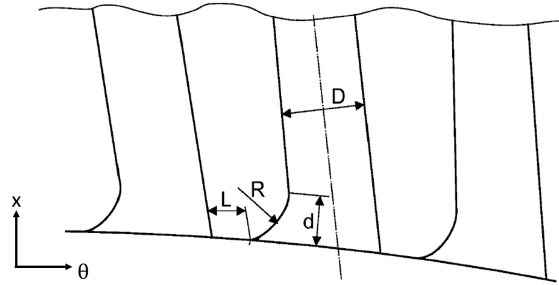


Fig. 3.5: RB inlet cross-section on the  $x - \theta$  plane [22].

Fig. 3.6 shows a cross-section on the  $r - \theta$  plane, where  $r$  is the radial direction.

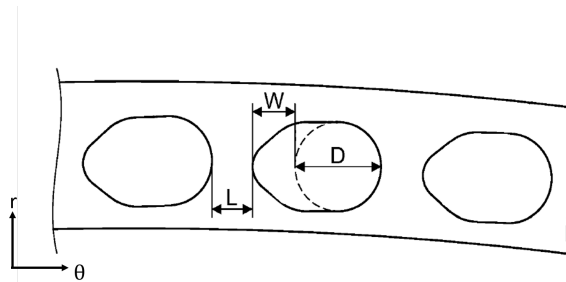


Fig. 3.6: RB inlet cross-section on the  $r - \theta$  plane [22].

The main design constraint that must be fulfilled regards the distance between two neighbouring bores. Defining  $D$  as the diameter of the bores,  $L$  as the distance between the edges of two contiguous bores and  $W$  as the length of the asymmetric fillet projected on the  $r - \theta$  plane (see Fig. 3.6), MI fixed a minimum ratio  $\frac{(L+W)}{D}$  that must be fulfilled. The number of bores was fixed equal to the number of blades. This was done to locate the outlet symmetrically under the blades firtees. Moreover, the firtee is subjected to high mechanical stresses induced by the centrifugal forces acting on the blades. Therefore, the exact position of the outlet of the bore in the RHS cavity was defined by the department of MI to not compromise the stability of the firtee. The curvature radius of the fillet at the inlet  $R$  (see Fig. 3.5) was computed assuming the same ratio  $R/D$  of the RB that is currently present in the cooling feed system for blade three. Additionally, the radial position of the inlet of the cooling bores was fixed in order to avoid the modification of the radial position of the balancing pin holes. Ultimately, the diameter and the number of RB were fixed according to the assumptions and constraints mentioned above.

In Fig. 3.7, the final design for the inlet of the receiver bore is shown.



*Fig. 3.7: Front view (left) and  $x - \theta$  view (right) of the RB fillet inlet.*

## 3.2 Mesh generation

The mesh was generated using CENTAUR, a software that allows for the creation of hybrid grids in complex geometries. The hybrid mesh approach combines prismatic or hexahedral elements, typically used in block-structured grids, with tetrahedral elements, which are used for unstructured grids.

Triangles on the boundary surface are used as a starting point to create layers of prismatic elements in the near-wall regions. The structured nature of the prismatic elements in the direction normal to the wall exploits the advantages of traditional structured grid approaches and allows for a better capture of the boundary layer in proximity of the walls. Furthermore, prismatic grids offer good orthogonality and clustering capabilities. Tetrahedral elements are used to fill the rest of the domain allowing single-block generation even for extremely complex geometries. Additionally, the tetrahedral elements are well suited for grid refinement. Pyramids are used in some locations to allow for the transition between the prisms or hexahedra and the tetrahedra. [35]

The CAD model of the fluid domain was first exported into an IGES (Initial Graphics Exchange Specification) file and then imported to CENTAUR. During the process, it was necessary to repair alterations such as gaps, overlaps and discontinuities. This was done using GeoRepair, a tool included within CENTAUR. Moreover, CENTAUR allows the user to specify the size of the tetrahedra elements, the mesh clustering and the thickness of the first layer of prismatic elements in regions of interest such as the RB, the SR cavity and the surfaces in proximity of the labyrinth seals. The first layer thickness was chosen accordingly to the desired  $y^+$  at the wall, which depends on the near-wall treatment that is intended to be used.

### 3.3 Computational set-up

In this section, a brief description of the case set-up used in the CFD analysis will be presented. The CFD simulations were performed using the commercial software ANSYS Fluent, while for the post-processing the software ParaView was employed.

#### 3.3.1 Frame of reference

ANSYS Fluent solves by default the equation of fluid flow and heat transfer in a stationary reference frame. However, in problems that involve rotating parts such as rotating blades or walls (as in the case of this study), it is advantageous to solve the governing equation in a non-inertial frame of reference.

This results from the fact that rotating parts make the problem unsteady, if considered in the inertial frame. On the contrary, a rotating frame of reference allows to model the flow around rotating parts as a steady-state problem with respect to the moving frame. This is accomplished by incorporating additional accelerations terms in the solving equation that arise from the transformation from the inertial to the non-inertial frame of reference. These additional terms are the Coriolis acceleration and the centripetal acceleration. Therefore, for this study, the Single Rotating Reference Frame (SRF) was chosen.

Moreover, in ANSYS Fluent, the momentum equation can be formulated in two different ways:

- using the relative velocities as dependent variables,
- using the absolute velocities as dependent variables.

The first option is known as the Relative Velocity Formulation. This formulation is advantageous when the relative velocities of the flow field are on average smaller than the absolute ones. In this way, the numerical diffusion is reduced and the solution is more accurate. [36]

Therefore, for this study, the Relative Velocity Formulation was chosen. The equations implemented in the Relative Velocity Formulation are detailed in the Appendix A.2.

#### 3.3.2 Turbulence model

GT internal flows are typically turbulent and dominated by rotation, which results in complex shear layers with a highly non-isotropic turbulent field. As a result, turbulence plays a significant role in SAF [20]. In order to model the effects of turbulence, a RANS approach was chosen. The turbulent flow governing equations are the Reynolds-averaged Navier-Stokes (RANS) equations. The solvable RANS equations obtained using the Boussinesq hypothesis in index notation form are:

$$\frac{\partial U_i}{\partial x_i} = 0 \quad (3.1)$$

$$\frac{\partial U_i U_j}{\partial x_j} = -\frac{1}{\rho} \left( \frac{\partial p}{\partial x_i} + \frac{2}{3} \rho \frac{\partial k}{\partial x_i} \right) + \frac{\partial}{\partial x_j} \left[ \frac{1}{\rho} (\mu + \mu_t) \frac{\partial U_i}{\partial x_j} \right], \quad (3.2)$$

where  $U_i$  is the generic component of the mean velocity vector.

Additional equations are needed to close the system. These equations are provided by the turbulence models and the gas state equation.

In this study, the *Realizable*  $k-\epsilon$  turbulence model was used, while the air is treated as an ideal gas. In the Appendix A.3, a detailed description of the turbulent model is presented.

### 3.3.3 Near-wall treatment

In order to considerably reduce the number of cells and thus, the computational time, a near-wall treatment based on the high-Reynolds approach was used. The high-Reynolds approach consists of the use of wall functions at the wall to model the inner part of the boundary layer. Wall functions are empirical equations used to satisfy the physics of the flow in the near-wall region. With standard wall functions, the first cell center should be placed in the log-law region, where  $30 < y^+ < 300$  (see Fig. 3.8), to ensure a better accuracy of the result.

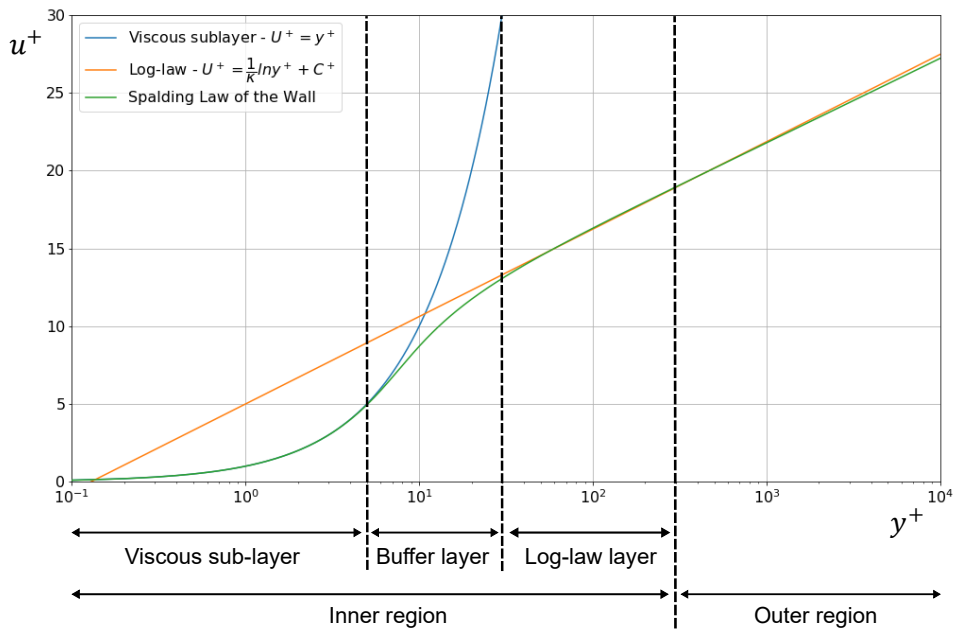


Fig. 3.8: Non-dimensional velocity profile at the wall.

The high-Reynolds approach was judged as the best compromise between accuracy and computational time.

### 3.3.4 Solver

The SIMPLE scheme was chosen as the pressure-velocity coupling scheme. For the spatial discretisation of the thermodynamic quantities, a second-order upwind scheme was chosen.

## 3.4 Boundary conditions

Fig. 3.9 summarises the boundary conditions. Four different classes of boundary conditions were implemented in the case object of this study:

1. **Inlet:** the fluid domain is characterised by one inlet section, located in the SR cavity. At the inlet surface, the CA mass flow and the total absolute temperature derived from the preliminary assessment were fixed.

2. **Outlet:** the fluid domain is characterised by three outlet sections, respectively located at the blade's firtree and at the labyrinth seals in the SR cavity.

At the blade's firtree, the target static pressure was used as the outlet boundary condition.

For the two remaining outlet surfaces, the option "target mass flow rate" was chosen since the labyrinth seals were not modelled. This option allows to set a mass flow rate and let the solver set the outlet static pressure in order to meet the desired mass flow rate, avoiding undesired and non-physical behaviour. The desired mass flow was derived from the preliminary assessment.

3. **Solid boundaries:** viscosity plays a key role in SAS flows. Therefore, the no-slip condition was applied to the walls.

Nevertheless, two different types of walls are present in the study case:

- The bearing case walls (in gray, in Fig. 3.9) which form part of the SR cavity are statoric walls and thus, must be modelled as a stationary wall. For these surfaces, the no-slip condition refers to the absolute velocity.
- The remaining walls (in orange, in Fig. 3.9) rotate around the axis of rotation of the GT and therefore must be modelled as rotoric walls with a rotational speed equal to the rotational speed of the GT. In this case, the no-slip condition refers to the relative velocity.

The walls were treated as adiabatic.

4. **Periodicity:** the lateral surfaces at the SR cavity and at the RHS cavity were modelled as rotational periodic surfaces since the assumption of rotational periodicity was made to simplify the fluid domain.

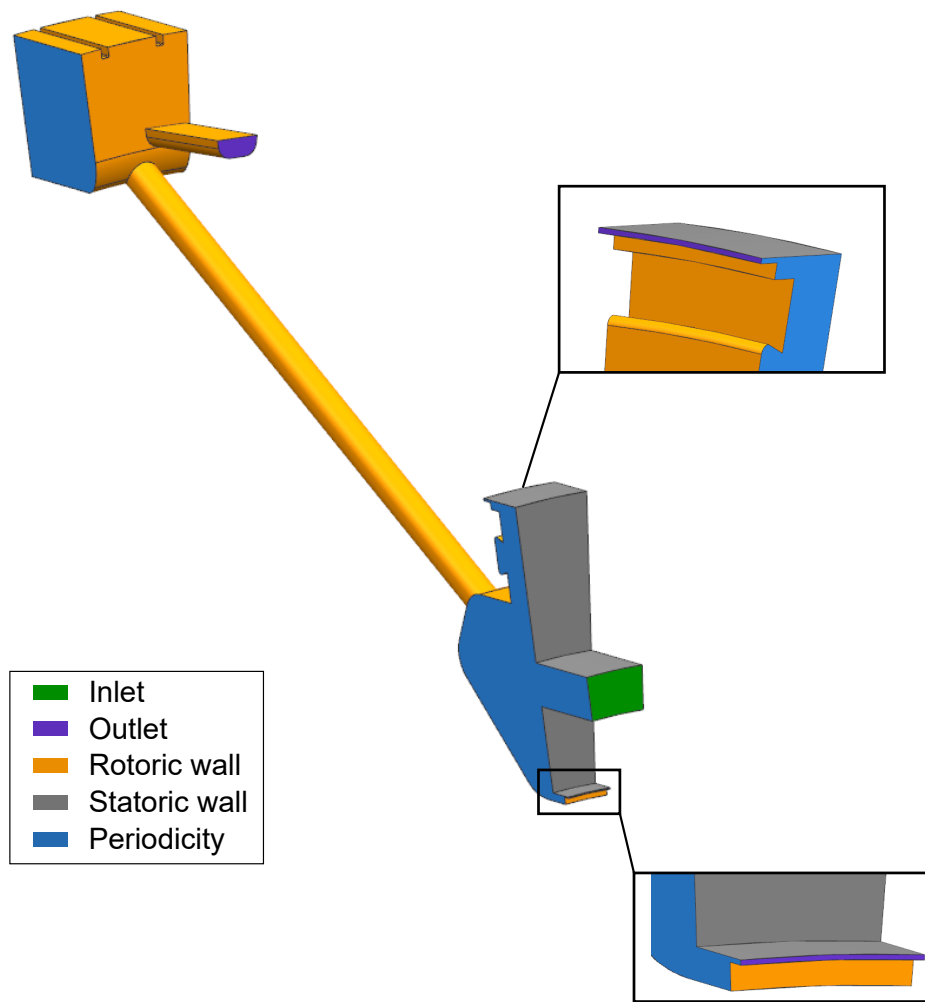


*Fig. 3.9: Boundary conditions.*

### 3.5 Mesh sensitivity study

The goal of the grid sensitivity study was to find a mesh characterised by a low number of cells. In this way, the computational time is reduced. Nevertheless, the grid must give reliable results in terms of integral quantities and a correct prediction of the flow field in the computational domain. Five different grids were generated and compared in order to find an appropriate mesh, which is summarised in the following table.

*Tab. 3.1: Number of cells for each grid.*

	<b>Number of cells</b>
i - Coarse	0.2 M
ii	1.9 M
iii	2.8 M
iv	4.9 M
v - Fine	23 M

In Fig 3.10, the coarse mesh is shown and compared to the fine mesh in Fig. 3.11 .

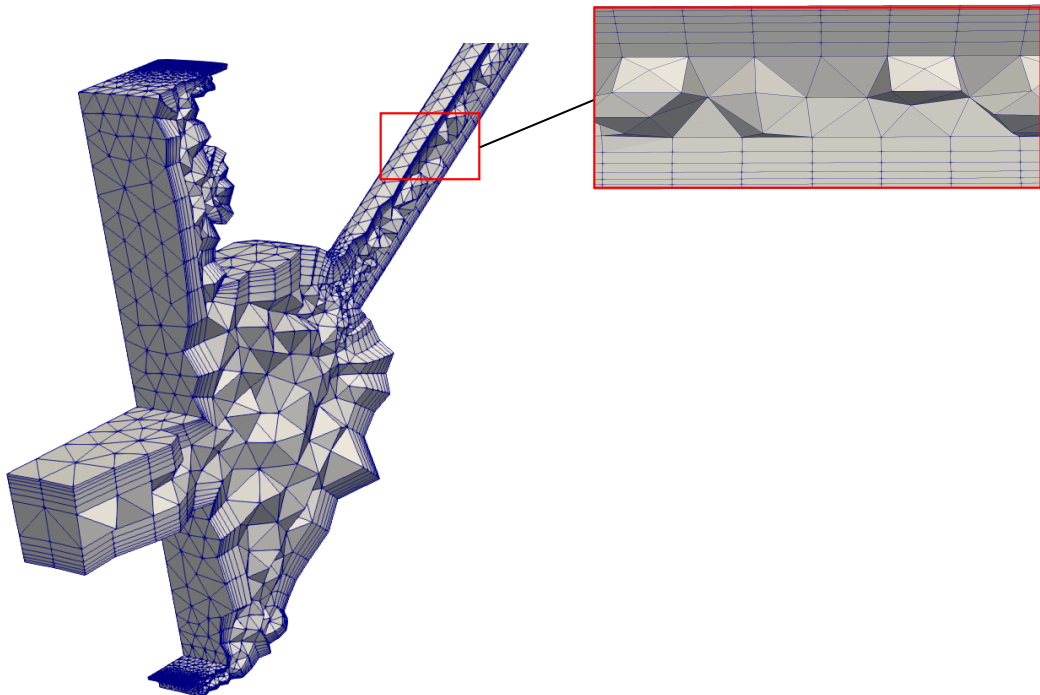


*Fig. 3.10: Coarse mesh.*

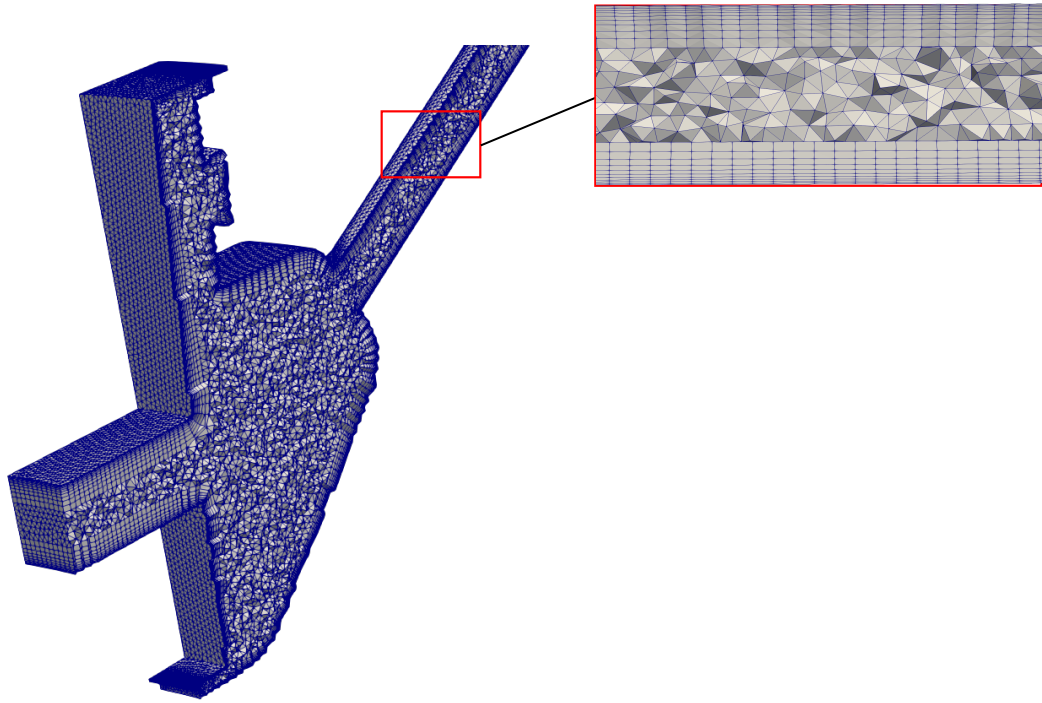
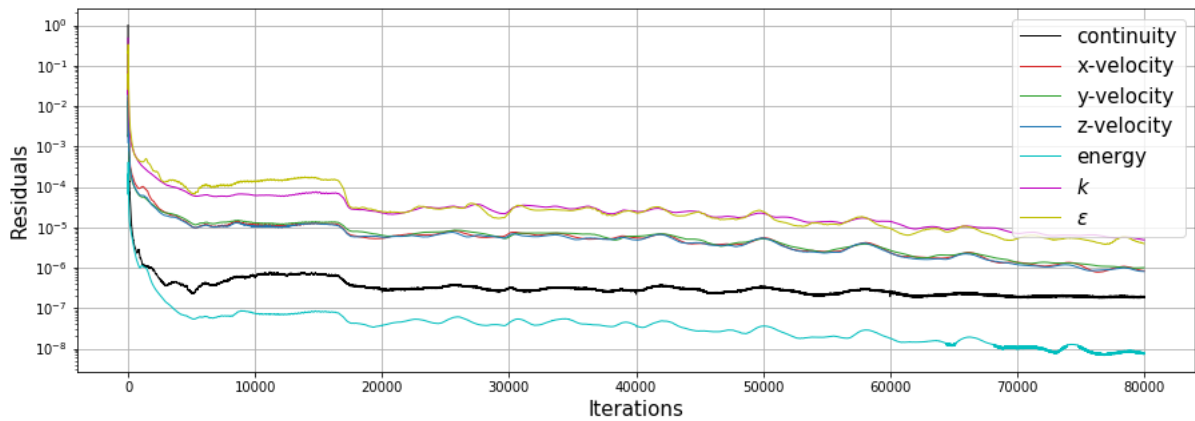


*Fig. 3.11: Fine mesh.*

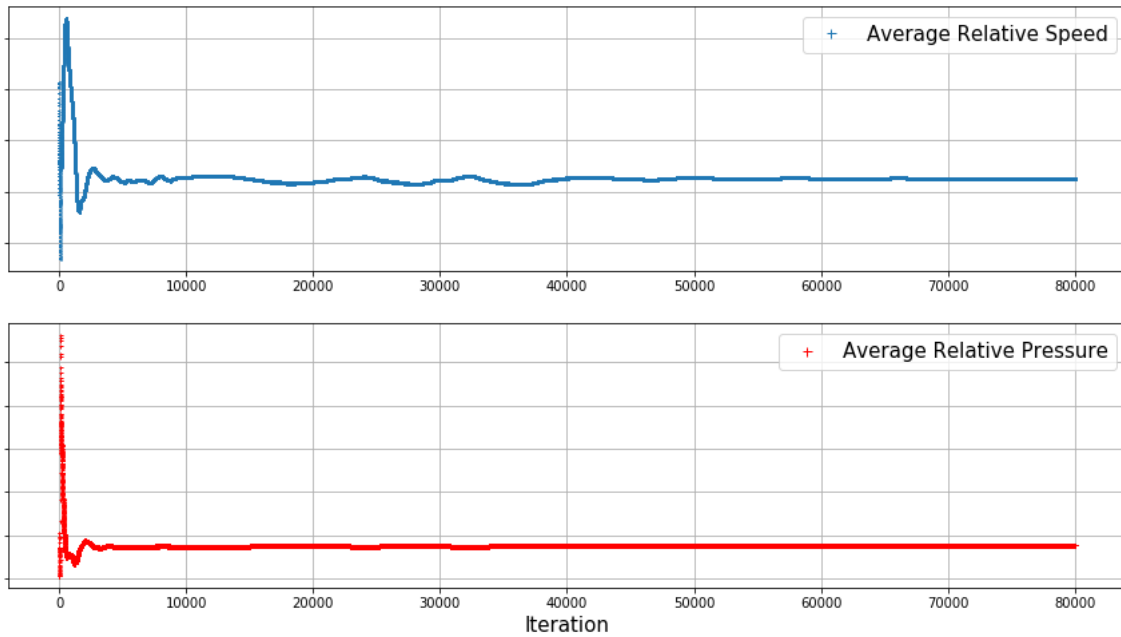
To ensure the convergence of the simulation, the residuals, values of relative velocity and pressure averaged over a cross-sectional plane at the RB were monitored.

Fig. 3.12 shows the residuals plotted against the iterations for a fine mesh: after approximately 60000 iterations, the residuals show a value below  $10^{-5}$  and the solution can be considered as converged.

This is confirmed by Fig. 3.13, in which the average relative velocity (on top) and the average static pressure (bottom) are plotted against the number of iterations for the same mesh. After 60000 iterations, the values are constant and the solution is therefore converged.



*Fig. 3.12: Residuals.*



*Fig. 3.13: RB average relative speed (top) and average relative pressure (bottom).*

In addition to the monitoring of the convergence of the aforementioned parameters, the  $y^+$  distribution must be controlled to ensure that the value is coherent with the near-wall treatment chosen for this study. In Fig. 3.14, the  $y^+$  distribution over the rotoric walls for the fine mesh is shown as an example.

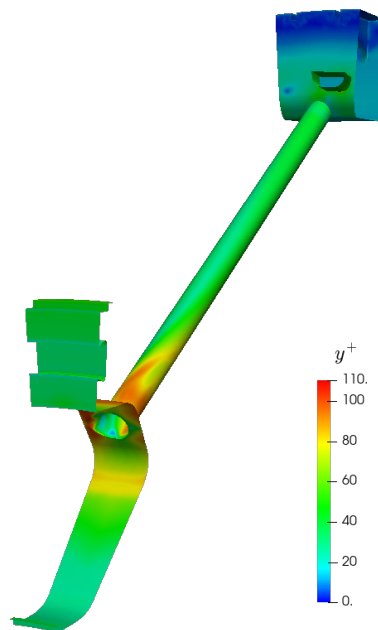


*Fig. 3.14: Contour of  $y^+$  over the rotoric walls.*

To compare the results of the five different grids, the velocity profiles in the RB and in the SR cavity were monitored. The velocity profiles are shown in Fig. 3.15, 3.16 and 3.17. It can be observed that the profiles of grid (iv) and (v) are independent of the mesh size. For that reason, mesh (iv) was chosen. Additionally, global parameters such as absolute total pressure at the inlet of the domain and total relative temperature at the blade's firtree show a relative difference below 1% for all the grids.

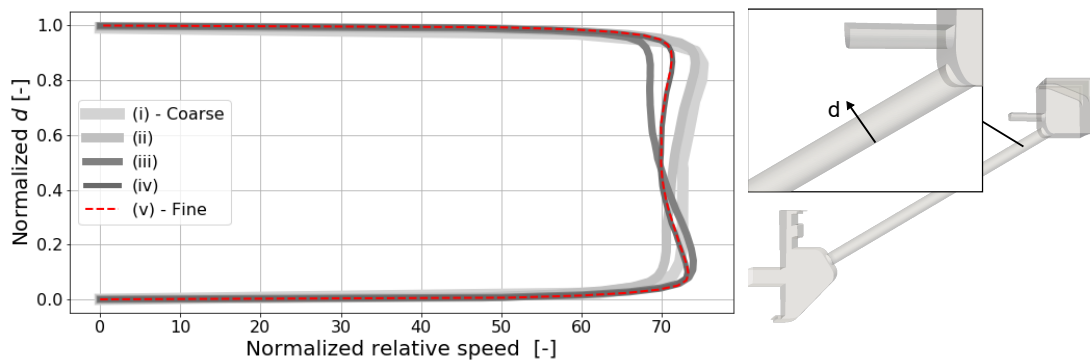


Fig. 3.15: Profiles of the relative velocity in the RB for the five different grids.

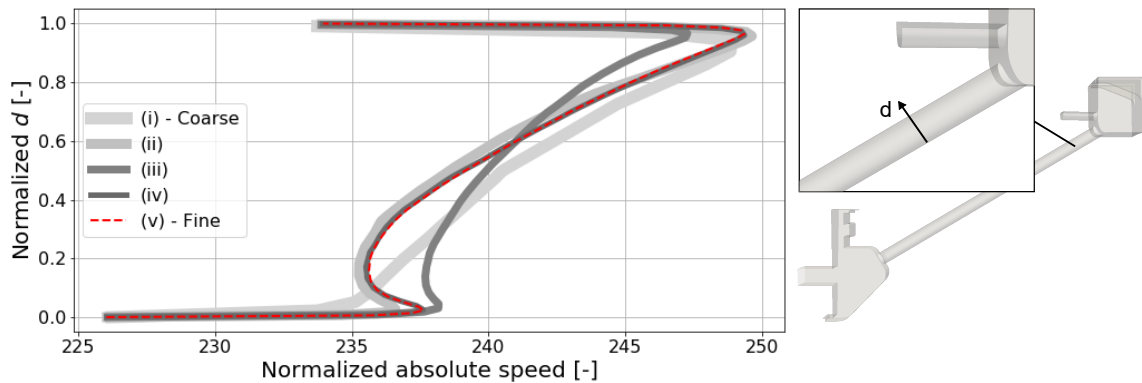
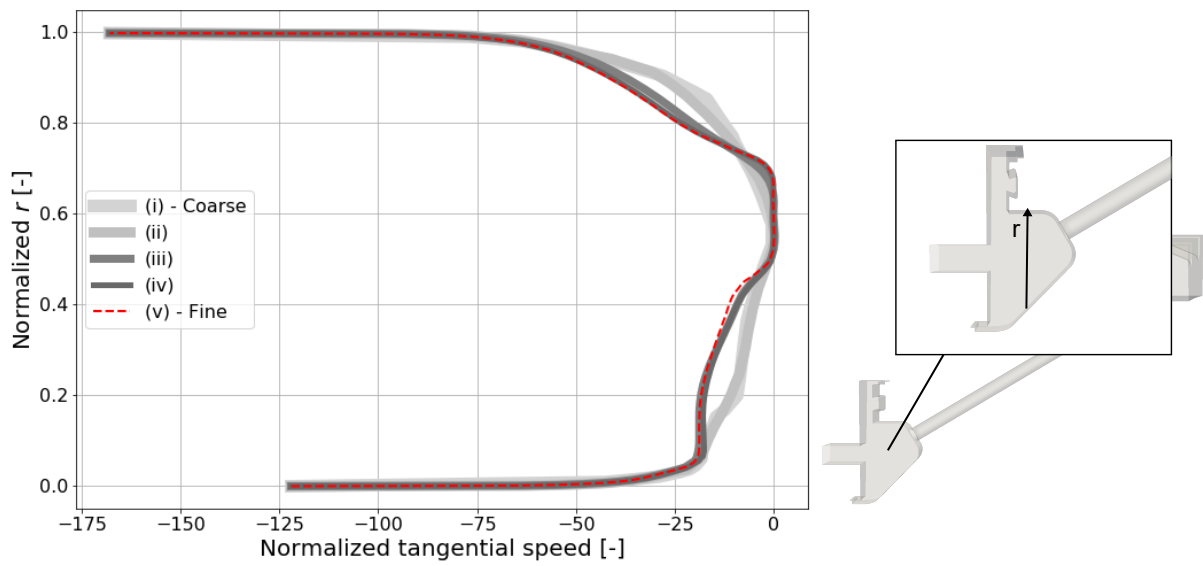


Fig. 3.16: Profiles of the absolute velocity in the RB for the five different grids.



*Fig. 3.17: Profiles of the tangential velocity in the SR cavity for the five different grids.*

## 4 Results and discussion

The reliability of a 1-D flow network depends on the empirical correlations implemented and on the validity of the assumptions made to build the network. Consequently, when a 1-D flow network of a new feed system is assembled, a re-calibration phase improves the quality of the correlations and the fidelity of the results.

In this chapter, the results of the CFD analysis of the concept selected for the alternative feed system will be presented. Moreover, the results obtained from the CFD analysis will be compared with the 1-D prediction and used to re-calibrate the 1-D flow network. This will be done for the base-load case and the part-load case.

### 4.1 Degrees of freedom of the 1-D flow network

In section 2.4.2, the assembly of the internal line of the 1-D flow network was presented. The variables, which represent the degrees of freedom of the flow network, are the following:

1. total pressure of the plenum at the inlet of the internal line,
2. tangential velocity set by the "swirl-generator" element in the SR cavity,
3. vortex exponent of the whirl connection in the SR cavity,
4. discharge coefficient at the inlet of the RB,
5. friction coefficient at the outlet of the RB,
6. discharge coefficient from the RHS cavity to the firtree.

In order to compare the results of the 1-D flow network with the results of the CFD analysis, the pressure and temperature at following different nodes in the flow network are considered:

1. static pressure in the SR cavity,
2. relative total pressure and relative total temperature in the SR cavity,
3. relative total pressure and relative total temperature at the control node located downstream to the inlet of the RB,
4. relative total pressure and relative total temperature at the outlet of the RB,
5. relative total pressure and relative total temperature in the RHS cavity (at the radius of the the RB outlet),
6. relative total pressure and relative total temperature in the RHS cavity (at the radius of the blade's firtree),
7. relative total pressure and relative total temperature at the blade's firtree.

The static pressure in the SR cavity can be assumed equal to the total absolute pressure since the absolute dynamic head is expected to be negligible due to the absence of the PSN.

The same quantities must be obtained from the CFD analysis. Therefore, a series of control surfaces at the same radius as the respective control nodes of the flow network are used. The values of the thermodynamic quantities for the comparison were obtained as average quantities on the control surfaces. Fig. 4.1 shows the main control surfaces considered for the post-processing of the CFD data.

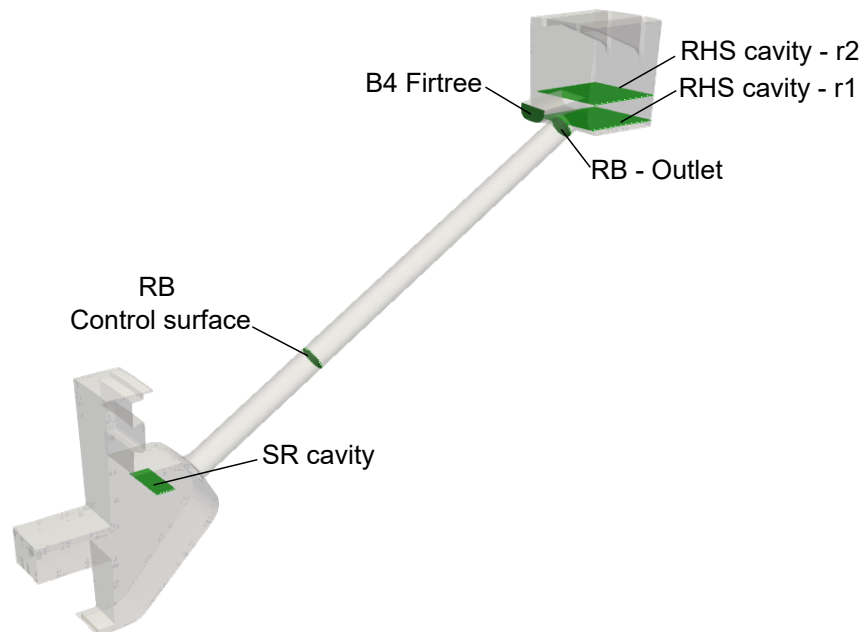


*Fig. 4.1: Main control surfaces considered for the post-processing of the CFD data.*

In addition to the above mentioned surfaces, auxiliary surfaces and planes were considered in order to develop a better understanding of the flow field.

## 4.2 Base-load case

Fig. 4.2 compares the values of total relative pressure predicted by the 1-D flow network with the results obtained from the CFD analysis at different locations in the flow system. In addition to the total relative pressure, the static pressure at SR cavity is shown.

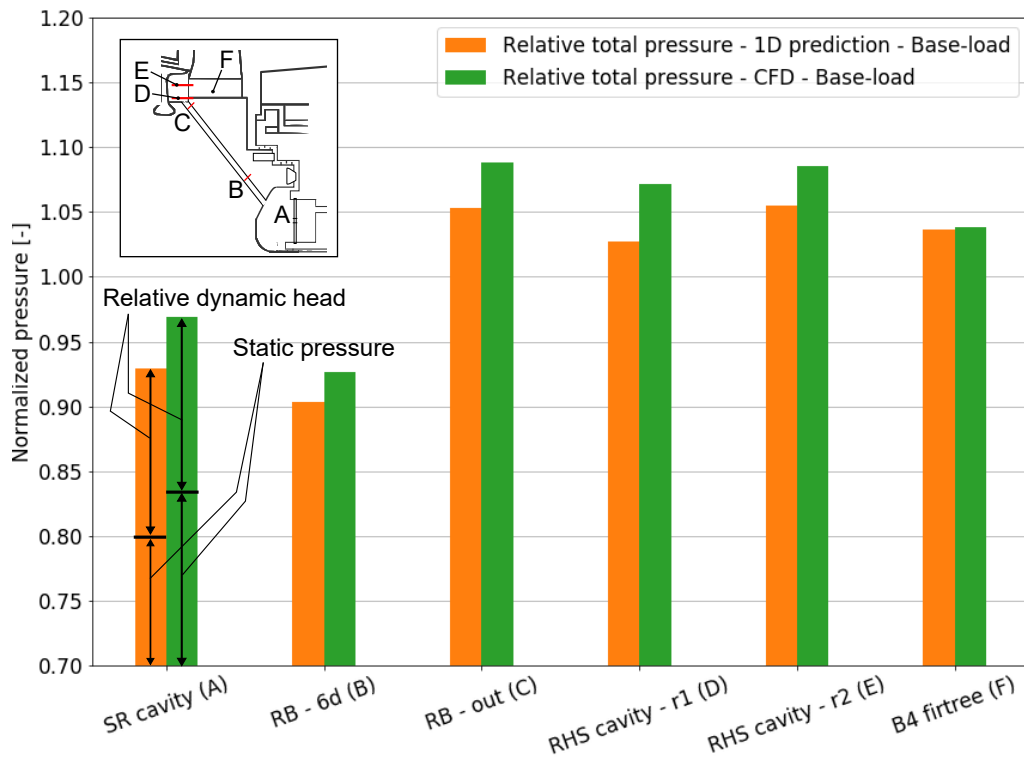


Fig. 4.2: Comparison of total relative and static pressure for the 1-D prediction and the CFD analysis at base-load.

Fig. 4.3 compares the distribution of the total relative temperature predicted by the 1-D flow network with the results obtained from the CFD analysis.

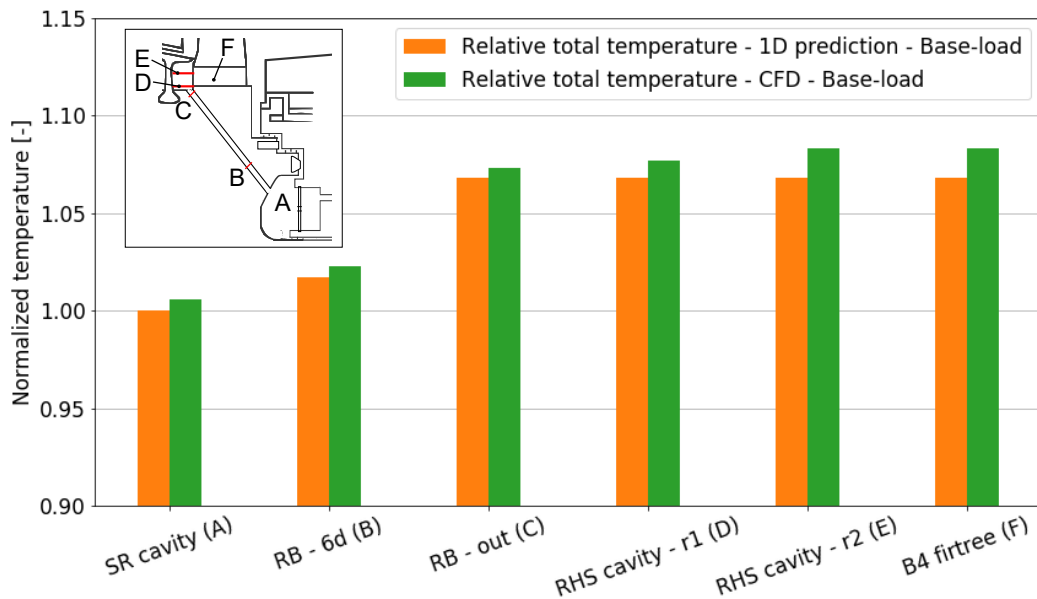


Fig. 4.3: Comparison of total relative temperature for the 1-D prediction and the CFD analysis at base-load.

In the following, the results of the CFD analysis will be shown and compared to the

1-D prediction.

#### 4.2.1 Stator-rotor cavity

The predicted value of the static pressure in the SR cavity is lower than the value obtained from the CFD analysis. As mentioned above, the static pressure in the SR cavity is directly proportional to the pressure required by the external compressor. Therefore, a detailed analysis of the losses and their sources is necessary in order to mitigate them.

Fig. 4.4 shows the contour plot of the tangential velocity in the SR cavity. The cavity can be divided into three zones characterised by different values of tangential velocity. The area of the cavity in front of the receiver bore (zone 1) is characterised by a core of fluid with a low swirl. This results from the fact that a high mass flow with nearly zero swirl goes from the inlet of the cavity to the inlet of the receiver. Additionally, Fig. 4.4 confirms the validity of the assumption of constant  $v_\theta$  from the inlet of the domain to the inlet of the receiver. This assumption is also valid for the lowermost part of the cavity (zone 2), even though in this area the value of the tangential velocity is higher than the value at the inlet of the receiver. For the upper side of the cavity (zone 3), the flow field is made complex by the presence of the groove used to place the balancing segments. Therefore, the assumption of constant tangential velocity is not valid at this location and a value of tangential speed must be imposed in order to match the static pressure in front of the labyrinth seal. However, for a more precise evaluation of the flow field in this area, the presence of the discontinuous balancing segments must be considered.

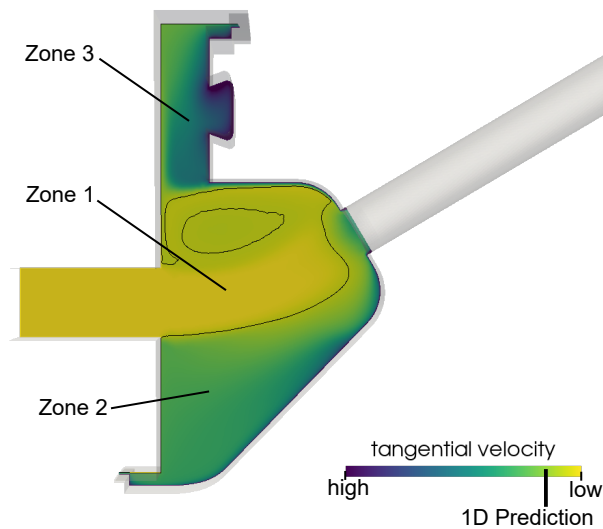


Fig. 4.4: Tangential velocity in the SR cavity.

The magnitude of the tangential velocity in the core of the flow in the upper part of the cavity is lower than the value obtained by the 1-D momentum balance. Therefore, the value imposed by the "swirl generator" connection must be corrected. The predicted total relative temperature in the SR cavity is lower than the temperature given by the CFD evaluation. A higher temperature is probably caused by the heat

produced by the friction in the cavity, which was not included in the 1-D flow network used for prediction. Therefore, the total temperature at the plenum at the inlet of the internal line was increased in order to match the values of the flow network with the results of the CFD analysis.

#### 4.2.2 Rotor bore inlet

The RB inlet is a crucial location since high losses are expected. The losses at the inlet of the RB can be evaluated by defining a discharge coefficient:

$$C_d = \frac{1}{\sqrt{\zeta + 1}}, \quad (4.1)$$

where the friction coefficient  $\zeta$  can be computed as:

$$\zeta = \frac{p_{t,rel1} - p_{t,rel2}}{\frac{1}{2}\rho_2 w_2^2}. \quad (4.2)$$

In eq. 4.2,  $p_{t,rel1}$  is the relative pressure evaluated inside the SR cavity, while  $p_{t,rel2}$ ,  $\rho_2$  and  $w_2$  are respectively the relative total pressure, density and relative speed evaluated at a section, which is usually located two diameters away from the inlet [23]. However, in this study, the losses extend for more than two diameters away from the inlet. This is shown in Fig. 4.5 using the velocity vector field in a cross-sectional plane located in the middle of the RB. Velocity vectors are scaled using the logarithmic value of the relative velocity magnitude for visualisation purpose.

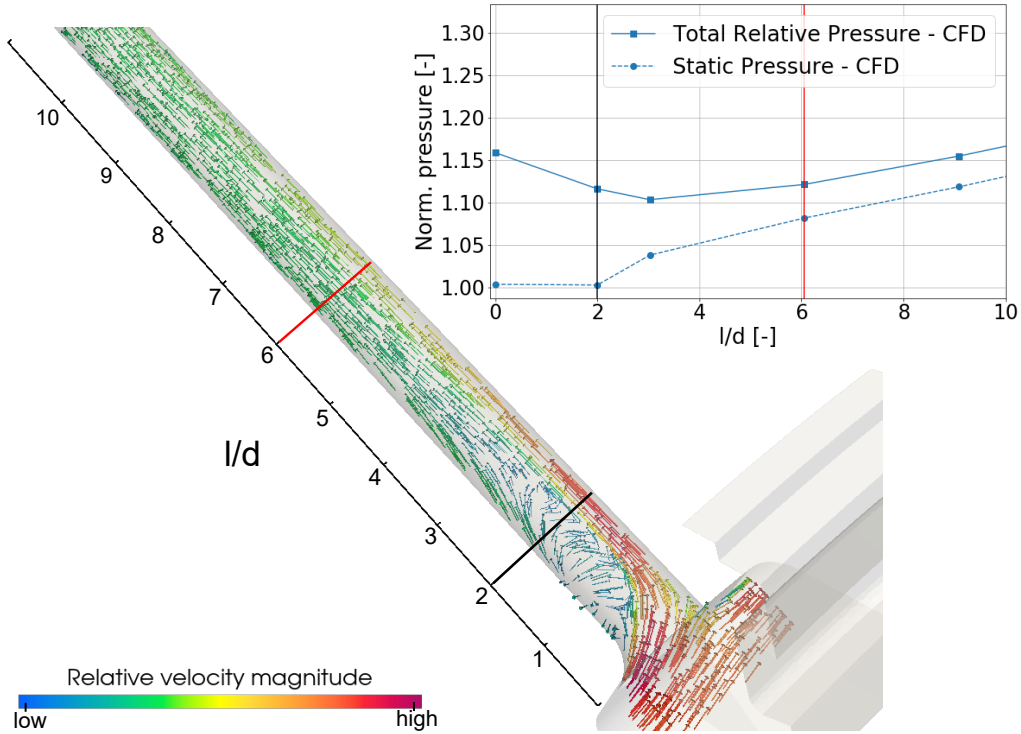


Fig. 4.5: Vector flow field and pressure distribution at the inlet of the RB.

This is confirmed by the diagram shown in Fig. 4.5, where the total relative pressure

and static pressure are plotted against the axial distance from the inlet of the bore non-dimensionalised using the diameter. It can be noticed that the effect of the recirculating flow on the total relative head extends up to a distance of six diameters from the inlet. Therefore, in order to evaluate the discharge coefficient, section 2 must be moved at a location that is at least six diameters away from the inlet of the receiver bore. Additionally, for the evaluation of the thermodynamic quantities, the rise of static pressure due to the pumping effect inside the bore must be taken into account.

Fig. 4.6 shows the correlation, property of Ansaldo Energia [23], used to predict the discharge coefficient  $C_d$  at the inlet of the bore as a function of the angle of attack  $\beta$ . The correlation is based on the CFD results of the RB located on the disk three that is characterised by a similar design. In the same plot, the predicted value and the value resulted from the CFD analysis are shown. The actual discharge coefficient is lower than expected but aligns with the prediction.

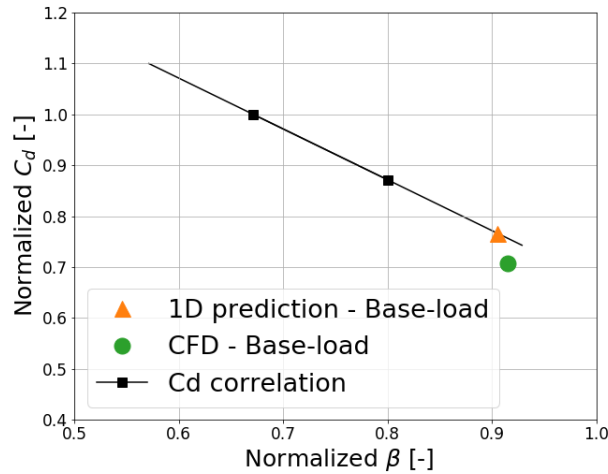


Fig. 4.6: Discharge coefficient for a rotating bore [23].

A low value of the discharge coefficient results from the presence of a re-circulation area, as shown in Fig. 4.6, which is caused by a high angle of attack  $\beta = \text{atan}(\frac{w_\theta}{w_{ax}})$ .

### 4.2.3 Rotor bore friction losses

The losses due to friction in the RB are modelled using a friction coefficient element, as shown in section 2.4.2. In the CFD analysis, the friction coefficient is computed similarly to what was done for the RB inlet. In this case, sections 1 and 2 are respectively the section located six diameters away from the inlet and the section at the outlet of the bore. The friction coefficient obtained by the CFD evaluation is 60% smaller than the the friction coefficient estimated. This can be partly attributed to the fact that the friction losses evaluated in this way do not include the first section of the bore, which are included in the losses at the inlet of the RB instead. Since the friction losses and the losses due to the recirculation at the inlet of the bore cannot be evaluated separately with sufficient precision, it was agreed within the

SAS department to implement the values obtained from the CFD analysis without further correction.

#### 4.2.4 Rotor heat shield cavity

The flow from the RHS cavity to the blade's firtree was modelled with a discharge coefficient (see 2.4.2).

Fig. 4.2 shows that the drop of total relative pressure evaluated at the outer radius in the RHS cavity from the CFD analysis is notably higher than the pressure drop predicted for the 1-D network. This can be seen also in Fig. 4.7, where the discharge coefficient computed from the CFD analysis is compared to the 1-D prediction. The predicted value was obtained from the correlation proposed by [13]: the discharge coefficient is plotted as a function of the pressure ratio across the orifice for different values of the length-to-diameter ratio  $l/d$ .

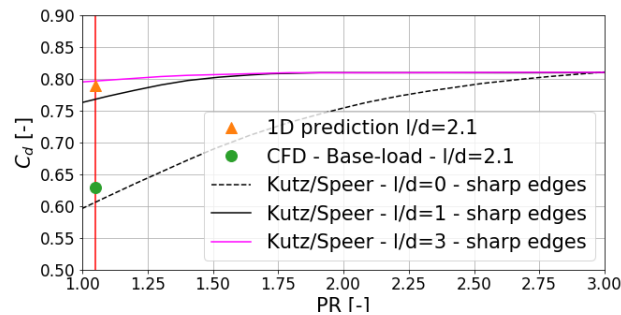


Fig. 4.7: Discharge coefficient for a non-rotating orifice [13].

The higher losses from the RHS cavity to the blade's firtree are due to a higher relative tangential speed in the cavity than expected. Fig. 4.8 (a) shows the vector field of the relative velocity on a horizontal plane at the RHS cavity and blade's firtree. As done for the RB inlet, the velocity vectors in the RHS area were scaled using the logarithmic value of the relative velocity magnitude for a better visualisation.

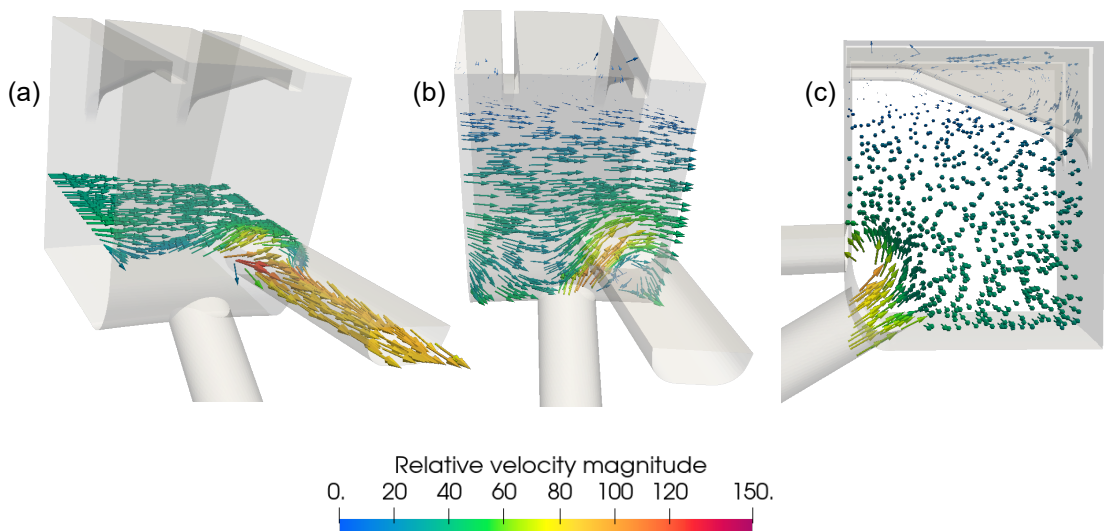


Fig. 4.8: Vector field of relative velocity at the RHS cavity and blade's firtree.

The tangential component of the relative speed in the cavity is enhanced by a vortex that is counter-rotating with respect to the direction of rotation of the GT, as shown in Fig. 4.8 (b). The vortex is caused by a jet that originates at the exit of the bore, as illustrated in Fig. 4.8 (c).

From Fig. 4.8, it can be seen that the relative velocity in the cavity is mainly directed in the tangential direction and must turn to the axial direction to flow into the firtree channel. Therefore, a correlation for a rotating orifice, similar to the one used to predict the discharge coefficient at the RB inlet, must be used. In Fig. 4.9, the discharge coefficient obtained as a result from the CFD evaluation is compared with a correlation proposed by [13]. The correlation gives the values of discharge coefficients for rotating orifices with sharp edges as a function of the angle of attack  $\beta$  for different ratios of length-to-diameter  $l/d$ . It is possible to notice that the discharge coefficient computed is aligned with the proposed correlation with an off-set that could result from 3-D effects that are not considered in the correlations.

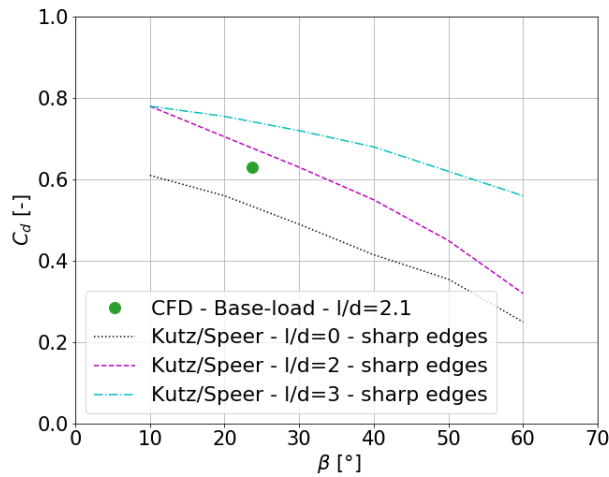


Fig. 4.9: Discharge coefficient for a rotating orifice [13].

The off-set of total relative temperature at the outlet of the domain between the prediction and the CFD results is given by the sum of the off-set of temperature at the SR cavity and the frictional heat produced in the RHS cavity. This last source of heat was not included in the prediction. Therefore, a heat pick-up of  $3\text{ K}$  was added to match the relative total temperature at the blade's firtree.

#### 4.2.5 Re-calibration of the 1-D flow network - Pressure

Once all the variables listed in 4.1 were re-calibrated, it was possible to assemble a new 1-D flow network. In Fig. 4.10, the pressure distribution for the tuned flow network is shown and compared with the prediction and the results from the CFD analysis.

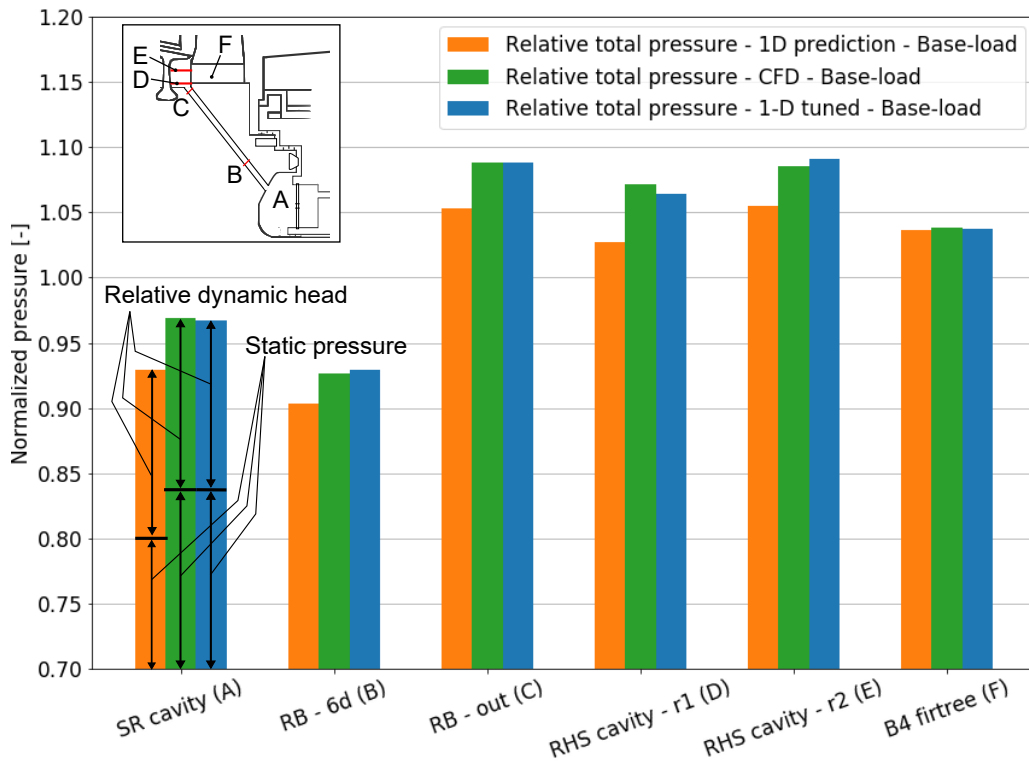


Fig. 4.10: Comparison of total relative and static pressure for the 1-D prediction, CFD analysis and the re-calibrated 1-D flow network at base-load.

It can be noticed that the results of the re-calibrated flow network are well aligned with the results from CFD with a relatively small deviation at the nodes at the RHS cavity. This is mainly due to the fact that the flow in the cavity is highly 3-D and made complex by the presence of the jet.

However, it was decided not to add additional nodes and elements to model the complex flow field in the cavity and to accept a small discrepancy.

#### 4.2.6 Re-calibration of the 1-D flow network - Temperature

In Fig. 4.11 the distribution of the total relative temperature for the tuned flow network is shown and compared with the prediction and the results from the CFD analysis. With the additional heat pick-up at the SR cavity and at the RHS cavity, the new flow network matches well the CFD results.

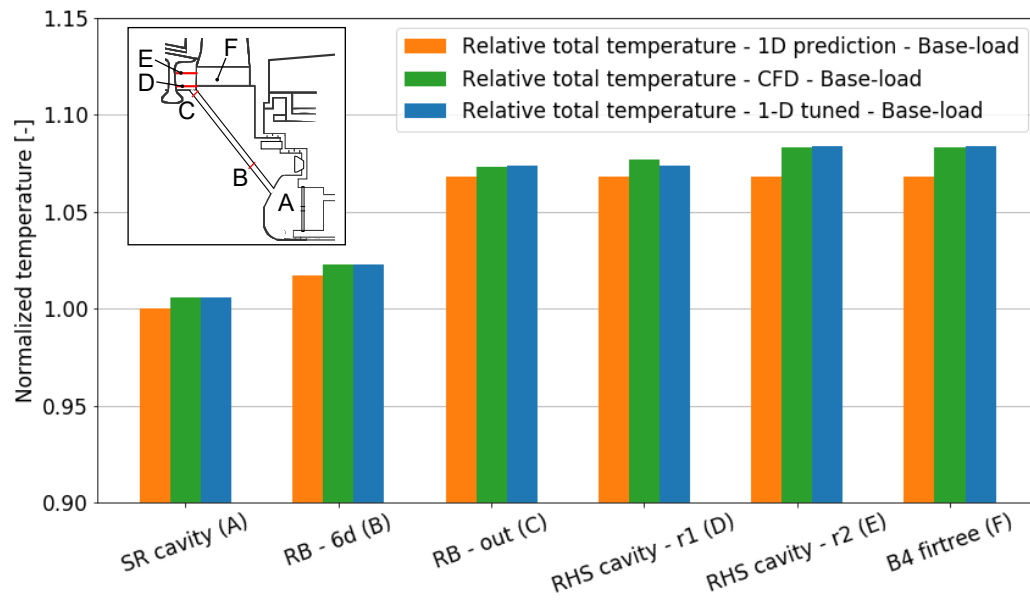


Fig. 4.11: Comparison of total relative temperature for the 1-D prediction, CFD analysis and the re-calibrated 1-D flow network at base-load.

### 4.3 Part-load case

Fig. 4.12 compares the pressure distribution predicted by the 1-D flow network with the results obtained from the CFD analysis.

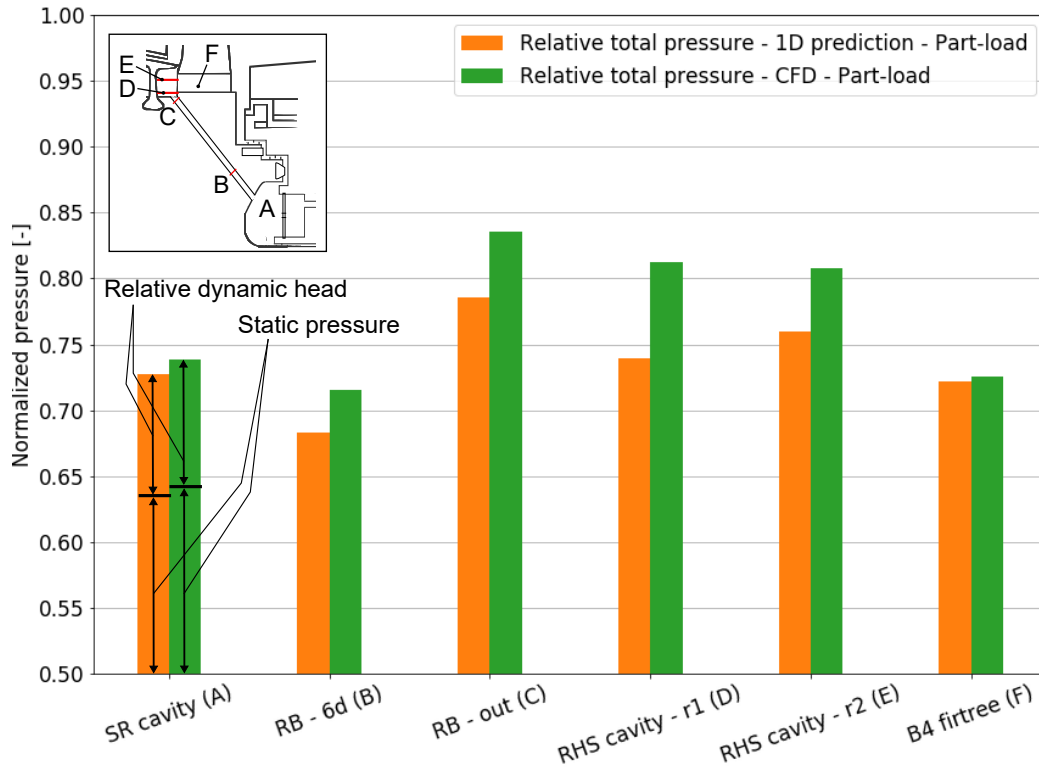


Fig. 4.12: Comparison of total relative and static pressure for the 1-D prediction and the CFD analysis at part-load.

In the following, the results of the 1-D prediction and the results of the CFD analysis will be compared.

#### 4.3.1 Stator-rotor cavity

In Fig. 4.13, the tangential velocity in the SR cavity at part-load (right) is shown and compared to base-load. It can be noticed that the flow field at part-load shows a similar behaviour as at base-load.

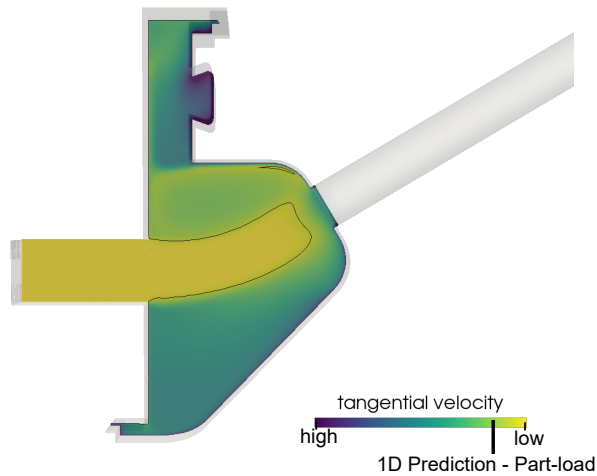


Fig. 4.13: Tangential velocity in the SR cavity at part-load.

However, also for the part-load case, the magnitude tangential velocity computed as a result from the CFD analysis is lower than the predicted value. Additionally, also for the part-load case, the total pressure in the cavity is lower than predicted.

#### 4.3.2 Rotor bore inlet

The losses at the inlet of the bore for the part-load case were expected to be lower than at base-load. The main reason is that although the value of relative tangential velocity in the cavity between the two cases is comparable, the axial speed in the bore for the part-load case is notably higher. The higher axial speed is due to a higher mass flow through the bore and a lower density, as seen in section 2.6. Therefore, the RB inlet at part-load is subjected to a more favorable angle of attack  $\beta$ . This is confirmed by the CFD analysis. In Fig. 4.14, the predicted value and the value obtained from the CFD analysis for the part-load case are shown and compared with the base-load results.

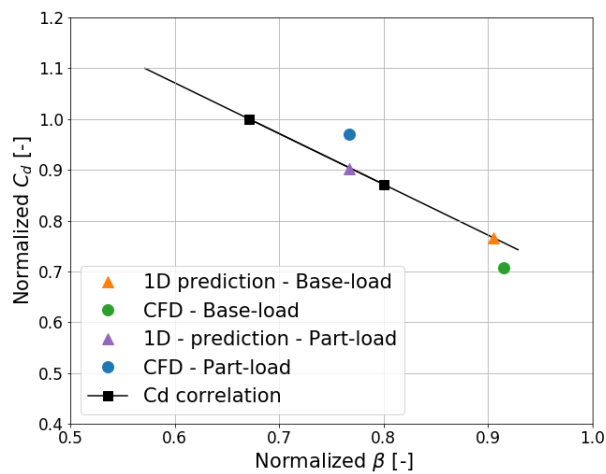


Fig. 4.14: Discharge coefficient for a rotating bore [23].

Moreover, it can be noticed that the discharge coefficient obtained from the CFD analysis is higher than the prediction. This means that for the part-load case, the RB inlet losses were over-predicted.

### 4.3.3 Rotor bore friction losses

For the friction losses at part-load, a consideration similar to the base-load case can be done. The friction coefficient obtained from the CFD analysis was notably lower than the prediction. Therefore, it was corrected to re-calibrate the flow network.

### 4.3.4 Rotor heat shield cavity

As it was seen for the base-load case, also at part-load, the flow field at the SR cavity is highly dominated by the jet from the RB and the losses were under-predicted (see Fig. 4.12). However, the discharge coefficient, which results from the CFD analysis at part-load, is lower than the value obtained at base-load. This can be explained by the different ratios  $\frac{w_\theta}{w_{ax}}$  in the cavity. The jet at part-load results to be stronger than at base-load due a higher axial velocity. Therefore, the vortex in the relative frame is enhanced, leading to a higher tangential velocity  $w_\theta$ . However, as a direct consequence of a higher mass flow and a lower density, the axial component of the relative velocity  $w_{ax}$  in the blade's firtree channel increases more than the relative tangential velocity in the cavity (see Fig.4.15). This results in a lower ratio  $\frac{w_\theta}{w_{ax}}$  in the cavity, which leads to a lower discharge coefficient, as shown in Fig. 4.16.

In Fig. 4.15, the vector field of relative velocity at base-load (a) is compared with the vector field at part-load (b).

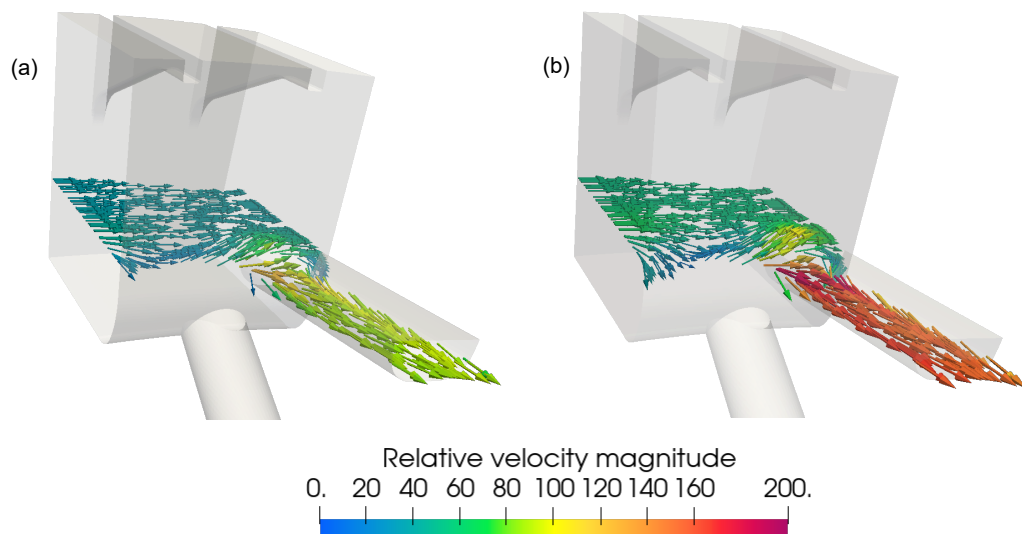


Fig. 4.15: Vector flow field for base-load (a) and for part-load (b) in the RHS cavity.

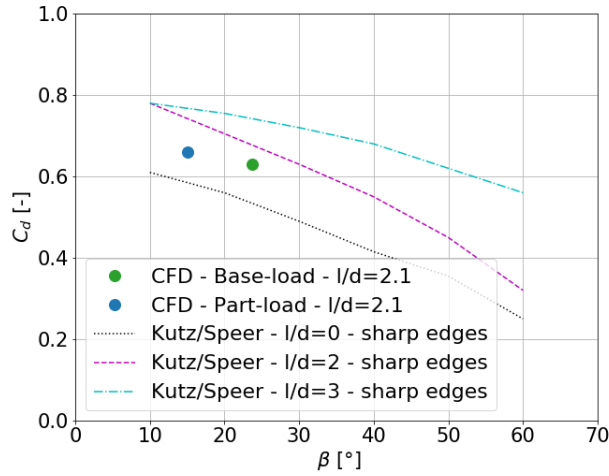


Fig. 4.16: Discharge coefficient for a rotating orifice [13].

#### 4.3.5 Re-calibration of the 1-D flow network - Pressure

As it was done for the base-load case, it was possible to assemble a new 1-D flow network for part-load with the re-calibrated variables. In Fig. 4.17, the pressure distribution for the tuned flow network is shown and compared with the prediction and the results from the CFD analysis.

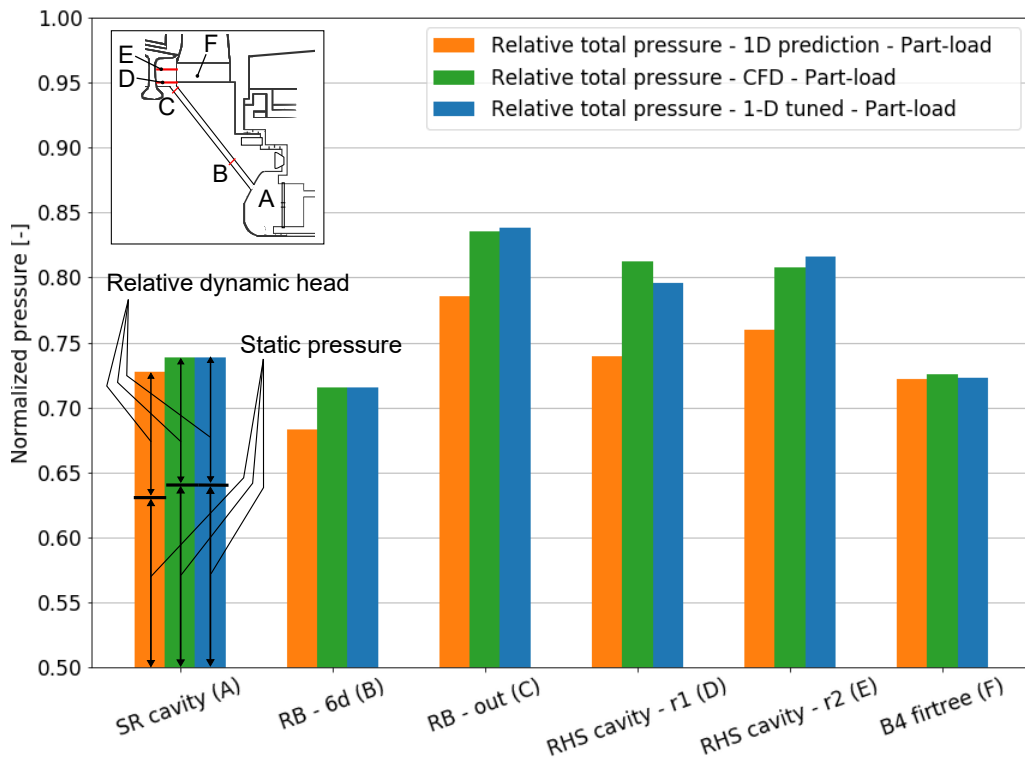


Fig. 4.17: Comparison of total relative and static pressure for the 1-D prediction, CFD analysis and the re-calibrated 1-D flow network at part-load.

The results of the re-calibrated flow network are well aligned with the results from CFD with a relatively small deviation for the nodes at the RHS cavity. This results mainly from the fact that the flow in the cavity is highly 3-D and made complex by the presence of the jet. As done for the base-load case, it was decided not to add additional nodes or elements to model the complex flow field in the cavity and to accept a small discrepancy.

#### 4.3.6 Re-calibration of the 1-D flow network - Temperature

For the temperature distribution, the considerations mentioned above for the base-load case are valid also for part-load. In Fig. 4.18, the distribution of the total relative temperature for the tuned flow network is compared with the prediction and the results from the CFD analysis.

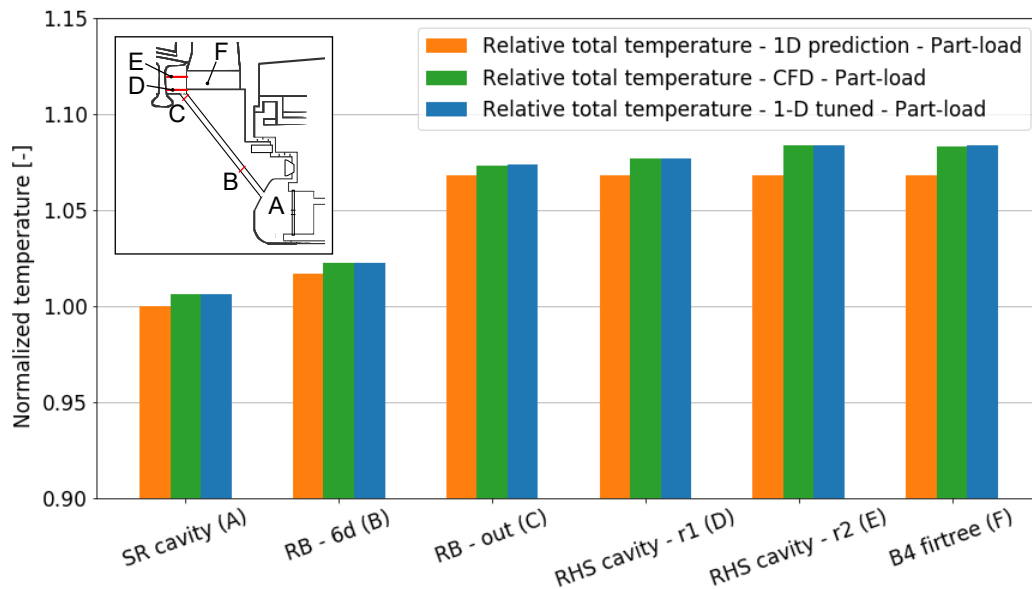


Fig. 4.18: Comparison of total relative temperature for the 1-D prediction, CFD analysis and the re-calibrated 1-D flow network at part-load.

## 5 Conclusion

In this thesis, an investigation for an alternative CA feed system for the last stage blade of a heavy-duty GT has been conducted. In particular, a separately integrated feed system supplied by an external compressor has been studied. In the first part, the requirements and boundary conditions of the feed system have been discussed and analysed. A preliminary performance analysis has shown concrete benefits in terms of GT net power output and GT efficiency provided by the feed system. To design the system, information has been collected from internal studies, literature and interactions with the departments of MI and GTI. As a result, two detailed concepts have been realised. The first concept is characterised by the presence of a cover plate on the rear part of the disk, while the second one is characterised by an additional balcony on the rotor-end disk. In both concepts, the CA flowing to the blades of the last stage of the turbine was provided by RB. Additionally, for both concepts, a solution with PSN as well as without PSN has been considered.

A 1-D flow network has been assembled for all the solutions to evaluate the pressure required by the external compressor. From this analysis, the solution with PSN has been excluded due to the high value of supply pressure required from the external compressor. Although the two concepts have shown a similar pressure distribution, in accordance with the MI and GTI departments, the concept without the cover plate has been judged as the most promising concept. Additionally, the robustness of the concept has been evaluated also at part-load. To improve the reliability of the 1-D flow network, a CFD evaluation of the selected concept at base-load and part-load has been done. The performed CFD analysis has proven that the losses at the inlet of the bore were aligned with the prediction. However, the numerical evaluation has shown that the design of the inlet of the bore must be optimised to minimise the recirculating flow area and thus, to reduce the losses. Furthermore, it has been shown that the losses at the blade's firtree were higher than predicted. To reduce the losses in this area, a bigger area for the firtree channel is necessary.

Ultimately, the 1-D flow network has been re-calibrated using the results provided by the CFD analysis. Hence, the network has become a powerful tool that can be used for further investigations.

As the next step, the feed system needs to be validated in a test rig with real hardware to verify and confirm the results obtained from the numerical investigation. The alternative feed system would bring substantial alterations to the design of the rear part of the turbine disk due to the presence of the bores as well as by the additional balcony. Moreover, a lower CA temperature would modify the mass flow rate required to supply the blades of the last stage. Consequently, further investigations regarding the temperature distribution, the mechanical integrity, the lifetime of the rear part of the turbine disk and the actual CA mass flow rate are necessary to define the feasibility of the concept.

An additional aspect is the selection of the external compressor that must fulfil the requirements of the CA feed system in terms of supplied mass flow and pressure.

In conclusion, this thesis has identified a good starting point, from which more advanced studies can move towards the search for an optimal configuration.

## References

- [1] Ansaldo energia website. <https://www.ansaldoenergia.com/about-us/profile>, accessed 28 February 2022.
- [2] Meherwan P. Boyce. *Gas Turbine Engineering Handbook*. Gulf Professional Publishing, 2002.
- [3] G. Lozza. *Turbine a gas e cicli combinati*. Esculapio edizioni, Italia, 2016.
- [4] G. Dailey. *Design and calculation issues, Aero-Thermal performances of Internal Cooling System in Turbomachinery*. VKI, 2000.
- [5] V. Lanata. *Characterization of Secondary Air System circuits in a Gas Turbine engine*. 2019.
- [6] Carl M. Sangan. *Measurement of ingress through gas turbine rim seals*. University of Bath, 2011.
- [7] R. Jakoby, J. Rinn, C. Appel, and A. Studerus. Turn-down capability of ansaldo energia's gt26. *ASME Turbo Expo 2021: Turbomachinery Technical Conference and Exposition*, 2021.
- [8] K. Döbbling, G. Dousomos, and J. McFeat. Gas turbine and corresponding last rotor disk. <https://patents.justia.com/patent/20180187550>, 7 2016. Patent number 20180187550.
- [9] M. Stämpfli, R. Wifling, and M. Seeman. Locking and fixing device for a heat shield element for a rotor unit of a turbomachine. <https://patents.google.com/patent/US20080181778>, May 5 2010. Patent number US7722319B2.
- [10] Kane D. Virkler, S. Rotor disk assembly for a gas turbine engine. <https://patents.google.com/patent/US10107102B2/en>, 10 2018. Patent number US10107102B2.
- [11] C. Soares. *Gas Turbines (Second Edition)*. Butterworth-Heinemann, Oxford, second edition edition, 2015.
- [12] C. Bricaud. *Charakterisierung der Verluste in Vordralldüsen systemen: Wege zu erhöhter Kühleffektivität in Gasturbinen*. 2014.
- [13] K. J. Kutz and T. M. Speer. Simulation of the secondary air system of aero engines. 1994.
- [14] H. Schlichting and K. Gersten. Grenzschicht-theorie. *Springer-Verlag, Berlin, Germany*, 2004.
- [15] Gan X. Chen, J. X. and J. M. Owen. Heat transfer in an air-cooled rotor-stator system. 1996.

- [16] J. W. Daily and R. E. Nece. Chamber dimension effects on induced flow and frictional resistance of enclosed disks. 1960.
- [17] K. Zhou, S. N. Wood, and J. M. Owen. Computation of ingestion through gas turbine rim seals. 2011.
- [18] A. Prots. *Projektarbeit: Implementation of Piping Elements into a Flow Network Solver for Secondary Air Systems of Gas Turbines*. Faculty of Mechanical Science and Engineering Institute of Power Engineering, Technische Universität Dresden, 2018.
- [19] S. Holzhäuser. *Separately integrated compressor stage for cooling of the posterior turbine blades*. Diploma Thesis No.: D 356/12, Faculty of Mechanical Science and Engineering Institute of Power Engineering, Technische Universität Dresden, 2012.
- [20] B. Sultanian. *Gas Turbines: Internal Flow Systems Modeling*. Cambridge Aerospace Series. Cambridge University Press, 2018.
- [21] Yuxin Liu, Benzhuang Yue, Xiaozhi Kong, Hua Chen, and Huawei Lu. Design and performance analysis of a vane shaped rotating receiver hole in high radius pre-swirl systems for gas turbine cooling. *Aerospace Science and Technology*, 115:106807, 2021.
- [22] S. Holzhäuser, C. Simon-Delgado, and C. Berger. Rotor shaft with cooling bores inlet. <https://patents.justia.com/patent/10113432>, 2 2015. Patent number 10113432.
- [23] C. Bricaud, S. Strueken, and T. Zierer. *Discharge coefficient database*. Ansaldo Energia Internal Document, 2019.
- [24] R. Wächli. *Secondary Air Systems*. KWR lecture series, ABB, 1995.
- [25] Gas turbines - Acceptance tests - ISO 2314:2009(E). Standard, International Organization for Standardization, Geneva, CH, December 2009.
- [26] J. M. Owen and R. H. Rogers. *Flow and Heat Transfer in Rotating-Disc Systems, Volume 1 - Rotor Stator Systems*. ISBN 0863800904, 1989.
- [27] J. M. Owen and R. H. Rogers. *Flow and Heat Transfer in Rotating-Disc Systems, Volume 2 - Rotating Cavities*. ISBN 086380179X, 1995.
- [28] Björn-Christian Will. Theoretical, numerical and experimental investigation of the flow in rotor-stator cavities with application to a centrifugal pump. [https://duepublico2.uni-due.de/receive/duepublico\\_mods\\_00026782](https://duepublico2.uni-due.de/receive/duepublico_mods_00026782), 2011.
- [29] A.A. Lomakin. *Axial Pressure in Centrifugal Pumps, Taking into Account the Influence of the Gap Size in the Packing Rings*. Sovietskoe Kotloturbostroenie, Vol. 12, p. 431-437, 1940.
- [30] A. Egli. The leakage steam through labyrinth glands. 1935.

- [31] I. Idelchik. Handbook of hydraulic resistance, 2nd edition. *Journal of Pressure Vessel Technology-transactions of The Asme - J Pressure vessel technology*, 109, 05 1987.
- [32] C. Bricaud, C. Berger, and S. Rofka. *Six tool documentation*. Ansaldo Energia Internal Document, 2019.
- [33] Y. A. cengel. *Heat and Mass Transfer*. McGraw-Hill Education, 2011.
- [34] N. Shall. Practitioner’s guide: Strengths, weaknesses, opportunities threats (swot). [http://www.methodfinder.net/download\\_all.html](http://www.methodfinder.net/download_all.html), accessed 15 March 2022.
- [35] Centaur software. <https://www.centaursoft.com/why-hybrid-grids>, accessed 29 January 2022.
- [36] Fluent user’s guide. [https://www.afs.enea.it/project/neptunius/docs/fluent/html/ug/main\\_pre.htm](https://www.afs.enea.it/project/neptunius/docs/fluent/html/ug/main_pre.htm), accessed 29 January 2022.
- [37] Fluent theory guide. [https://www.afs.enea.it/project/neptunius/docs/fluent/html/th/main\\_pre.htm](https://www.afs.enea.it/project/neptunius/docs/fluent/html/th/main_pre.htm), accessed 16 February 2022.

## A Appendix

### A.1 Core swirl estimation in the stator-rotor cavity

The flow field inside a SR cavity is highly complex and 3-D. A CFD analysis is a valid analytical method to predict such a flow field with precision. However, a 1-D flow modeling methodology can be employed in order to get a fast prediction of the flow quantities and to give a first guess for the preliminary considerations.

Therefore, a 1-D estimation of the flow field inside a SR cavity is presented.

The cavity is modelled by a simplified cylindrical control volume. For simplicity, a constant axial  $l$  gap is assumed.

In Fig. A.1, the control volume is shown.

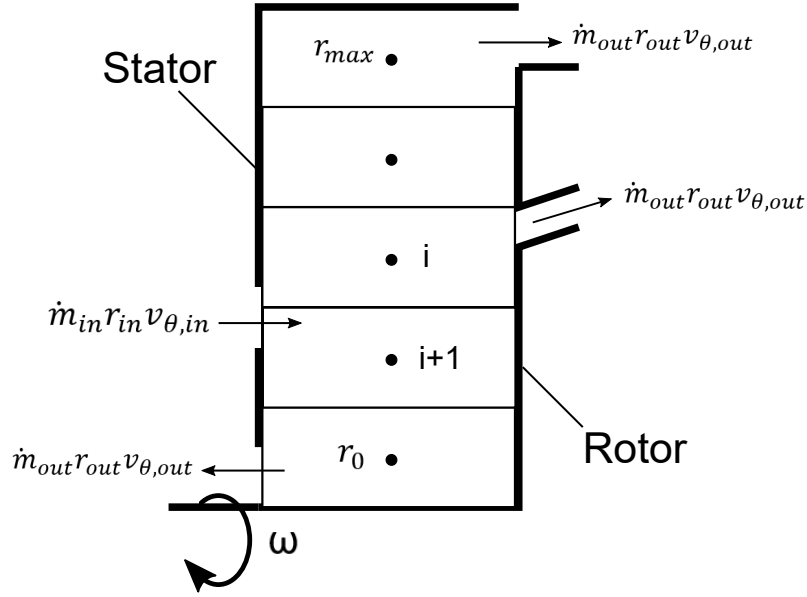


Fig. A.1: Sketch of the control volume used for the core swirl estimation.

The principle of conservation of angular momentum leads to the following equation:

$$\sum \dot{m}_{in} r_{in} v_{\theta in} = M_S + M_R + \sum \dot{m}_{out} r_{out} v_{\theta out},$$

where  $\sum \dot{m}_{in} r_{in} v_{\theta in}$  is the sum of the tangential momentum that enters the control volume,  $\sum \dot{m}_{out} r_{out} v_{\theta out}$  is the sum of the tangential momentum that exits the control volume and  $M_S$  and  $M_R$  are respectively the tangential momentum induced by the stator and the rotor.

To capture the radial variation of the flow properties, the stator-rotor cavity is discretised into a number of cells along the radial direction, as shown in Fig. A.1.

The tangential momentum transferred by the stator to the fluid is:

$$M_S = M_{S,rmax} + \sum dM_{S,i},$$

where  $M_{S,rmax}$  is the momentum transferred by the stator to the first cell along the axial direction:

$$M_{S,rmax} = \rho_m ax \frac{v_{\theta,max}^2}{2} \lambda_s r_{max} \pi l,$$

while  $dM_{S,i}$  is the momentum transferred by the stator to the fluid along the radial direction for the  $i$ -th cell:

$$dM_{S,i} = \rho_i \frac{v_{\theta,i}^2}{2} \lambda_s \left( \frac{r_i + r_{i+1}}{2} \right) \pi (r_i^2 - r_{i+1}^2).$$

Similarly, for the rotor the following equation can be assumed:

$$M_R = \sum dM_{R,i} + M_{R,r0},$$

where  $dM_{R,i}$  is the momentum transferred by the rotor to the fluid along the radial direction for the  $i$ -th cell:

$$dM_{R,i} = \rho_i \frac{(v_{\theta,i} - u_i)|v_{\theta,i} - u_i|}{2} \lambda_R \left( \frac{r_i + r_{i+1}}{2} \right) \pi (r_i^2 - r_{i+1}^2),$$

with  $M_{R,r0}$  as the momentum transferred by the rotor to the first cell along the axial direction:

$$M_{R,r0} = \rho_0 \frac{(v_{\theta,0} - u_0)|v_{\theta,0} - u_0|}{2} \lambda_R r_0 \pi l.$$

The density for the  $i$ -th cell is computed by the ideal gas law, which can be written as

$$\rho_i = \frac{p_i}{R T_i},$$

where  $R$  is the gas-specific constant,  $T_i$  is the static temperature and  $p_i$  is the static pressure.

The pressure distribution along the radial direction can be computed as follows:

$$p_i = p_i + dp_i,$$

where the pressure increment along the radial direction is given by the following equation:

$$dp_i = \rho_i v_{\theta_i}^2 \frac{(r_{i+1} - r_i)}{r_i}.$$

The radial distribution of the temperature is computed under the assumption of constant total absolute temperature according to the following equation:

$$T_i = T_t - \frac{v_{\theta_i}^2}{2C_p}.$$

Ultimately, the radial distribution of the tangential velocity is given by

$$v_{\theta_i} = v_{\theta_{i-1}} \left( \frac{r_{i-1}}{r_i} \right)^n,$$

where  $n$  is the exponent, which defines the radial gradient of the tangential velocity.

The set of equations mentioned above can be solved iteratively once a first guess for  $v_{\theta max}$  is chosen and the exponent  $n$  is fixed.

The result is therefore a radial distribution of  $v_{\theta i}$ , which satisfies the tangential momentum balance.

## A.2 Governing equations for a rotating frame of reference

When the governing equations are solved in the rotating frame of reference, additional terms are inserted in the acceleration of the fluid. These additional terms are the Coriolis acceleration and the centripetal acceleration.

Moreover, the momentum equations can be formulated in two different ways:

- using the relative velocities as dependent variables,
- using the absolute velocities as dependent variables.

The first option is known as the Relative Velocity Formulation. This formulation is advantageous when the relative velocities of the flow field are on average smaller than the absolute ones. In this way, the numerical diffusion is reduced and the solution is more accurate.

The conservation of mass and momentum in the Relative Velocity Formulation are respectively:

$$\frac{\partial \rho}{\partial t} + \nabla \cdot \rho \vec{v}_r = 0$$

$$\frac{\partial \rho \vec{v}_r}{\partial t} + \nabla \cdot (\vec{v}_r \vec{v}_r) + \rho(2\vec{\omega} \times \vec{v}_r + \vec{\omega} \times \vec{\omega} \times \vec{r}) = -\nabla p + \nabla \cdot \overline{\overline{\tau}} + \vec{F},$$

where  $\vec{v}_r$  is the relative velocity vector and  $\overline{\overline{\tau}}$  is the viscous stress expressed in terms of relative components.

The momentum equation contains two additional terms:

- $2\vec{\omega} \times \vec{v}_r$  is the Coriolis acceleration,
- $\vec{\omega} \times \vec{\omega} \times \vec{r}$  is the centripetal acceleration.

[37]

## A.3 Realisable $k - \epsilon$ turbulence model

The Realisable  $k - \epsilon$  turbulence model is a 2-equation model widely used for internal and external flow problems. The governing equations are summed up as follows:

$$\frac{D\rho k}{Dt} = \underbrace{\frac{\partial}{\partial x_j} \left[ \left( \mu + \frac{\mu_t}{\sigma_k} \right) \frac{\partial k}{\partial x_j} \right]}_{\text{Diffusion}} + \underbrace{\mu_t S^2}_{\text{Production}} - \underbrace{\rho \epsilon}_{\text{Dissipation}} - \underbrace{Y_M}_{\text{Compressibility effect}} + \underbrace{P_b}_{\text{Buoyancy production}} + \underbrace{S_k}_{\text{Source}}$$

$$\frac{D\rho \epsilon}{Dt} = \underbrace{\frac{\partial}{\partial x_j} \left[ \left( \mu + \frac{\mu_t}{\sigma_\epsilon} \right) \frac{\partial \epsilon}{\partial x_j} \right]}_{\text{Diffusion}} + \underbrace{\rho C_1 S \epsilon}_{\text{Production}} - \underbrace{\rho C_2 \frac{\epsilon^2}{k + \sqrt{\nu \epsilon}}}_{\text{Dissipation}} + \underbrace{C_{1\epsilon} \frac{\epsilon}{k} C_{3\epsilon} P_b}_{\text{Cross-Diffusion}} + \underbrace{S_\epsilon}_{\text{Source}}.$$

These are the transport equations for  $k$  and  $\epsilon$ , where  $D/Dt$  is the material derivative,  $S_k$  and  $S_\epsilon$  are user-defined source terms [37], and

$$S_{ij} = \frac{1}{2} \left( \frac{\partial u_i}{\partial x_j} + \frac{\partial u_j}{\partial x_i} \right)$$

is the module of the mean-rate-of-strain tensor.

The model constants are:

$$C_1 = \max \left[ 0.43, \frac{\eta}{\eta + 5} \right], \quad \eta = S \frac{k}{\epsilon}, \quad C_{1\epsilon} = 1.44, \quad C_2 = 1.9,$$

while  $\sigma_k$  and  $\sigma_\epsilon$  are the Prandtl numbers for  $k$  and  $\epsilon$  respectively.

The turbulent viscosity is computed as

$$\nu_t = C_\mu \frac{k^2}{\epsilon}$$

where:

$$C_\mu = \frac{1}{A_0 + A_s U^* \frac{k}{\epsilon}},$$

$$U^* = \sqrt{S_{ij} S_{ij} + \tilde{\Omega}_{ij} \tilde{\Omega}_{ij}},$$

$$\tilde{\Omega}_{ij} = \Omega_{ij} - 2\epsilon_{ijk} \omega_k,$$

$$\tilde{\Omega}_{ij} = \overline{\Omega_{ij}} - \epsilon_{ijk} \omega_k.$$

$\overline{\Omega_{ij}}$  is the mean rate-of-rotation tensor viewed in a rotating reference frame with the angular velocity  $\omega_k$ . The model constants  $A_0$  and  $A_s$  are given by:

$$A_0 = 4.04, \quad A_s = \sqrt{6} \cos(\phi), \quad \phi = \frac{1}{3} \cos^{-1}(\sqrt{6}W), \quad W = \frac{S_{ij} S_{jk} S_{kj}}{\tilde{S}_{ij}^2}, \quad \tilde{S}_{ij} = \sqrt{S_{ij} S_{ij}}$$

The Realisable  $k - \epsilon$  turbulence model has shown substantial improvements with respect to the classic  $k - \epsilon$  turbulence model in presence of strong streamline curvature, vortices, and rotation. Additionally, the Realisable  $k - \epsilon$  model provides the best performance of all the  $k - \epsilon$  model versions for several validations of separated flows and flows with complex secondary flow features. [37]